



# Acoustic Focusing for Multiparameter Flow Cytometry

ARTICLE COLLECTION

WILEY

**CURRENT  
PROTOCOLS**  
A Wiley Brand

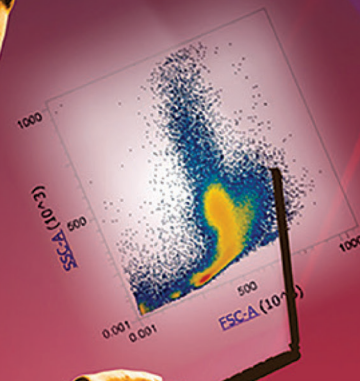
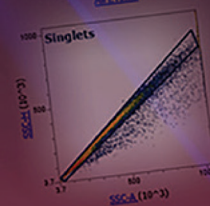
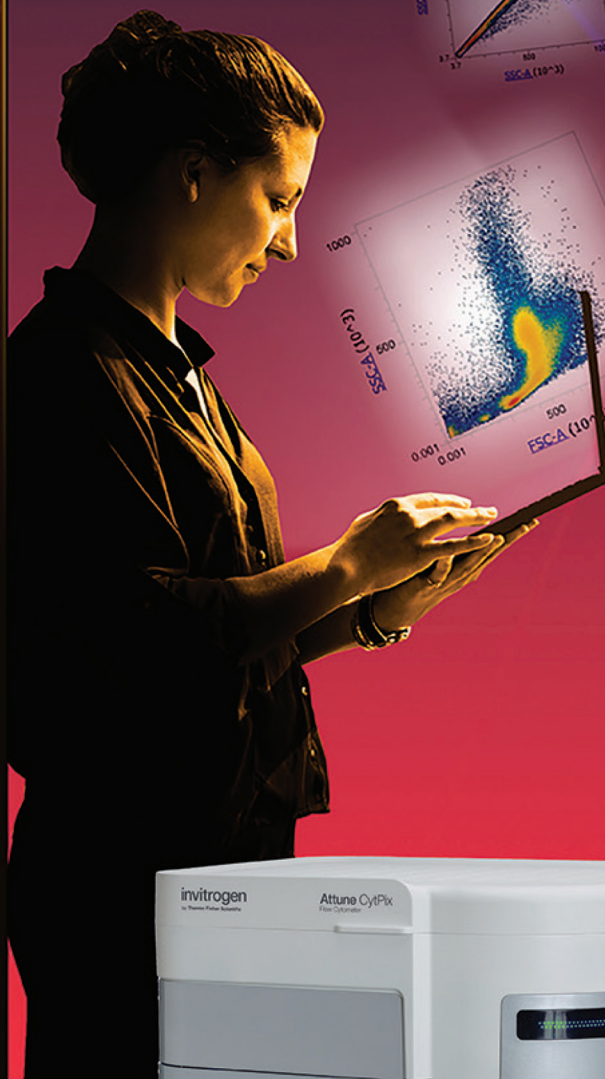
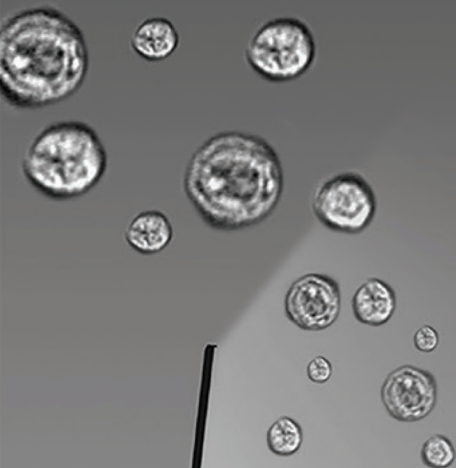
Sponsored by:

**ThermoFisher**  
SCIENTIFIC

The world leader in serving science

invitrogen

Two data sets. One step. Zero doubt.



**Confidently confirm your cell profiles with a new flow cytometer that delivers flow cytometry and imaging data simultaneously.** Now, you can acquire dual data quickly and easily. The new Invitrogen™ Attune™ CytPix™ Flow Cytometer delivers both brightfield images and flow cytometry data sets simultaneously, so you can confirm cellular characteristics and sample quality confidently, without changing your protocols.



Enhance analysis and confidence at [thermofisher.com/cytpix](https://www.thermofisher.com/cytpix)

**ThermoFisher**  
SCIENTIFIC

For Research Use Only. Not for use in diagnostic procedures. © 2021 Thermo Fisher Scientific Inc. All rights reserved. All trademarks are the property of Thermo Fisher Scientific and its subsidiaries unless otherwise specified. COL25211 0621

# Contents

## 4

Introduction

## 5

Fundamentals of Acoustic  
Cytometry

BY MICHAEL D. WARD, AND GREGORY KADUCHAK  
Current Protocols in Cytometry

## 20

Light-Triggered Drug Release from  
Red Blood Cells Suppresses Arthritic  
Inflammation

BY EMILIA M. ZYWOT, NATALIA ORLOVA, SONG DING, RISHI  
R. RAMPERSAD, EMILY M. RABJOHNS, VICTORIA A.  
WICKENHEISSER, QUNZHAO WANG, JOSHUA G. WELFARE,  
LAUREN HAAR, AMANDA M. EUDY, TERESA K. TARRANT,  
AND DAVID S. LAWRENCE

Advanced Therapeutics

## 31

Cell-Based Therapy for Canavan  
Disease Using Human iPSC-Derived  
NPCs and OPCs

BY LIZHAO FENG, JIANFEI CHAO, E TIAN, LI LI, PENG YE,  
MI ZHANG, XIANWEI CHEN, QI CUI, GUIHUA SUN, TAO  
ZHOU, GERARDO FELIX, YUE QIN, WENDONG LI, EDWARD  
DAVID MEZA, JEREMY KLEIN, LUCY GHODA, WEIDONG  
HU, YONGLUN LUO, WEI DANG, DAVID HSU, JOSEPH GOLD,  
STEVEN A. GOLDMAN, REUBEN MATALON, AND YANHONG  
SHI

Advanced Science

## 50

WJMSC-derived small extracellular  
vesicle enhance T cell suppression  
through PD-L1

BY MEIZHANG LI, RUPAL SODER, SUNIL ABHYANKAR,  
HAITHAM ABDELHAKIM, MITCHELLW. BRAUN, CAMILLE  
V. TRINIDAD, HARSH B. PATHAK, ZIYAN PESSETTO,  
CLAYTON DEIGHAN, SIDDHARTHA GANGULY, BUDDHADEB  
DAWN, JOSEPH MCGUIRK, NEIL DUNAVIN, AND ANDREW  
K. GODWIN

Journal of Extracellular Vesicles

Cover Image ©Thermo Fisher Scientific



# Introduction

BY JEREMY PETRAVICZ, PH.D., EDITOR, *CURRENT PROTOCOLS*

The hardware underlying flow cytometers can be broadly divided into two categories: detection and fluidics. Detection encompasses the lasers, filters, and detector modules of the cytometer. The fluidics system includes the sample reservoir, injection stream and flow cell. The precision of identifying and characterizing single cells relies not only on the detection system of the cytometer, but also on the fluidics system. Integral to this is the ability to process the sample into a stream that enables the detection of single cells as they pass the detectors using a process known as hydrodynamic focusing.

In hydrodynamic focusing, the sample or central stream and the sheath fluid run parallel to each other at different rates, with the sheath fluid the slower of the pair. This creates a laminar flow that aligns the cells in the sample stream based on the configuration of the flow cell. There are limits to hydrodynamic focusing: increasing the sample volume input rate leads to corresponding decreases in single cell resolution necessary for applications such as immunophenotyping. To overcome this limitation, flow cytometers can combine hydrodynamic focusing with a process known as acoustic focusing. Acoustic focusing can be thought of as a “pre-alignment” step of the cells in the sample stream prior to being introduced into the sheath fluid. The use of acoustic focusing can enable the user to sort cells at higher rates and with higher precision than hydrodynamic focus alone. However, as discussed in Ward and Kaduchak (2018), there are considerations when deciding if the use of acoustic focusing is appropriate for your sample type. Additionally, acoustic focusing systems can be combined with high-speed brightfield cameras (such as in the Attune CytPix Flow Cytometer system) to obtain images of the cell populations as it is being sorted to examine morphology or the presence of doublet/triplet cells.

This article collection highlights the application of this technology to the development of cell-based therapies, utilizing the strengths of acoustic focusing combined with multiparameter flow cytometry to characterize both cells designed to deliver therapeutics and the impact of cell-based therapies on target cells. Ward and Kaduchak (2018) provides a technical overview of acoustic focusing flow cytometry to familiarize the reader. This overview discusses the strengths and limitations of acoustic focusing, as well as mitigating any potential impacts that it can have on the cells being processed. Next, Zywtot et al (2021) demonstrate how acoustic focusing and imaging flow cytometry can be utilized to analyze the viability and morphology of modified red blood cells (mRBCs) under development as a potential cell-based therapy. The mRBCs were designed to deliver an anti-inflammatory agent in a light dependent manner with higher efficacy than more conventional delivery methods.

The third article is Feng et al (2020) which details the development of an induced pluripotent stem cell (iPSC) based therapy for Canavan disease (CD), a leukodystrophy that leads to loss of myelin and brain degeneration. Acoustic focusing flow cytometry was utilized to obtain candidate cells for generation of human iPSCs from CD patients. These iPSCs were then engineered to carry a functional copy of the ASPA gene which is mutated in CD. Treatment with these engineered cells in a mouse model of CD rescued many of the major pathological features of the disease and increased their survivability. Lastly, Li et al (2020) examined the role of small extracellular vesicles (sEVs) derived from Wharton's Jelly-derived mesenchymal stem cells (WJMSCs) to modulate the immune response to organ transplant. The authors found WJMSCs secrete sEVs enriched in a ligand that modulates T-cell responses. Through acoustic focusing flow cytometry, they were able to characterize the inhibitory action of the ligand on T-cell activation and reduce the pathological response in acute graft versus host disease.

Through the concepts and applications presented in this research article collection we hope to educate scientists on how acoustic focusing and imaging flow cytometry can advance their research and gain deeper insight cell populations. For more information regarding acoustic flow cytometry, we encourage you to visit the **Thermo Fisher Scientific Attune Flow Cytometer** page and explore the possibilities presented there for your research.

## References

- Ward, M. D., & Kaduchak, G. (2018). Fundamentals of Acoustic Cytometry. *Current Protocols in Cytometry*, 84, e36. doi: <https://doi.org/10.1002/cpcy.36>
- Zywtot, E.M., Orlova, N., Ding, S., Rampersad, R.R., Rabjohns, E.M., Wickenheisser, V.A., Wang, Q., Welfare, J.G., Haar, L., Eudy, A.M., Tarrant, T.K. and Lawrence, D.S. (2022), Light-Triggered Drug Release from Red Blood Cells Suppresses Arthritic Inflammation. *Adv. Therap.* 2100159. <https://doi.org/10.1002/adtp.202100159>
- Feng, L., Chao, J., Tian, E., Li, L., Ye, P., Zhang, M., Chen, X., Cui, Q., Sun, G., Zhou, T., Felix, G., Qin, Y., Li, W., Meza, E. D., Klein, J., Ghoda, L., Hu, W., Luo, Y., Dang, W., Hsu, D., Gold, J., Goldman, S. A., Matalon, R., Shi, Y., Cell-Based Therapy for Canavan Disease Using Human iPSC-Derived NPCs and OPCs. *Adv. Sci.* 2020, 7, 2002155.t
- Li, M, Soder, R, Abhyankar, S, et al. WJMSC-derived small extracellular vesicle enhance T cell suppression through PD-L1. *J Extracell Vesicles.* 2021; 10:e12067. <https://doi.org/10.1002/jev2.12067>

# Fundamentals of Acoustic Cytometry

Michael D. Ward<sup>1</sup> and Gregory Kaduchak<sup>1</sup>

<sup>1</sup>ThermoFisher Scientific, Eugene, Oregon

Acoustic cytometry uses radiation pressure forces instead of or in addition to hydrodynamic focusing to position cells or particles in a flowing stream for analysis. Commercial implementations to date combine both hydrodynamic and acoustic focusing together to enable high precision analysis of a broad dynamic range of volumetric sample input rates up to an order of magnitude higher than is practical with hydrodynamic focus alone. This capability allows great flexibility in reducing assay time or modifying or eliminating concentration requirements or concentration steps in sample preparation protocols. It also provides a practical method for processing sub-microliter volumes using sample dilution. In order to take full advantage of this dynamic range, it is necessary to understand the fundamental benefits and limitations of acoustic focusing as applied to flow cytometry. © 2018 by John Wiley & Sons, Inc.

Keywords: acoustic focus • acoustic cytometry • high-speed flow cytometry • hydrodynamic focus • sample preparation

## How to cite this article:

Ward, M. D., & Kaduchak, G. (2018). Fundamentals of Acoustic Cytometry. *Current Protocols in Cytometry*, 84, e36. doi: 10.1002/cpcy.36

## INTRODUCTION

Hydrodynamic focusing uses sheath flow to confine injected sample fluid to a small “sample core” that is typically accelerated to meters-per-second velocity through an optical interrogation region defined by a tightly focused laser beam. The first description of acoustic focusing applied in flow cytometry (Goddard et al. 2006) mimicked this process without requiring sheath flow by exploiting physical differences between cells or particles relative to the background carrier medium to position the particles or cells in a single, focused line along the central axis of a glass capillary. Subsequent commercially available acoustic focusing cytometers have combined hydrodynamic focusing and acoustic focusing together by applying the acoustic focus to a similar ultrasonic capillary device used to inject the sample into a sheath manifold (Acoustic Focusing Overview, 4/12/2017). By focusing cells into a tight line prior to injection in the sheath manifold, precise alignment of cells in interrogating lasers can be maintained at much higher volumetric inputs than possible with hydrodynamic focus alone (Figure 1). These higher input rates enable dilute samples to be processed quickly, without resorting to centrifugation or other concentration steps. Alternately, they allow dilution of concentrated samples or modifying of protocols for lower cell concentrations, without fear of long analysis times.

Acoustic cytometry as referred to herein uses acoustic radiation pressure to align cells in flow for analysis in an interrogation region using optical detectors. It should not be confused with flow cytometry that uses acoustic energy to interrogate cells, (Roos & Apfel, 1988) or that detects acoustic energy from the photoacoustic effect, which is stimulated by light pulses. (Galanzha & Zharov, 2012). Acoustic alignment could however be used together with acoustic interrogation, and detection and photoacoustic analysis has already been combined with acoustic alignment in vivo (Galanzha et.al., 2016).



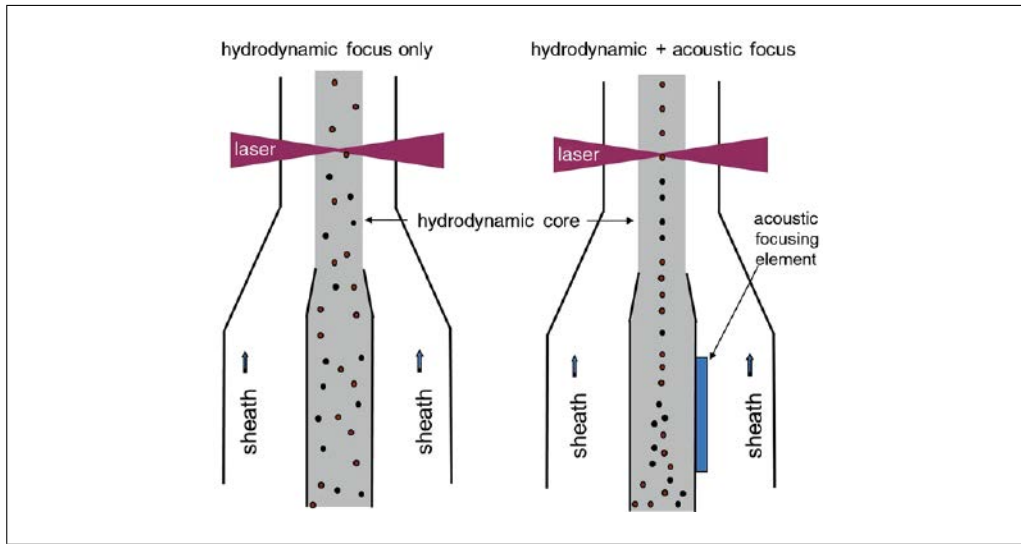


**Figure 1** Comparison of hydrodynamic focus alone (left) versus Acoustic-assisted hydrodynamic focus (right) at a high volumetric sample input rate. Acoustic focusing of particles before sample injection into the sheath manifold allows velocity and illumination precision to be maintained for large sample cores resulting from these rates.

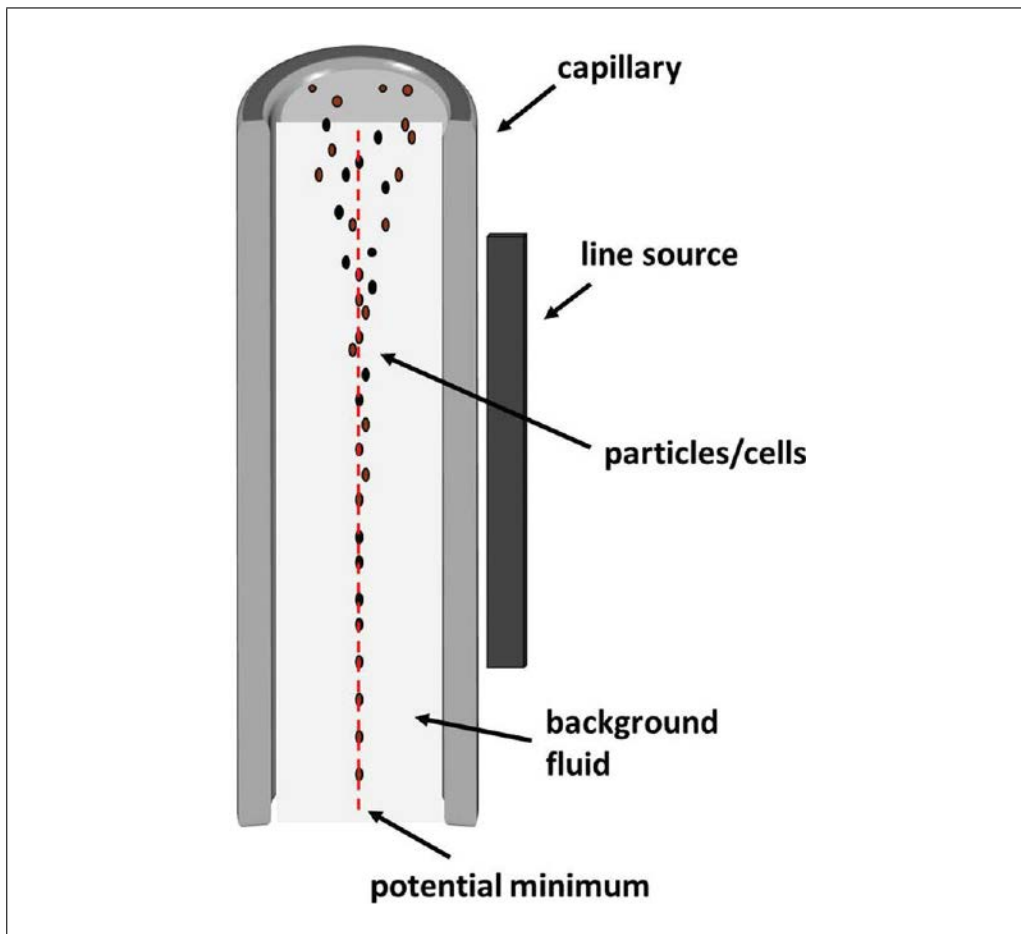


**Figure 2** Schematic of a line-driven capillary depicting tight single line focusing of particles in a flowing liquid using acoustic radiation pressure.

The effect of acoustic radiation pressure on particles in a medium was first described by Kundt and Lehmann (1874) after they witnessed dust particles levitated in organ pipes. This effect has been applied to aqueous solutions for the separation of bioparticles (Coakley, Bardsley, Grundy, Zamani, & Clarke, 1989, 2000; Curtis & Stephans, 1982; Jönsson, Nilsson, Petersson, Allers, & Laurell, 2005; Yasuda, Haupt, & Unemura, 1997). Use of acoustic fields for separation of cells and or positioning cells for analysis continues to be an active area of research today, with wide ranging applications including bulk processing of algae for bio fuels and cells for cell therapy, multiple focused lines of cells for high throughput flow cytometry (Piyasena et al., 2012), and single cell manipulations like cell sorting (Ren et al., 2015). Ren et al. used acoustic traveling waves and a surface acoustic wave device or SAW to sort cells, but the bulk of these studies use resonant square or rectangular cavities to create acoustic standing waves. The acoustic cytometers described here use standing waves generated by a circular focusing device called a line-driven capillary. The line-driven capillary, described by Kaduchak et al. (2008), is an acoustically resonant device that focuses cells or particles into a single line using a capillary driven by a single piezoelectric transducer or line-source (Figure 2). The theory of this device is described by Goddard and Kaduchak (2005).

### THE ACOUSTIC-ASSISTED HYDRODYNAMIC FOCUSING CYTOMETER

Commercial instruments employing these acoustic-focusing devices are more aptly named “acoustic-assisted hydrodynamic focusing cytometers” because they use the line-driven capillary to inject sample into a sheath manifold, in much the same way as a sample injection probe is used in a conventional cytometer (Figure 3).

In contrast, the first acoustic cytometer focused particles without sheath flow (Goddard, Martin, Graves, & Kaduchak, 2006). There are advantages to eliminating sheath, but practical challenges as well. In a sheathless cytometer, the sample is free to contact and contaminate optical flow cell walls. In addition, particle velocity, and therefore dwell time in an interrogating laser, is linearly dependent on volumetric sample input rate. A primary advantage of acoustic focus is that data precision can be maintained over a large dynamic range of volumetric sample input rates. However, in order to take advantage of this range without sheath flow, the electronics and software would need to accommodate

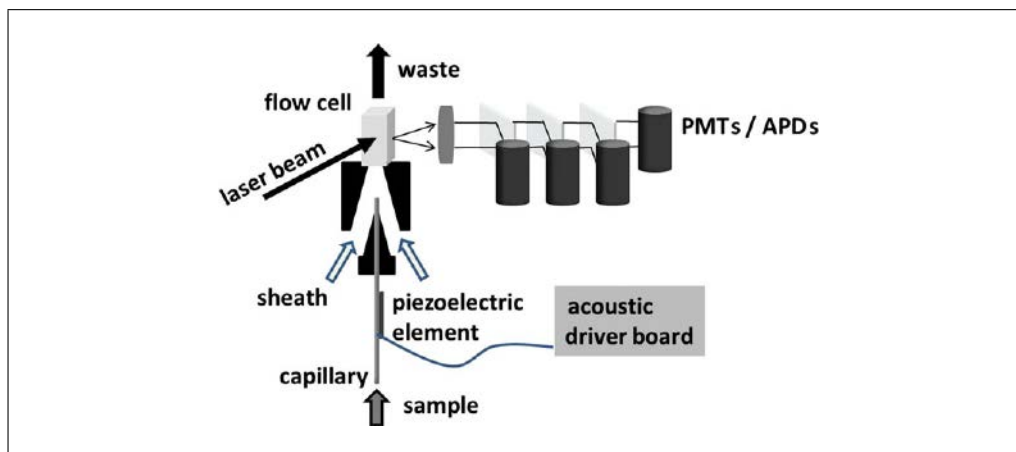


**Figure 3** Generic illustration of an acoustic assisted hydrodynamic focusing analyzer. Sample is forced into the capillary, acoustically focused, injected into a sheath manifold, analyzed, and transferred to waste. As for a conventional flow cytometer, the analysis stage includes a laser beam focused at the position of the particles in the optical cell. The scatter/fluorescent signal is conditioned by appropriate optical filters before optical detection. Driving and control electronics are added to ensure the piezoelectric device is driven at the acoustic resonance frequency of the piezoelectric element/capillary.

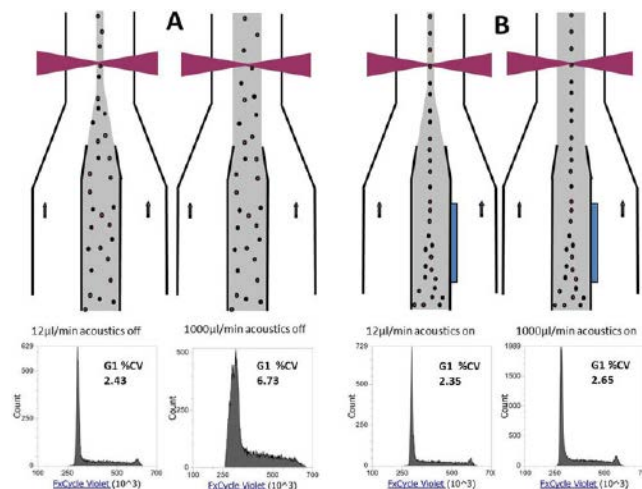


**Figure 4** Schematic drawings of hydrodynamic focus only (**A**) and acoustic assisted hydrodynamic focus at low (left) and high (right) sample input rates. Directly under each schematic is a corresponding cell cycle histogram of FxCycle™ Violet area taken at low (12  $\mu\text{l}/\text{min}$ ) and high (1000  $\mu\text{l}/\text{min}$ ) flow rates.

signals across the same large dynamic range of velocities and laser dwell times. For the instrument used to collect the data presented in Figure 4, the flow rate spans nearly two orders of magnitude (12  $\mu\text{l}/\text{min}$  to 1000  $\mu\text{l}/\text{min}$ ).

Apart from the acoustic capillary and its driving electronics, all the other components in Fig 3 could be used to construct a conventional cytometer. In fact, the instrument can be used as a hydrodynamic focus only instrument by simply turning off the acoustic driver board. This board drives the vibration of the line-driven capillary device using feedback control that ensures that the resonant frequency required for a tight focus is maintained. This frequency varies with the capillary diameter and wall thickness. A 300- $\mu\text{m}$  inner diameter capillary, for example, may have a resonance near 3 MHz, whereas a 600- $\mu\text{m}$  inner diameter capillary resonates at a proportionately lower frequency near 1.5 MHz. The resonance also varies with temperature and fluid properties. The variations for the range of temperatures and samples used in flow cytometry are relatively small, with resonant frequency changes on the order of a few percent, but the feedback control is still essential to ensure optimum performance over this entire range.

During operation of the cytometer, a discreet flow rate between 12 and 1000  $\mu\text{l}/\text{min}$  is chosen and the instrument adjusts its sheath rate such that the ratio of sample to sheath is highest at the lowest rate and lowest at the highest rate. Figure 4 shows schematics for low and high sample input rates with acoustic focusing turned on or off. Cell cycle histograms for actively growing alcohol fixed and FxCycle™ Violet stained Jurkat cells are paired with each schematic. See supplementary material for protocol details. Figure 4A shows the two rates with the acoustic field off (hydrodynamic focus only). The 12  $\mu\text{l}/\text{min}$  rate shows the good precision required for cell cycle analysis, whereas the 1000  $\mu\text{l}/\text{min}$  rate precision is only useful for counting cells. With the acoustic field off, the cells are free to distribute across the large core, and signal precision is degraded by increased variation of cell velocity and illumination intensity of the laser. For this instrument, the precision drop due to illumination position variation is partly mitigated by a flat top laser beam profile, but the G1 cell cycle stage coefficient of variation (CV) is a high 6.73% and the G2 cell cycle peak disappears entirely. With the acoustic field turned on in Figure 4B, velocity and illumination intensity precision are high for both low and high rates. The CV benefit for the acoustic focus vs. no acoustic focus at 12  $\mu\text{l}/\text{min}$  is small at 2.35%



versus 2.43%, respectively, because of the high ratio of sheath to sample at this rate. The precision benefit of acoustic focus tapers off with the decrease in sample core diameter, providing no additional benefit as the core diameter approaches the cell or particle size. In other words, acoustic focus does not push a 10  $\mu\text{m}$  diameter cell any closer to the center of a 10  $\mu\text{m}$  diameter sample core than does hydrodynamic focus.

The high precision demonstrated in Figure 4B at 1000  $\mu\text{l}/\text{min}$  enables running of samples up to 10 times faster than in cytometers without acoustic focus. This does not mean, however, that all samples should be run this fast. Understanding how best to take advantage of this increased throughput can be made easier by answering the following questions: (1) How are different cells or particles focused by the acoustic field? (2) What is the acoustic concentration effect and how does it pertain to sample concentration and injection rates? Once these questions are answered, one can begin to ask about how acoustic cytometry can help answer questions in biology, chemistry, and medicine.

## ACOUSTIC FORCE ON PARTICLES IN A MEDIUM

The answer to the question of how cells or particles are affected by acoustic focus starts with the mechanical properties of both the particles and the medium they are carried in. Equation 1 gives the acoustic force  $U$  exerted on a particle in a carrier medium, Gorkov (1962):

$$U = \frac{4}{3}\pi a^3 \left[ \left( \beta_o \frac{\langle p^2 \rangle}{2} \right) f_1 - \frac{3}{2} \left( \frac{\rho_o \langle v^2 \rangle}{2} \right) f_2 \right]$$

Equation 1

Here,  $a$  is the particle radius,  $\beta_o$  is the compressibility of the surrounding fluid, and  $\rho_o$  is the density of the surrounding fluid. The pressure and velocity of the acoustic field in the absence of the particle are described by  $p$  and  $v$ , respectively, and the brackets correspond to a time-averaged quantity. The terms  $f_1$  and  $f_2$  are the contrast terms that determine how the mechanical properties (compressibility and density, respectively) of the particle differ from the background medium. They are given by the following Equations 2a and 2b:

$$f_1 = 1 - \frac{\beta_p}{\beta_o}$$

Equation 2a

$$f_2 = \frac{2(\rho_p - \rho_o)}{(2\rho_p + \rho_o)}$$

Equation 2b

The subscript  $p$  corresponds to intrinsic properties of the particle. The force  $F$  acting on a particle is related to the gradient of the force potential  $U$  by Equation 3:

$$F = -\nabla U$$

Equation 3

Particles will be localized at positions where the potential  $U$  displays a minimum (stable equilibrium). The acoustic contrast of a particle (or medium) is determined by the density and compressibility differences between it and the background medium as defined by terms  $f_1$  and  $f_2$  in Equations 2a and 2b. The relative magnitudes and signs of  $f_1$  and

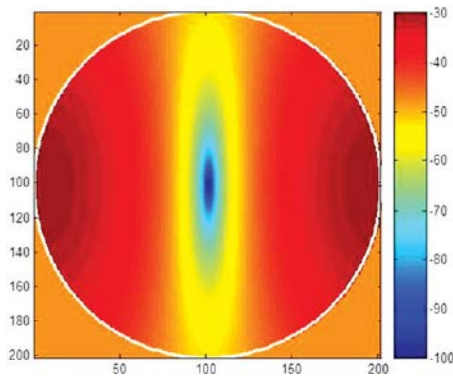


**Figure 5** Calculated acoustic force potential in the cross-section of an acoustically driven capillary. Particles with positive acoustic contrast are focused toward the force potential trap in the center of the cross-section. Note that the acoustic field is asymmetric, with stronger gradients along the axis of the piezo driver. This asymmetry can improve precision of analysis of non-spherical cells by helping to orient them in interrogating lasers.

$f_2$  determine the behavior of the radiation force potential  $U$  and thus determine the magnitude and direction of the acoustic radiation pressure force. As an example, if a particle and the background medium share the same density value ( $\rho_p = \rho_0$ ), then  $f_2$  is zero and the acoustic contrast is due only to compressibility differences in  $f_1$ . If both  $f_1$  and  $f_2$  are zero, then there is no acoustic contrast. Figure 5 displays the force potential  $U$  for an erythrocyte within the cross section of an acoustically driven capillary containing phosphate buffered saline. Particles traveling through the capillary experience a time averaged force that transports them into the deep potential well centered along the axis of the capillary.

It should be noted that nearly all particles and cells of interest have acoustic contrast values in water or aqueous buffers, which force them to migrate to the central axis of the capillary (as shown in Figure 5). These particles have positive acoustic contrast in these fluids. There are a few materials such as fat particles and gas bubbles that have negative acoustic contrast which forces their migration toward the wall of the capillary in the acoustic field.

### Effects on Cell Health and Viability

Detrimental acoustic effects on cells are invariably at the top of the list of concerns for many cell biologists when introduced to the topic of acoustic focusing. This is because ultrasonic energy is routinely used for lysis of cells as hardy as bacterial spores. Like most acoustic resonators designed for cell manipulation (Wiklund, 2012), line driven acoustic capillaries used for cytometry are different from devices designed to lyse cells in fundamentally important ways. First, acoustic lysis is typically done using sub-megahertz frequencies that can create cavitation, a phenomenon in which tiny gas bubbles form and collapse with tremendous local shear and heating. The acoustic focusing capillaries used here operate at a frequency well above 1 MHz without cavitation. Second, acoustic lysis is performed at very high energy levels where acoustic streaming and rapid fluid heating are common. Acoustic cytometry is performed with relatively low energy levels of tens of milliwatts maximum electrical input power at the high sample flow rate of a milliliter per minute. At lower flow rates, this power is progressively scaled down. The acoustic energy dissipated in the fluid is also significantly less than the electrical input energy. The design of the acoustically driven capillary spreads this energy over the entire length of the capillary and there is very little sample heating. Goddard, Sanders, Martin, Kaduchak, and Graves (2007) showed that the viability of Chinese hamster ovary (CHO) cells was

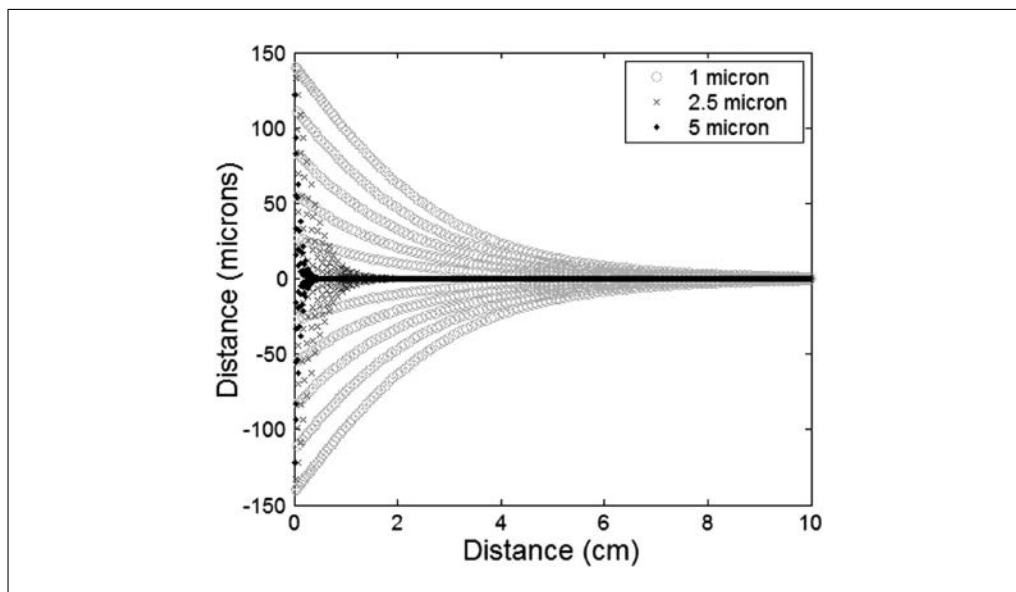


**Figure 6** Calculated trajectories of different diameter microspheres as they travel along the axis of the acoustic focusing capillary. The vertical axis is the particle position relative to the capillary axis. The horizontal axis is the particle position along the length of the capillary. Sample flows from left to right at a rate of 1000  $\mu\text{l}/\text{min}$ .

not significantly affected by the acoustic field created by a large acoustically driven capillary even in the sub-megahertz region. The higher, gentler megahertz frequencies now utilized in commercial cytometers are routinely used in safe medical imaging of patients and are thought to be gentle enough for cell separations where cell health or recovery are critical, such as cell therapy (FloDesign Sonics) or circulating tumor cell separation. (Li et al., 2015). Pre-focusing in the injector with acoustics also serves to reduce the acceleration of cells required in the subsequent hydrodynamic focus where cells can undergo significant shear forces.

### Particle or Cell Size

While many cells and microbes have similar acoustic contrast, the acoustic force on different sized particles varies widely. As can be seen from Equation 1, the acoustic force is proportional to the third power of the particles' radius. The force resisting movement of the particle is the Stokes drag force  $F_d$ , which can be approximated by the following Equation 4 for a hard sphere with particle Reynolds numbers  $<0.1$ :

$$F_d = 6\pi r_p \eta u_r$$

**Equation 4**

Here  $r_p$  is the cell or particle radius,  $\eta$  is the medium viscosity, and  $u_r$  is the acoustically induced velocity in the radial direction.  $F_d$  is linearly proportional to radius, so the net result is that overall force is proportional to the particles' radius squared with small particles moving more slowly than large particles of similar acoustic contrast. Figure 6 shows the predicted trajectories of various sizes of polystyrene beads in a sample flowing in the axial direction in the acoustic capillary. As can be seen from this figure, it takes longer for the smaller particles to reach the capillary axis. This in turn dictates that volumetric sample throughput should be reduced when processing smaller particles such as bacteria. If the residence time within the capillary of particles or cells of a given size is not long enough, the variation in position of the particles/cells about the central capillary axis will be greater and the coefficient of variation (CV) of the optical measurement will

suffer at the higher sample input rates. Acoustics may contribute to focus and may also align asymmetric cells but smaller particles should generally be analyzed at conventional sample input rates, so that the additional hydrodynamic focusing can help ensure higher precision.

If the particle is so small that the acoustic force is weaker than Brownian motion, the acoustic field will not have a focusing effect, such that positioning precision will depend solely on the hydrodynamic focus. This size cutoff is a function of acoustic contrast factors, acoustic power, and frequency and is beyond the scope of this unit, but in general, nano particles, like exosomes and viruses, should be analyzed with low sample input rates/high sheath to sample ratios, as in any flow cytometer.

### THE ACOUSTIC CONCENTRATION EFFECT

The focusing of all cells in the capillary volume to a line in the center of the capillary creates a local effective cell concentration that can be many times higher than the initial starting concentration. This enables much faster analysis of dilute samples, but it necessitates the addition of sheath fluid at higher cell concentrations in order to maintain single particle analysis. Figure 7 illustrates the acoustic concentration effect in the absence of sheath. Whole blood diluted to about  $2 \times 10^7$  (Figure 7A and B) and  $2 \times 10^6$  red blood cells per ml (Figure 7C) was imaged in a quartz flow cell after pumping through a capillary with the acoustic field turned off (7A) and on (7.B and C). When the acoustic field is on, all of the positive acoustic contrast particles in the capillary are forced to the center before being pumped into the flow cell. This effect in relatively concentrated samples results in a rope-like sheet of particles that can be many particles in width like that seen in Figure 7B.

In the instrument, this rope is injected into a sheath manifold where sheath fluid speeds up and separates the cells, creating single particle spacing dependent on the sample to sheath ratio. A 1:10 sample to sheath ratio for example, would create spacing similar to that seen in the 10-fold dilution of sheathless sample in Figure 7.C. Rope-like conditions similar to Figure 7B can be created in the laser interrogation zone of the instrument itself by diluting less and running at high sample input rates. For a 10-fold dilution of blood

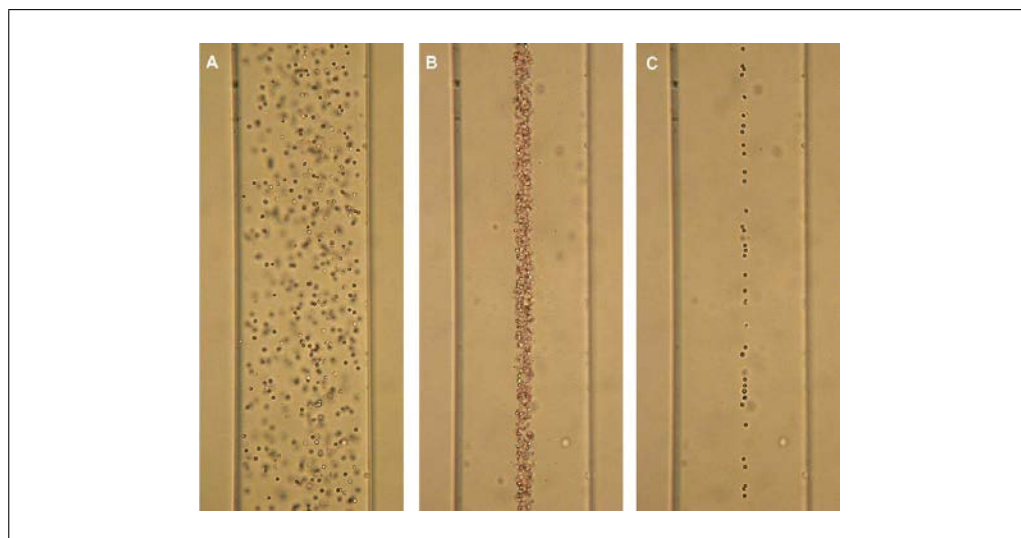


**Figure 7** Micrographs of dilute acoustically focused whole blood pumped into in a square quartz flow cell without sheath. (A, B)  $2 \times 10^7$  RBCs per ml (C)  $2 \times 10^6$  RBCs per ml. In the instrument, where sheath flow accelerates the sample and separates the cells, a 100 fold and a 10 fold higher concentration respectively run at  $1000 \mu\text{l}/\text{min}$  would be needed to produce similar concentrations to B and C in the laser interrogation zone.



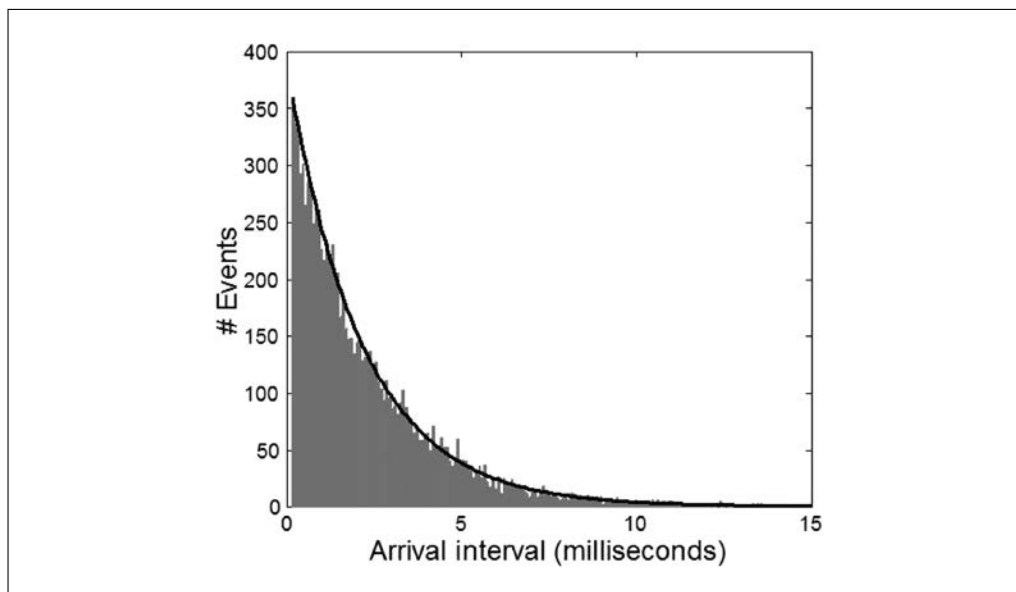


**Figure 8** Plot of number of events versus arrival interval at the interrogation laser for acoustically focused microspheres in flow at 1 ml/min without sheath flow. The black line is an exponential distribution. The experimental data (gray bars) closely matches this prediction.

containing  $5 \times 10^9$  RBCs per ml and injected at 1000  $\mu\text{l}/\text{min}$ , approximately 8 million RBCs per second pass through the instrument. For a core velocity of 8 meters/second, this averages about 10 cells per 10 micron length of sample core. With several cells in the laser focus at all times, scatter is completely useless, but fluorescence data can still be collected from white blood cells. This sounds attractive from a throughput standpoint, because white blood cell coincidence under these conditions is still relatively rare for whole blood, but the quality of fluorescence data is degraded. Higher concentration of unbound fluorophore, combined with non-specific staining, reduces sensitivity such that this technique can typically only be used for high density antigens with bright labels. An additional effect is the absorbance of violet laser light by hemoglobin, which further diminishes signals for violet excitable probes.

### **Volumetric Throughput, Poisson Rate and Coincidence**

Although acoustic cytometers can process sample volumes an order of magnitude faster than conventional cytometers, this does not mean that all samples should be processed this fast. This is often desirable for more dilute samples, but at higher concentrations, all cytometers, including acoustic ones with or without sheath, are limited by coincident events as governed by Poisson statistics. Figure 8 shows that the inter-arrival times of particles that have been acoustically focused follow an exponential distribution, which is in agreement with a Poisson process.

Poisson statistics predict the likelihood of one cell, no cells, or more than one cell being present in an event window. As sample throughput increases with higher sample concentration, the probability of a cell being present in an interrogating laser beam in any given window of time increases, but the probability of more than one cell being present in the laser also increases (a coincident event).

Coincidence in an event window should generally be kept low by using mean rates of less than one event per ten event windows for most assays (van den Engh, 2000). This condition theoretically corresponds to a 10% coincidence rate. While speed of electronics can also limit event rates, most modern cytometers are capable of electronic event rates

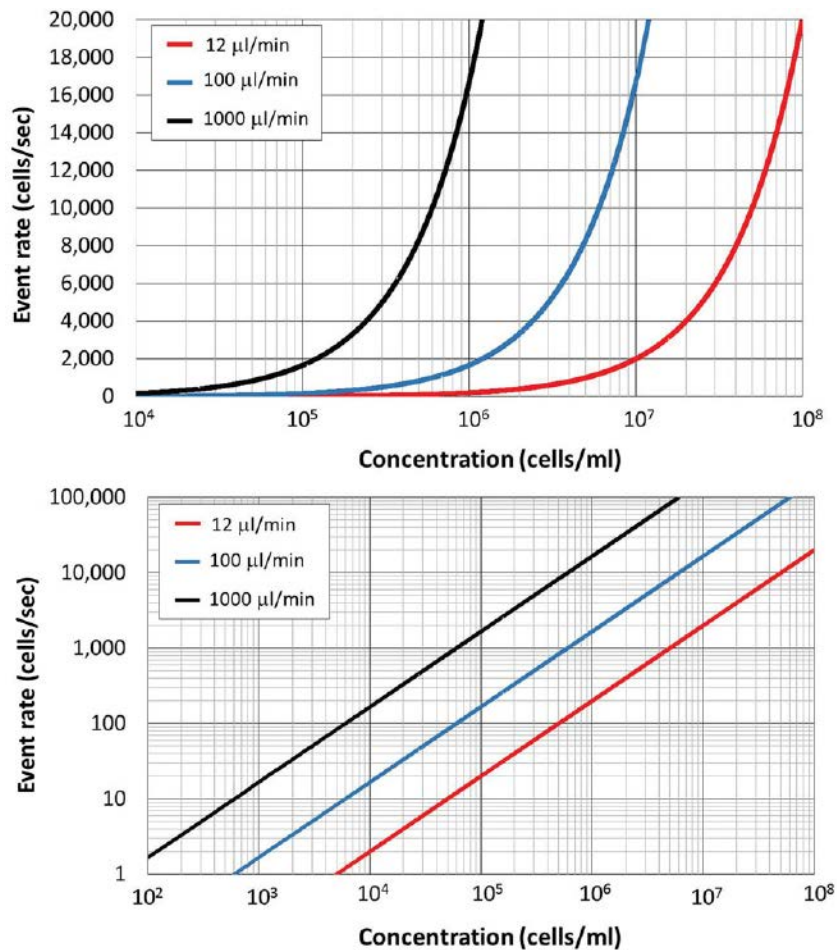


**Figure 9** Linear versus log (top) and log versus log (bottom) plots for cell event rate versus initial sample concentration for sample input rates of 12, 100, and 1000  $\mu\text{l}/\text{min}$ . Event rates are theoretical and exclude the impact of coincidence. Linear plotting of event rate emphasizes the low event rates obtained with cell concentrations below one million per milliliter at conventional rates. Log plotting of event rate shows both the need for high throughput rates at the lowest cell concentrations and the danger of exceeding maximum instrument event rates at high cell concentrations.

that significantly exceed their 10% Poisson rate, which is governed by the magnitude and variation of cell velocity.

Large variation in cell velocity for large sample cores limits sample core size and consequently volumetric throughput in a conventional cytometer. The size of an event window dictates the Poisson rate, and in a cytometer with spatially separated lasers, the event window must typically be extended to account for different laser to laser arrival times for particles or cells having different velocities. In a large core without acoustic focus, the large spread in transit times requires larger event windows which decrease the Poisson rate.

If lower coincidence is desired or higher coincidence is acceptable, sample concentration and or volumetric sample rate should be adjusted accordingly with a corresponding decrease or increase in particle throughput. Figure 9 shows linear (top) and log (bottom) plots of theoretical event rates that exclude the impact of coincidence. Event rates are in cells per second as a function of the log of sample concentration for three different volumetric flow rates: 12, 100, and 1000  $\mu\text{l}/\text{min}$ . The first two rates cover a similar

dynamic range to most conventional cytometers and the third is the highest rate on the acoustic cytometer. Many flow cytometry protocols are written for cell concentrations in the millions per milliliter range. The plots show that this is no accident, since this is where the event rate for the first two traditional sample input rates reaches the hundreds and low thousands per second, where analysis time can be kept reasonable while maintaining lower coincidence.

The linear versus log plot emphasizes that much below one million cells per milliliter, conventional sample rates can mean long analysis times. At 100,000 cells per milliliter a 100  $\mu\text{l}/\text{min}$  input rate delivers just 167 cells per second and the 12  $\mu\text{l}/\text{min}$  rate delivers only 20 per second. The log versus log plot gives a quick look at extremely low concentrations, where event rates dip below 1 cell per second at concentrations less than 600 and 5000 cells per milliliter for these flow rates respectively. At the high concentration extremes, the log versus log plot readily shows that the high acoustic assisted sample input rate of 1000  $\mu\text{l}/\text{min}$  can easily deliver cells fast enough to exceed instrument Poisson rates above concentrations of one million cells per ml. This rate of 35,000 events/sec for the instrument used here, is reached for a concentration of just over two million cells per milliliter. It follows then, that for many conventional cytometry protocol concentrations, a lower sample rate should be used or the sample should be diluted.

### **A DIFFERENT PARADIGM FOR SAMPLE DILUTION**

With acoustic focus, the additional order of magnitude for the sample throughput rate that is possible, allows cytometrists to think outside the box of conventional sample protocol concentrations. Sample dilution is often kept to a minimum in cytometry protocols because of fear of long analysis times, but dilution need not be feared with the higher volumetric throughput. The high dynamic range of the acoustic assisted cytometer offers great flexibility in reducing assay time, reducing assay concentration requirements or eliminating concentration steps. Dilute samples can be run quickly and samples that are diluted during sample preparation protocols may sometimes be run without an otherwise needed final centrifugation step.

Protocols may also be altered if there is a benefit to lower concentration such as reduced cell sticking. Some sample preparation protocols, like magnetic bead separations for example, can have higher purity and/or recovery when the final separation step in the magnetic field is performed with greater dilution. Higher dilutions are often not used however, as losses in any additional required concentration step offset these benefits.

A less obvious benefit of dilution is that it allows a greater percentage of cells to be analyzed without fear of sucking up an entire sample and introducing air into the system. Assuming an instrument dead volume and a residual volume that is typically left in a tube after processing, the percentage of cells left behind is linearly related to the dilution factor. If for example 50  $\mu\text{l}$  of a concentrated 100- $\mu\text{l}$  sample are left after analysis, this translates to 50% unanalyzed cells. If the same sample is diluted 10-fold before analysis, only 5% of the cells will remain in the same 50  $\mu\text{l}$  residual volume.

#### ***Small initial sample size***

High volumetric sample throughput combined with high dilution factors make it practical to use very small initial sample sizes without fear of losing significant cells to instrument dead volume or residual volume. Even fractions of very small samples can often be used for experimental set-up or alternate sample treatments.

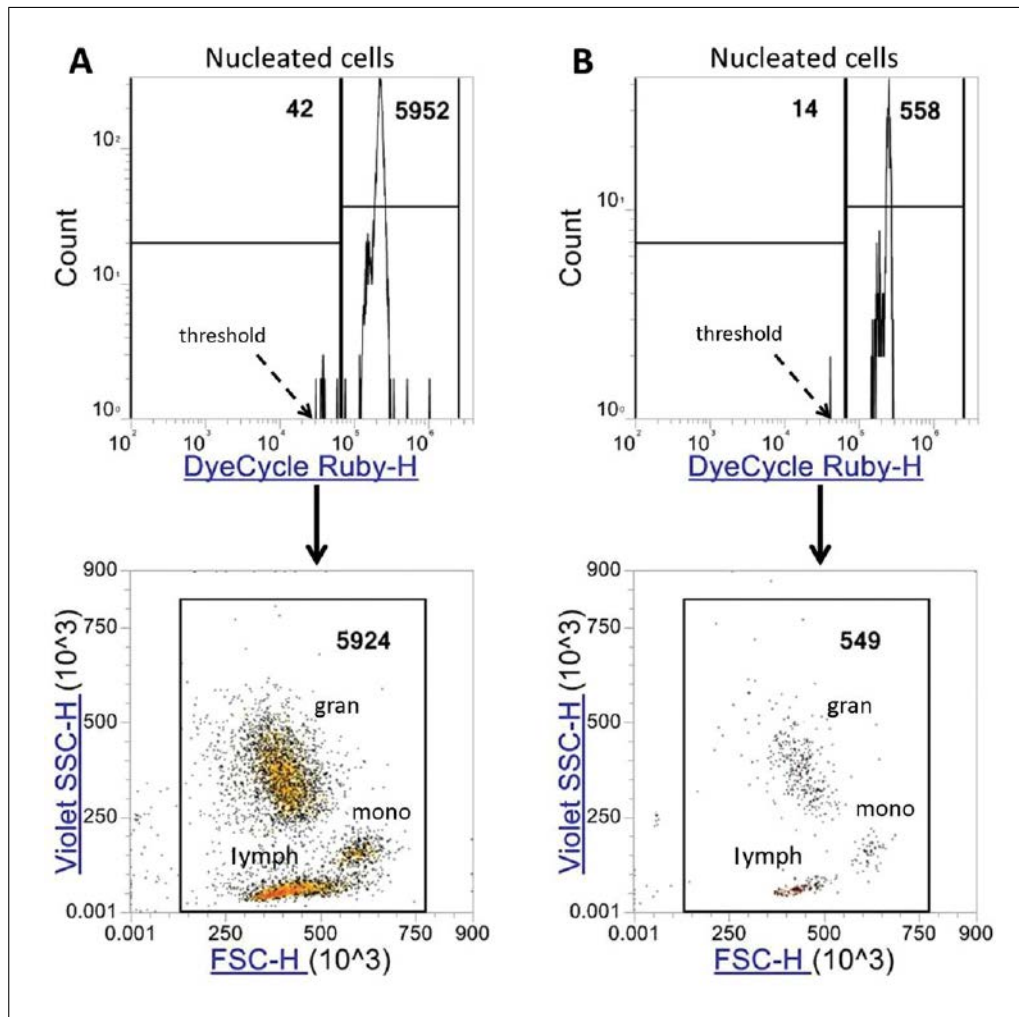


**Figure 10** Analysis of nucleated cells from 940 nl (A) and 94 nl (B) of whole blood with 850-fold and 8500-fold dilution, respectively. Nucleated cells are plotted on a log log histogram of DyeCycle™Ruby fluorescence showing the threshold level used for collection and a linear 405 nm violet SSC-H versus FSC-H differential scatter plot showing white blood cell populations Granulocytes (Gran), Monocytes (Mono), and Lymphocytes (Lymph).

For precious samples where analyzing every cell is important, combining a “no lyse, no wash” protocol with high dilution prevents cell loss from centrifugation or lysis reagents and decreases cells lost in residual volume. For Figure 10A a 1  $\mu$ l sample of whole blood was diluted into 850  $\mu$ l of DyeCycle™Ruby nucleic acid staining buffer and 800  $\mu$ l, of this dilution was run at 1000  $\mu$ l/min with an analysis time of about 46 sec. For Figure 10B, the 1  $\mu$ l sample is diluted as for A and 85  $\mu$ l of this dilution was diluted another 10-fold and run as in A. Nucleated cell events are captured by thresholding on DyeCycle Ruby high events.

For each sample, 800  $\mu$ l of an 850  $\mu$ l sample or 94% of the sample is analyzed, equating to 940 nl (A) and 94 nl (B) of the original whole blood sample. Each sample is plotted with a log log histogram of DyeCycle Ruby fluorescence and a corresponding differential white blood cell scatter plot using 405 nm violet SSC-H versus FSC-H (488 nm blue). For full protocol and instrument setup, see supplementary material. Note that for whole unlysed blood on this instrument, the position of granulocytes in FSC is shifted significantly to the left relative to ammonium chloride lysed blood. Red blood cell lysis protocols can change white blood cell morphology, particularly for granulocytes. The differences in FSC seen from morphology changes are dependent on interrogating light parameters



including wavelength, scatter collection angles and laser focus and alignment. (Petritz et al., 2017).

For “no-lyse, no-wash” protocols and for any protocol in which a wash step may be removed, it is important to understand how assay background can either be increased by the large sample cores generated at high volumetric input rates or reduced by dilution of the free fluorophore in a sample.

### ***Background reduction from dilution***

One concern that arises when proposing elimination or significant reduction of sheath ratios is that the benefit of squeezing the sample core to a very small size, such that very little free fluorophore is excited by the laser, is lost. If the sample core is large, the laser will excite free fluorophores throughout the beam focus, resulting in higher background for unwashed samples. This effect is mitigated somewhat by the tight Gaussian focus of the laser beam and by spatial filtration in the collection optics, but for a given concentration of unbound fluorophore, fluorescence background is higher than for a tightly hydrodynamically focused core. With dilution, however, the concentration of free label is reduced by the dilution factor, reducing the fluorescence background. Dilution, like washing by centrifugation, will disturb the binding equilibrium, but for higher affinity labels, dissociation will be insignificant if it is performed within a reasonable time before analysis. For many antibodies with useful affinity, dissociation half-lives are on the order of hours or days. If dissociation for lower affinity ligands is of concern, rapid dilution followed by analysis with a high volumetric sample rate can be used as a quicker alternative to centrifugation for background reduction.

As a frame of reference for background reduction, a single round of centrifugation, depending on operator and dilution prior to and after centrifugation, is typically comparable to about a 300-fold dilution. For a properly titrated immunophenotyping experiment with high affinity antibodies, non-specific binding contributes more to background than does unbound fluorophore at this dilution, and continued dilution beyond 500 to 800-fold may not significantly reduce background levels.

Note that for lower affinity reagents like nucleic acid stains, dilution can disturb equilibrium in a short period of time and that for some high precision assays like cell cycle analysis, the dilution buffer should contain equilibrium concentrations of these low affinity stains. This can increase background in large cores, even for dyes considered “non-fluorescent” until bound, depending on the dye concentration and the ratio of fluorescence enhancement upon binding.

## **SUMMARY AND OUTLOOK**

Use of acoustic fields for separation and positioning of cells and particles has been an active and growing area of research for nearly four decades. Diverse uses of these fields in flow cytometry have been suggested, including pre-analysis sample preparation, acoustic cell sorting, multi-stream analysis and sheathless triggered stopped or even reverse flow analysis. Commercial implementations to date have focused on combining sheath and acoustic focusing to create instruments capable of high precision analysis over a high dynamic range of volumetric sample inputs from 12  $\mu\text{l}/\text{min}$  to 1000  $\mu\text{l}/\text{min}$ .

This expansion of dynamic range enables up to an order of magnitude faster analysis times versus conventional hydrodynamic focusing alone, particularly for dilute samples, and provides greater flexibility in sample preparation protocols. Protocols can be modified to run lower concentrations of cells, eliminate extra concentration steps or dilute to extend the number of experiments possible or increase the percentage of cells analyzed in very small volumes. Flexibility for sample dilution ratios is particularly useful for optimization

of no lyse no wash assays where red blood cell lysis and centrifugation are avoided to minimize potential sample preparation artifacts.

Increasing availability of more and more parameters in flow cytometry has spurred discovery of new cell types, more correlation of phenotyping with live cell function and increasing scrutiny of smaller and smaller phenotypic and functional cell subpopulations. The concern that sample preparation causes loss or alteration of specific fragile cells has grown in the face of this research, making protocols that can minimize impact on live cells and their response to environment and stimuli highly desirable.

Understanding the fundamental advantages and limitations of acoustic focusing as applied to flow cytometry can enable users to better leverage the technology, not only to increase throughput and save time but also to modify and improve sample preparation and minimize its effects on cell biology.

### Acknowledgements

The authors thank Marc DeJohn of Biomeme Inc. and the late Carl Stewart and Patrick Turner for their significant contributions to the implementation of acoustic focusing in flow cytometry. We also thank Jolene Bradford of Thermo Fisher Scientific for valuable support and advice.

### Conflicts of Interest

The authors are employees of Thermo Fisher Scientific, which is in the business of selling flow cytometers and flow cytometry reagents.

### Literature Cited

- Acoustic Focusing Overview, 4/12/(2017). Retrieved from <https://www.thermofisher.com/us/en/home/life-science/cell-analysis/flow-cytometry/flow-cytometers/acoustic-focusing-technology-overview.html>. Accessed November 28, 2017.
- Coakley, W. T., Bardsley, D. W., Grundy, M. A., Zamani, F., & Clarke, D. J. (1989). Cell manipulation in ultrasonic standing wave fields. *Journal of Chemical Technology and Biotechnology*, 44, 43–62. doi: 10.1002/jctb.280440106.
- Coakley, W. T., Hawkes, J. J., Sobanski, M. A., Cousins, C. M., & Spengler, J. (2000). Analytical scale ultrasonic standing wave manipulation of cells and microparticles. *Ultrasonics*, 38, 638–641. doi: 10.1016/S0041-624X(99)00151-1.
- Curtis, H. W., & Stephans, E. J. (1982). Ultrasonic continuous flow plasmapheresis separator. *IBM Technical Disclosure Bulletin*, 25(1).
- Galanzha, E. I., & Zharov, V. P. (2012). Photoacoustic flow cytometry. *Methods (San Diego, Calif.)*, 57(3), 280–296. doi: 10.1016/j.jymeth.2012.06.009.
- Galanzha, E. I., Viegas, M. G., Malinsky, T. I., Melerzanov, A. V., Juratli, M. A., Sarimol-laoglu, M., ... Zharov, V. P. (2016). In vivo acoustic and photoacoustic focusing of circulating cells. *Scientific Reports*, 6, 21531. doi: 10.1038/srep21531.
- Goddard, G., & Kaduchak, G. (2005). Ultrasonic particle concentration in a line-driven cylindrical tube. *Journal of the Acoustical Society of America*, 117, 3440–3447. doi: 10.1121/1.1904405.
- Goddard, G., Martin, J. C., Graves, S. W., & Kaduchak, G. (2006). Ultrasonic particle concentration for sheathless focusing of particles for analysis in a flow cytometer. *Cytometry*, 69, 66–74. doi: 10.1002/cyto.a.20205.
- Goddard, G. R., Sanders, C. K., Martin, J. C., Kaduchak, G., & Graves, S. W. (2007). Analytical performance of an ultrasonic particle focusing flow cytometer. *Analytical Chemistry*, 79, 8740–8746. doi: 10.1021/ac071402t.
- Gorkov, L. P. (1962). Forces acting on a small particle in an acoustic field within an ideal fluid. *Soviet Physics-Doklady*, 6, 773–775.
- Jönsson, H., Nilsson, A., Petersson, F., Allers, M., & Laurell, T. (2005). Particle separation using ultrasound can be used with human shed mediastinal blood. *Perfusion*, 20, 39–43. doi: 10.1191/0267659105pf782oa.
- Kaduchak, G., Goddard, G., Salzman, G., Sinha, D., Martin, J. C., Kwiatkowski, C. S., & Graves, S. W. (2008). Ultrasonic Particle Concentration and Application in Flow Cytometry. *United States Patent*, 7, 340, 957.
- Kundt, A., & Lehmann, O. (1874). Longitudinal vibrations and acoustic figures in cylindrical columns of liquids. *Annalen der Physik und Chemie (Poggendorff's Annalen)*, 153, 1–11.
- Li, P., Mao, Z., Peng, Z., Zhou, L., Chen, Y., Huang, P-H., ... Huang, T. J. (2015). Acoustic separation of circulating tumor cells. *Proceedings of the National Academy of Sciences of the United States of America*, 112(16), 4970–4975. doi: 10.1073/pnas.1504484112.
- Petriz, J., Bradford, J. A., & Ward, M. D. (2017). No lyse no wash flow cytometry for maximizing minimal sample preparation.

- Methods (San Diego, Calif.)*, pii, S1046–2023(17)30159–30157. <https://doi.org/10.1016/j.jymeth.2017.12.012>.
- Piyasena, M. E., Suthanthiraraj, P. P. A., Applegate, R. W. Jr., Goumas, A. M., Woods, T. A., López, G. P., & Graves, S. W. (2012). Multinode Acoustic Focusing for Parallel Flow Cytometry. *Analytical Chemistry*, *84*, 1831–1839. doi: 10.1021/ac200963n.
- Ren, L., Chen, Y., Lia, P., Maa, Z., Huang, P.-H., Rufoa, J., ... Huang, T. J. (2015). A high-throughput standing surface acoustic wave (SSAW)-based cell sorter. *Lab on A Chip*, *15*(19), 3870–3879. doi: 10.1039/C5LC00706B.
- Roos, M. S., & Apfel, R. E. (1988). Application of 30-MHz acoustic scattering to the study of human red blood cells. *Journal of the Acoustical Society of America*, *83*, 1639–1644. doi: 10.1121/1.395918.
- van den Engh, G. (2000). High speed cell sorting. In *Emerging Tools for Single-Cell Analysis: Advances in Optical Measurement Technologies* (pp. 21–48). G. Durack, & J. P. Robinson (Eds.), New York: John Wiley and Sons.
- Wiklund, M. (2012). Acoustofluidics 12: Biocompatibility and cell viability in microfluidic acoustic resonators. *Lab on A Chip*, *12*, 2018–2028. doi: 10.1039/c2lc40201g.
- Yasuda, K., Haupt, S. S., & Unemura, S. (1997). Using acoustic radiation force as a concentration method for erythrocytes. *The Journal of the Acoustical Society of America*, *102*, 642–645. doi: 10.1121/1.421009.

# Light-Triggered Drug Release from Red Blood Cells Suppresses Arthritic Inflammation

Emilia M. Zywot, Natalia Orlova, Song Ding, Rishi R. Rampersad, Emily M. Rabjohns, Victoria A. Wickenheisser, Qunzhao Wang, Joshua G. Welfare, Lauren Haar, Amanda M. Eudy, Teresa K. Tarrant,\* and David S. Lawrence\*

Arthritis is a leading cause of disability in adults, which can be intensely incapacitating. The location and intensity of the pain is both subjective and challenging to manage. Consequently, patient-directed delivery of anti-inflammatories is an essential component of future therapeutic strategies for the management of this disorder. The design and application of a light-responsive red blood cell (RBC)-conveyed dexamethasone (Dex) construct that enables targeted drug delivery upon illumination of the inflamed site is described. The red wavelength (650 nm) responsive nature of the phototherapeutic is validated using tissue phantoms mimicking the light absorbing properties of various skin types. Furthermore, photoreleased Dex has the same impact on cellular responses as conventional Dex. Murine RBCs containing the photoactivatable therapeutic display comparable circulation properties as fluorescently labeled RBCs. In addition, a single dose of light-targeted Dex delivery is fivefold more effective in suppressing inflammation than the parent drug, delivered serially over multiple days. These results are consistent with the notion that the circulatory system be used as an on-command drug depot, providing the means to therapeutically target diseased sites both efficiently and effectively.


## 1. Introduction

Joint pain and inflammation are a leading cause of disability among working age adults with staggering societal costs.<sup>[1]</sup> For

E. M. Zywot, N. Orlova, S. Ding, Q. Wang, L. Haar, D. S. Lawrence  
Division of Chemical Biology and Medicinal Chemistry  
University of North Carolina  
Chapel Hill, NC 27599, USA  
E-mail: lawrencd@email.unc.edu

R. R. Rampersad, E. M. Rabjohns, V. A. Wickenheisser, A. M. Eudy,  
T. K. Tarrant  
Department of Medicine  
Division of Rheumatology and Immunology  
Duke University  
Durham, NC 27710, USA  
E-mail: teresa.tarrant@duke.edu

J. G. Welfare, D. S. Lawrence  
Department of Chemistry  
University of North Carolina  
Chapel Hill, NC 27599, USA

 The ORCID identification number(s) for the author(s) of this article can be found under <https://doi.org/10.1002/adtp.202100159>

DOI: 10.1002/adtp.202100159

example, the economic burden associated with arthritis is estimated to be greater than \$300 billion in the United States alone.<sup>[2]</sup> As a consequence of the persistent nature of these diseases, frequent and long-term therapeutic administration is required, which results in moderate to severe undesired side effects. Furthermore, the therapeutic needs are accentuated during periods of profoundly increased disease activity, which can be intensely debilitating. Efforts to improve efficacy and reduce undesired systemic toxicity have focused on technologies, which can selectively deliver therapeutics to inflamed joints.<sup>[3,4]</sup> Indeed, it has been known for decades that the direct injection of glucocorticoids into arthritic joints provides temporary benefits;<sup>[5]</sup> however, multiple injections into joints on a routine basis is not an acceptable therapeutic option.<sup>[3]</sup> Nonetheless, the repeated delivery of therapeutic agents to afflicted joints is required to silence local inflammation and repair damage.<sup>[6]</sup> A stimuli-responsive drug

delivery system could potentially be used to intermittently dispense therapeutic agent(s) at the diseased site in a patient-directed, as-needed, fashion. Specifically, light as a stimulus enjoys a number of potentially useful attributes, including that it can be easily focused on inflamed and painful joints using readily available 600 to 1000 nm laser and light-emitting diode (LED) light sources.<sup>[7]</sup> A light-activated form of an anti-inflammatory agent, such as dexamethasone (Dex), would ideally be maintained in the circulatory system in an inactive state, and subsequently released using light by the patient when needed. Indeed, the circulatory system represents an opportune drug depot since all cells in the human body are positioned within 100  $\mu\text{m}$  of a blood vessel. However, repeated delivery to inflamed joints over the course of days or weeks requires a circulatory presence significantly longer than the half-life (a few hours) of the parent drug. We have addressed this issue by installing a photoactivatable Dex inside red blood cells (RBCs) and have employed these engineered cells to successfully treat a mouse model of inflammatory arthritis. For clinical relevance, the overwhelming majority of RBC drug loading studies have been performed with human erythrocytes (hRBCs). However, in preparation for animal studies, loaded mouse RBCs were also formulated and characterized.



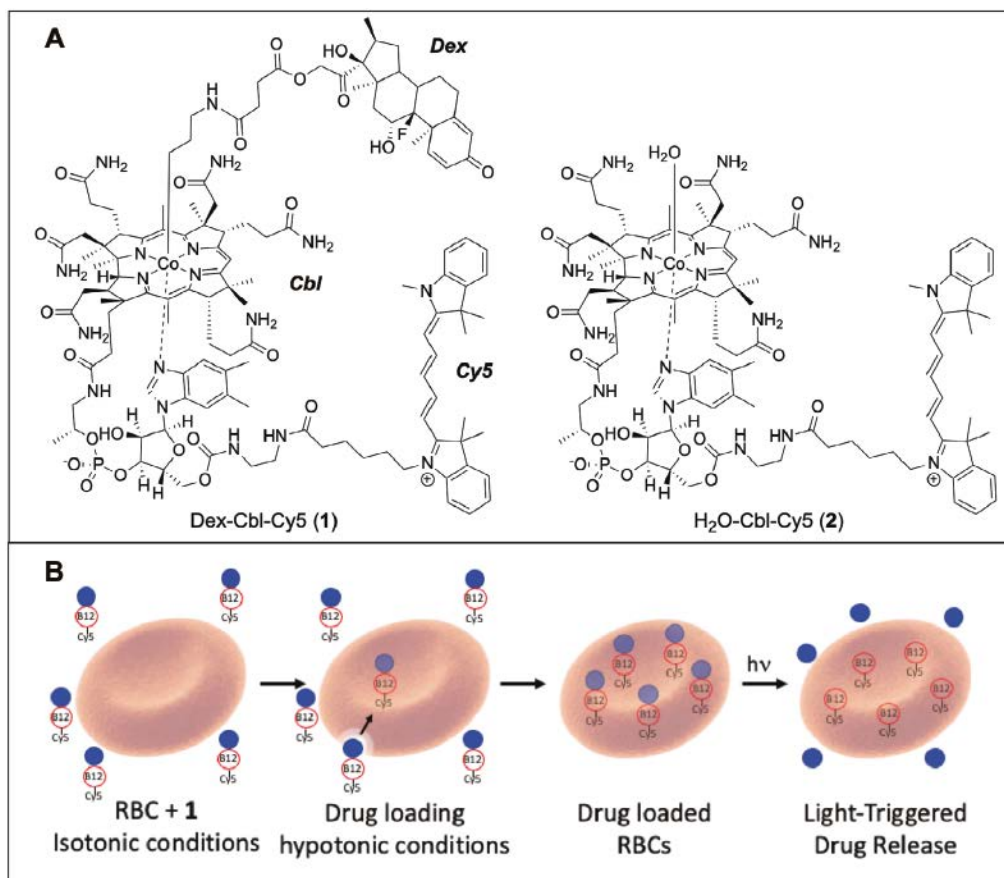


**Figure 1.** Assembly of Dex-Cbl-Cy5 RBC phototherapeutics. A) Structures of photoactivatable Dex-Cbl-Cy5 (1) and control compound H<sub>2</sub>O-Cbl-Cy5 (2). B) Schematic representation of the isotonic-to-hypotonic-to-isotonic method by which phototherapeutics are loaded into RBCs and subsequently photochemically released. Dex is represented by the blue sphere. Pore formation in the RBC membrane occurs in the presence of **1** or **2** under hypotonic conditions (4 °C for 40 min). Pores are subsequently resealed by direct addition of high salt followed by incubation at 37 °C for 20 min. Conjugates **1** or **2** remain trapped inside the RBC due to the membrane impermeability of the B12 anchor. Upon photolysis of the C–Co bond, the now membrane permeable Dex is released from the RBC carrier.

## 2. Results and Discussion

### 2.1. Design of a Circulating Photoresponsive Anti-Inflammatory Drug Depot

Novel therapies designed to maintain Dex's circulatory presence while minimizing its systemic side effects employ slow release carrier-based systems such as liposomes, polymeric-drug conjugates, and RBCs.<sup>[8]</sup> Of these carriers, RBCs present a potentially elegant solution to the challenge of creating a long-term drug depot that circulates throughout the body in an innocuous, dormant form.<sup>[9,10]</sup> Indeed, internally loaded RBCs have been reported to circulate for at least 1 month.<sup>[10]</sup> The strategy outlined herein employs engineered RBCs that stably house a Dex derivative that is released upon exposure to red light (650 nm). A key element of the design strategy is the covalent attachment of Dex to vitamin B12 (cobalamin, Cbl), where Cbl serves three roles (Figure 1A).<sup>[11]</sup> First, Cbl is membrane impermeable, which ensures that the internally loaded Drug-Cbl is retained by the RBC (Figure 1B). Second, Dex is appended to the central Co of Cbl via a light cleavable C–Co bond. Exposure to the appropriate wavelength severs Dex from the Cbl anchor, enabling the drug to freely diffuse out

of the RBC. Third, although the corrin ring of Cbl absorbs only short wavelength light (330–575 nm), installation of Cy5 on the Cbl<sup>[12–14]</sup> adjusts photorelease of the appended drug to a longer, tissue-penetrating wavelength (650 nm).<sup>[15]</sup>

#### 2.1.1. Synthesis of Cbl Conjugates

Both Dex-Cbl-Cy5 (**1**) and H<sub>2</sub>O-Cbl-Cy5 (**2**) (Figure 1A) were synthesized and introduced into RBCs to assess drug photodelivery as a potential therapeutic strategy for the treatment of inflammatory arthritis. H<sub>2</sub>O-Cbl-Cy5 serves as an inactive control that lacks the Dex therapeutic agent. In brief, Dex was appended to the aminopropyl ligand on the Co and Cy5 subsequently coupled to an ethylenediamine linker on the ribose of Cbl (Schemes S1 and S2 and Figures S1–S4, Supporting Information). The Cy5 fluorophore extends the light capturing wavelengths of Cbl from 330–575 nm to 650 nm, where the latter displays greater tissue penetration than that of the former (Figure S5, Supporting Information).<sup>[11,13]</sup> LC-MS analysis of the resulting mixture after photolysis of Dex-Cbl-Cy5 confirms the expected photoproducts,

**Table 1.** Mean corpuscular volume (MCV), mean cell hemoglobin (MCH), and mean corpuscular hemoglobin concentration (MCHC) in human and mouse RBCs. Data presented as mean  $\pm$  SD,  $n = 3$ ; where NA = not applicable and Q = quantitative.

| Properties                  | Native <sup>a)</sup> | DiI <sup>a)</sup> | 1 <sup>a)</sup> | 2 <sup>a)</sup> | Native <sup>b)</sup> | DiI <sup>b)</sup> | 1 <sup>b)</sup> | 2 <sup>b)</sup> |
|-----------------------------|----------------------|-------------------|-----------------|-----------------|----------------------|-------------------|-----------------|-----------------|
| MCV [fL]                    | 98 $\pm$ 5           | 100 $\pm$ 1       | 70 $\pm$ 7      | 76 $\pm$ 5      | 34 $\pm$ 1           | 36 $\pm$ 3        | 29 $\pm$ 3      | 33 $\pm$ 4      |
| MCH [pg]                    | 28 $\pm$ 2           | 30 $\pm$ 1        | 18 $\pm$ 1      | 21 $\pm$ 2      | 13 $\pm$ 1           | 14 $\pm$ 1        | 8 $\pm$ 1       | 8 $\pm$ 1       |
| MCHC [g dL <sup>-1</sup> ]  | 29 $\pm$ 1           | 30 $\pm$ 1        | 25 $\pm$ 3      | 28 $\pm$ 2      | 38 $\pm$ 1           | 40 $\pm$ 1        | 27 $\pm$ 4      | 23 $\pm$ 1      |
| Cell recovery after loading | NA                   | Q                 | Q               | Q               | NA                   | Q                 | 25–50%          | 25–50%          |

<sup>a)</sup> Human RBCs; <sup>b)</sup> Mouse RBCs.

namely free Dex and H<sub>2</sub>O-Cbl-Cy5 (Scheme S3 and Figure S5, Supporting Information).

### 2.1.2. Assembly of Phototherapeutic RBCs

RBCs internally loaded with either 1 or 2 were prepared using a hypotonic swelling procedure (Figure 1B).<sup>[11,12,16]</sup> Exposure of RBCs to a low ionic strength buffer solution induces cell swelling and pore formation within the cell membrane, which enables otherwise impermeable compounds to enter RBCs. The pores are subsequently resealed upon exposure to a high salt solution to reestablish an isotonic environment, which internally entraps the Cbl derivatives inside the RBCs (Figures S6 and S7, Supporting Information).<sup>[17]</sup> Although loading conditions are well established for hRBCs, mouse RBCs (mRBCs) are less stable than their human counterparts as demonstrated by their accelerated hemolysis and aging.<sup>[11,18]</sup> We found that modification of the established loading protocol improves the stability of the loaded mRBCs.<sup>[19]</sup> Key optimized parameters include lengthening the drug loading and membrane resealing times, the high salt addition to return the RBCs to an isotonic environment, and the presence of adenosine triphosphate (ATP) (see the Experimental Section for details).<sup>[20]</sup>

### 2.2. Characterization of Phototherapeutic RBCs

The hRBCs and mRBCs loaded with 1 or 2 were assessed for overall volume and hemoglobin content, cellular distribution of the phototherapeutic, and loading homogeneity and quantity of Dex in RBCs. The results from these studies were compared with those obtained for unmodified RBCs and for RBCs surface-loaded with the lipidated indocarbocyanine fluorophore DiI (1,1'-dioctadecyl-3,3,3',3'-tetramethylindocarbocyanine perchlorate;  $\lambda_{\text{ex}}$  550 nm,  $\lambda_{\text{em}}$  570 nm). DiI is noncovalently anchored via insertion of the lipid tails into the outer membrane sheath of the RBC. In addition, the DiI surface-loaded cells were used as a control circulation population serving as a comparison to internally loaded RBCs for in vivo studies (Figure S8, Supporting Information).<sup>[21]</sup> Specifically, no pores were opened in the membrane of DiI surface-loaded cells and, as a consequence, their internal contents are not perturbed. The mean corpuscular volume (MCV), mean corpuscular hemoglobin (MCH), and mean corpuscular hemoglobin concentration (MCHC) of both hRBCs and mRBCs were assessed by automated hemocytometry (Table 1).<sup>[22]</sup>

RBCs internally loaded with 1 or 2 are smaller and contain less hemoglobin on average than native RBCs. As expected, RBCs that

are surface loaded with DiI display values similar to native RBCs (Table 1). Trends are comparable for both mRBCs and hRBCs, consistent with the notion that opening and resealing RBCs results in the loss of some of the intracellular contents. In addition, although the recovery of hRBCs following loading is essentially quantitative, a significantly lower recovery was obtained for mRBCs. These results are consistent with the observation that hRBCs are more stable, under ex vivo conditions, than their murine counterparts.<sup>[11]</sup>

Imaging flow cytometry was used to qualitatively visualize the various RBC populations and to quantitatively assess changes in diameter and SSC (side light scattering) (Figure S9, Supporting Information). These studies confirm that RBCs containing either 1 or 2 exhibit a decrease in both size (diameter) and a decreasing shift in the SSC compared to native or DiI surface-loaded RBCs (Figure 2B,C,E,F). The decrease in diameter of internally loaded RBCs is consistent with hemocytometry MCV analysis and suggests that loss of some of the hemoglobin during the drug loading process is responsible for the smaller cell size. SSC is commonly related to the internal complexity (microparticles) of the cell. Since RBCs are presumed to have a relatively homogenous refractive index,<sup>[23]</sup> this implies that the refractive index is altered upon the partial replacement of hemoglobin with the Cbl conjugates 1 or 2.

We also assessed the uniformity of drug loading in RBCs and quantified the amount of Dex loaded. Fluorescent imaging flow cytometry revealed a uniform peak of loaded 1 and slightly less uniform 2 in hRBCs and mRBCs (Figure S10, Supporting Information). The amount of Dex-Cbl-Cy5 and H<sub>2</sub>O-Cbl-Cy5 loaded was quantified by ethanol extraction of loaded RBC pellets and subsequent measurement of the absorbance of Cy5 at 649 nm (Figures S11 and S12, Supporting Information). mRBCs contain 0.4  $\mu\text{g}$  Dex in 100  $\mu\text{L}$  of a mRBC pellet. Approximately 5% of Dex is loaded into RBCs.

### 2.3. Red Light Stimulates the Release of Dex from RBCs

We subsequently examined the light-triggered release of Dex from loaded hRBCs, which was quantified by LC-MS (Figure 3A; Figure S13 and Scheme S3, Supporting Information). In addition, following treatment, the RBC-containing solution was centrifuged and the presence of free Dex was examined in both the pellet and the supernatant. We did not detect free Dex in the absence of illumination (Figure 3A). By contrast, 5 min exposure to a 645 nm light source released the vast majority (90  $\pm$  5.8%) of Dex that had been loaded into RBCs, consistent with the notion

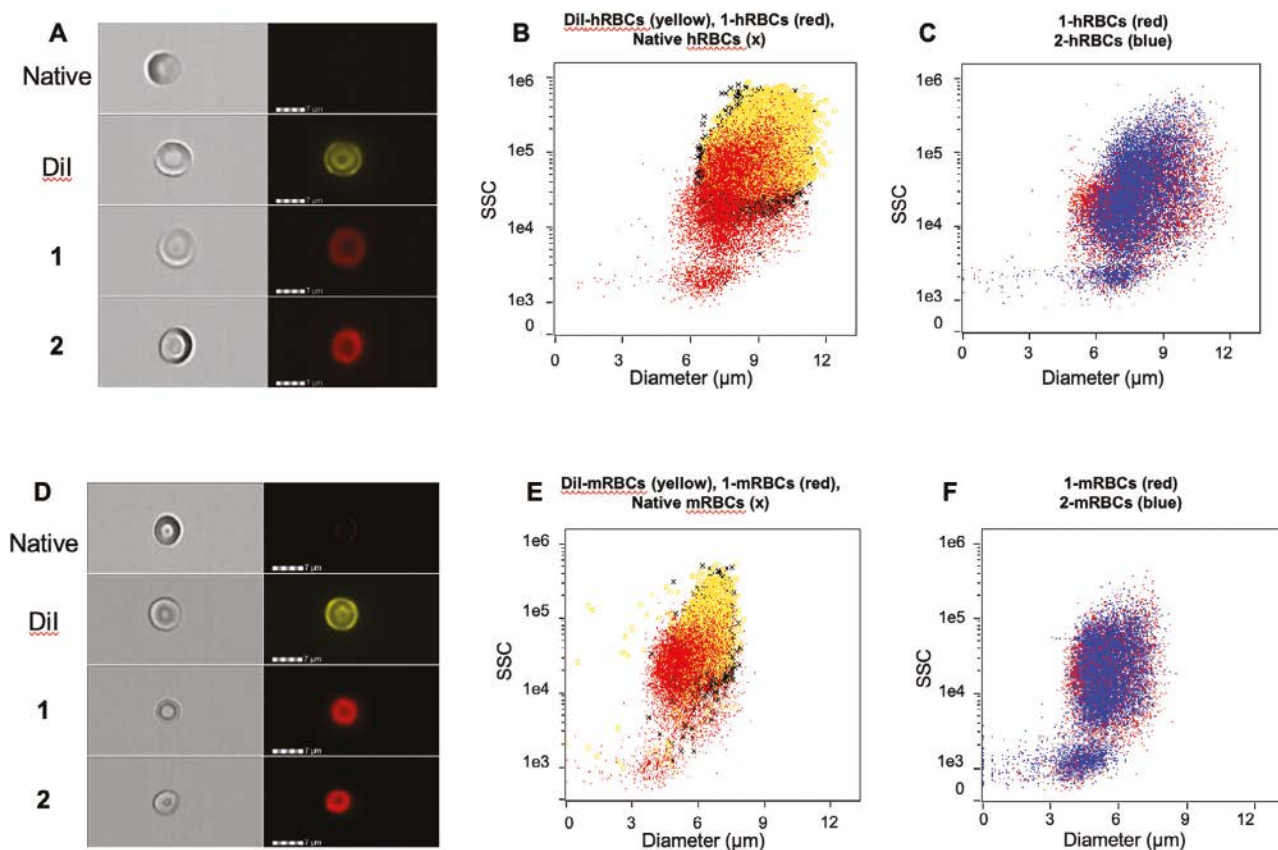


**Figure 2.** Characterization of native and loaded RBCs. A) Imaging flow cytometry of hRBCs. Bright-field images (left) and fluorescent images (right) of native, surface-loaded (Dil), and internally loaded (**1** or **2**) hRBCs. Scale bar represents 7  $\mu\text{m}$ . B,C) Plot of SSC versus diameter of loaded hRBCs. B) hRBCs loaded with **1** (red) display a greater variability in SSC compared to Dil (yellow) and native hRBCs (black x). C) hRBCs loaded with **2** (blue) exhibit morphological changes comparable to those displayed by hRBCs containing **1** (red). D) Imaging flow cytometry of mRBCs. Bright-field images (left) and fluorescent images (right) of native, surface-loaded (Dil), and internally loaded (**1** or **2**) mRBCs. Scale bar represents 7  $\mu\text{m}$ . E,F) Plot of SSC versus diameter of loaded mRBCs. E) mRBCs loaded with **1** (red) display a greater variability in SSC compared to surface-loaded Dil (yellow) and native mRBCs (black x). F) mRBCs loaded with **2** (blue) exhibit morphological changes comparable to those displayed by mRBCs containing **1** (red). The minor population of cells with the low SSCs in panels (B)–(F) are likely RBC ghosts.<sup>[24]</sup> Imaging data was used to calculate the diameter of each cell/event as previously described.<sup>[25]</sup>

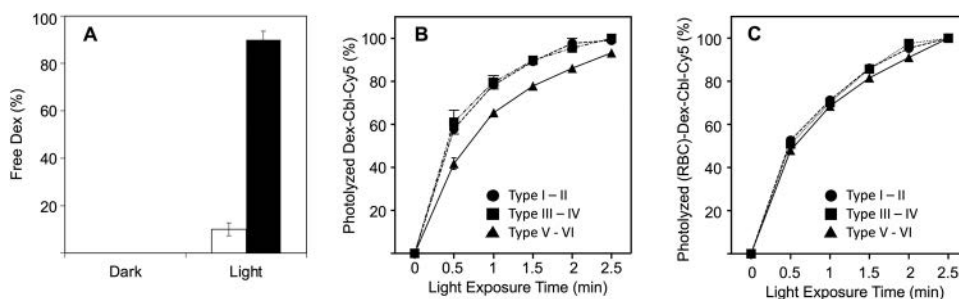


**Figure 3.** Photolysis of Dex-Cbl derivatives and release from hRBCs. A) hRBCs containing **1** were kept in the dark or exposed to 645 nm light for 5 min. Following illumination, the RBCs were centrifuged and the presence of free Dex in the supernatant (black bars) and pellet (white bars) was quantified via LC-MS. Free Dex is not detected in the absence of illumination whereas, upon illumination,  $90 \pm 5.8\%$  of free Dex is present in the supernatant. In addition, the photolyzed byproduct,  $\text{H}_2\text{O-Cbl-Cy5}$  (**2**) is not detected in the supernatant. B) Illumination (645 nm) of a buffered solution of **1** in the presence of Fitzpatrick phantom solutions. After 2 min of light exposure, there was no significant difference detected in Dex-Cbl-Cy5 photolysis with any of the Fitzpatrick types as measured by one-way ANOVA ( $n = 3$ , NS). C) Illumination (645 nm) of **1** embedded in hRBCs in the presence of Fitzpatrick phantom solutions. After 2 min of light exposure, there was no significant difference detected in Dex-Cbl-Cy5 photolysis from RBCs with any of the Fitzpatrick types as measured by one-way ANOVA ( $n = 3$ , NS). All samples were illuminated with a light intensity of  $1.0 \text{ mW cm}^{-2}$  for up to 6 min.

that Dex, once released from the membrane impermeable Cbl, is free to diffuse out of the cellular carrier (Figure 3A). Our previous studies with an alkyl-Cbl-Cy5 derivative revealed a quantum yield of  $\approx 0.1$ .<sup>[26]</sup>

The Dex-Cbl-Cy5 phototherapeutic is designed to respond to red photons, which are not as extensively absorbed by tissue as compared to blue light. Indeed, wavelengths in the far red/near IR achieve tissue depths of up to several cm under optimized conditions.<sup>[27]</sup> We explored the relative efficacy of Dex photorelease from Dex-Cbl, which lacks a red light absorbing antenna, and Dex-Cbl-Cy5, in the presence of the Fitzpatrick series of tissue phantoms. The latter are devised to mimic the tissue absorbing properties of human skin color, from lightly to heavily pigmented (Figure 3B,C).<sup>[26,28]</sup> We examined the photolysis of **1** filtered through Fitzpatrick skin phantom solutions that reproduced the properties of light (Type I–II; [melanin] =  $8.8 \mu\text{g mL}^{-1}$ ), brown (Type III–IV; [melanin] =  $66 \mu\text{g mL}^{-1}$ ), and dark (Type V–VI; [melanin] =  $130 \mu\text{g mL}^{-1}$ ) skin.<sup>[26]</sup> Illumination (510 nm) through the Fitzpatrick phantoms fails to produce significant photolysis of a buffered solution of Dex-Cbl (Scheme S4 and Figure S14, Supporting Information). Nearly 90% of Dex-Cbl is unphotolyzed even after 6 min of illumination in the presence of type I/II Fitzpatrick phantom (Figure S15, Supporting Information). As expected, tissue phantoms containing greater melanin concentrations are even more effective at blocking photolysis. By contrast, analogous experiments performed at 645 nm with **1** result in the near complete photolysis after only 3 min (Figure 3B). Finally, we examined the photorelease (645 nm) of Dex from hRBCs containing **1** in the presence of the tissue phantoms (Figure 3C). Reassuringly, illumination triggers the rapid photolysis of **1** and subsequent release of Dex from RBCs.

### 2.3.1. Photoreleased Dex Triggers Glucocorticoid Receptor $\alpha$ Translocation

Our initial studies on the potential therapeutic efficacy of photoactivatable Dex were performed on a variety of cultured human cells. Dex mediates its therapeutic action via the glucocorticoid receptor  $\alpha$  (GR $\alpha$ ), which is normally found in the cytoplasm but localizes to the nucleus in response to glucocorticoid binding.<sup>[29]</sup> Upon entry into the nucleus, GR $\alpha$  associates with glucocorticoid-responsive elements and stimulates or represses target gene expression.<sup>[29,30]</sup> We assessed the ability of Dex, photoreleased from RBCs bearing **1**, to trigger GR $\alpha$  in HeLa cells and primary fibroblast-like synoviocytes (FLSs). HeLa cells were used as a model cell line due to their established sensitivity to conventional Dex (Figure S16, Supporting Information).<sup>[31]</sup> In contrast, FLS are nonimmune cells that participate in rheumatoid arthritis (RA) pathogenesis. The FLS employed in this study were collected and cultured from RA patients.

Both HeLa and FLS cells were exposed to hRBCs bearing **1** in the dark and at 660 nm. In addition, RBCs containing **2** (i.e., no Dex) was used as a negative control and Dex itself was employed as a positive control. HeLa cells respond in a manner consistent with literature precedent (Figure 4A).<sup>[31]</sup> In the absence of 660 nm exposure, GR $\alpha$  is primarily retained in the cytoplasm in untreated HeLa cells and in cells co-incubated with hRBCs con-

taining either **1** or **2**. By contrast, robust GR $\alpha$  nuclear localization is clear in Dex exposed HeLa cells. Analogous experiments were performed in the presence of 660 nm light. Untreated HeLa cells, as well as those co-incubated with hRBCs containing **2** (negative control), fail to display a nuclear GR $\alpha$  migration. However, hRBCs loaded with **1** trigger the anticipated GR $\alpha$  migration in a fashion consistent with that observed with the parent glucocorticoid. These experiments were recapitulated using primary FLS cells from RA patients. We do note that FLS cells are phenotypically heterogeneous<sup>[32]</sup> and do not display the near 100% uniform GR $\alpha$  nuclear migration observed with HeLa cells. However, both 660 nm exposed hRBCs bearing **1**, and Dex itself, trigger the same degree of GR $\alpha$  relocation in FLS cells (Figure 4B; Figures S17 and S18, Supporting Information).

### 2.3.2. Photoreleased Dex Does Not Impact FLS Viability

Glucocorticoids are known to induce apoptosis in certain cell types, which serves as both a mechanism of action for anti-inflammatory effects as well as a contributor to certain negative side effects (such as osteoporosis).<sup>[29]</sup> With this in mind, we examined the impact that free Dex, or hRBCs containing **1** or **2**, have on Dex resistant and sensitive cells. FLS cells experience minimal growth inhibition in response to treatment with Dex (Figures S19 and S20, Supporting Information). The viability of FLS cells is likewise minimally impacted upon exposure to illuminated hRBCs bearing either **1** or **2** (Figure 4C). However, unlike synoviocytes, B cells are known to be sensitive to Dex (Figures S21 and S22, Supporting Information).<sup>[33]</sup> We examined the effect of hRBCs loaded with either **1** or **2**, in the presence of 660 nm light, on Sup-B15 lymphoma B cell viability. As expected, both Dex photoreleased from Dex-Cbl-Cy5 hRBCs, as well as the parent drug (Dex), impact B cell viability (Figure 4C). These results suggest that Dex, delivered to the site of inflammation, should reduce the localized immune response responsible for symptoms associated with arthritis. Furthermore, since synoviocytes play a key role in producing extracellular components of the synovial fluid, it is reassuring that the photorelease of Dex from RBCs does not impact FLS viability.

## 2.4. Photoactivated Treatment of Collagen Antibody-Induced Arthritis in a Mouse Model

### 2.4.1. The Circulatory Integrity of Internally and Externally Modified RBCs Is Similar

The circulatory integrity of modified RBCs was examined with a 1:1 mixture of two mRBC populations: i) internally loaded with H<sub>2</sub>O-Cbl-Cy5 (**2**) and ii) surface-loaded with DiI (Figure 5A). A mixture of the two populations were tail vein injected into mice and a blood sample was subsequently acquired after 20 min. Flow cytometry revealed that both cell types constitute  $\approx 3\%$  of all circulating RBCs. Subsequent blood sampling after 1 h revealed insignificant loss of circulating modified RBCs, indicating that Dex-loaded mRBCs circulate to the same extent as their fluorophore surface labelled counterparts.



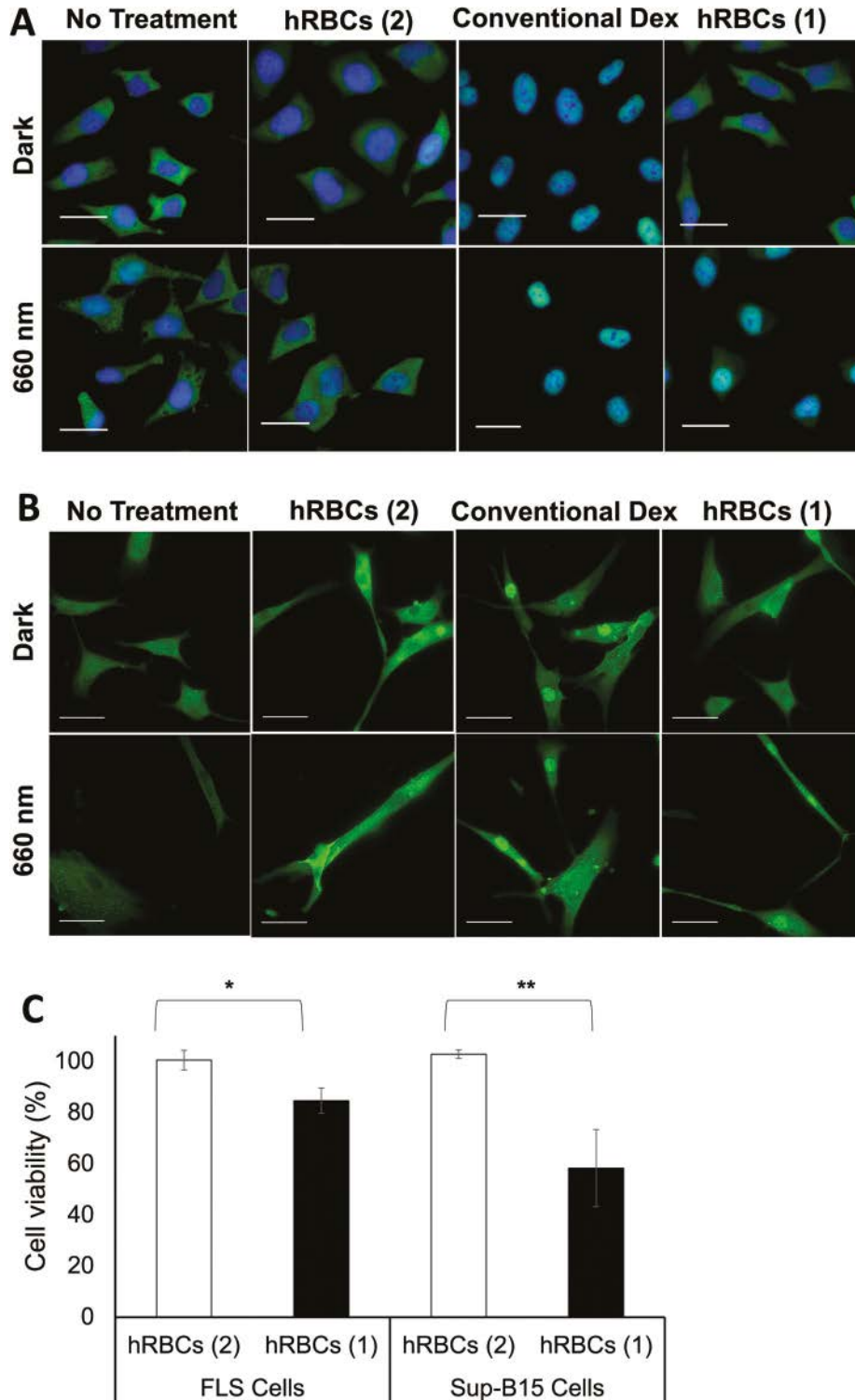


**Figure 4.** Efficacy and toxicity of Dex-Cbl-Cy5 hRBCs. A) Immunocytochemical analysis of GR $\alpha$  nuclear localization in HeLa cells. HeLa cells were cultured in serum free media for 24 h and then left untreated (column 1), exposed to hRBCs containing **2** (column 2), Dex ( $250 \times 10^{-9}$  M; column 3), or hRBCs containing **1** (column 4) in the absence (row 1) or presence of 660 nm light (row 2). Cells were fixed and permeabilized, exposed to anti-GR $\alpha$ , and subsequently antirabbit secondary antibodies conjugated to Alexa Fluor 488 (green). Cells were also labeled with the nuclear Hoescht 33342 stain (blue). Images display merged green and blue channels where scale bars represent 30  $\mu$ m (representative 1 of 5). B) Immunocytochemical analysis of GR $\alpha$  nuclear localization in FLS cells. FLS cells were exposed to the conditions for HeLa cells as described above without serum starvation. Scale bars represent 50  $\mu$ m (representative 1 of 4). C) The effect of 660 nm illuminated hRBCs loaded with **1** or **2** on the viability of FLS and Sup-B15 B cells. hRBC treatments with **1** have a modest impact on FLS cell viability, but a more substantial effect on Sup-B15 cells ( $n = 3$ , \* $P < 0.05$  and \*\* $P < 0.01$ ).



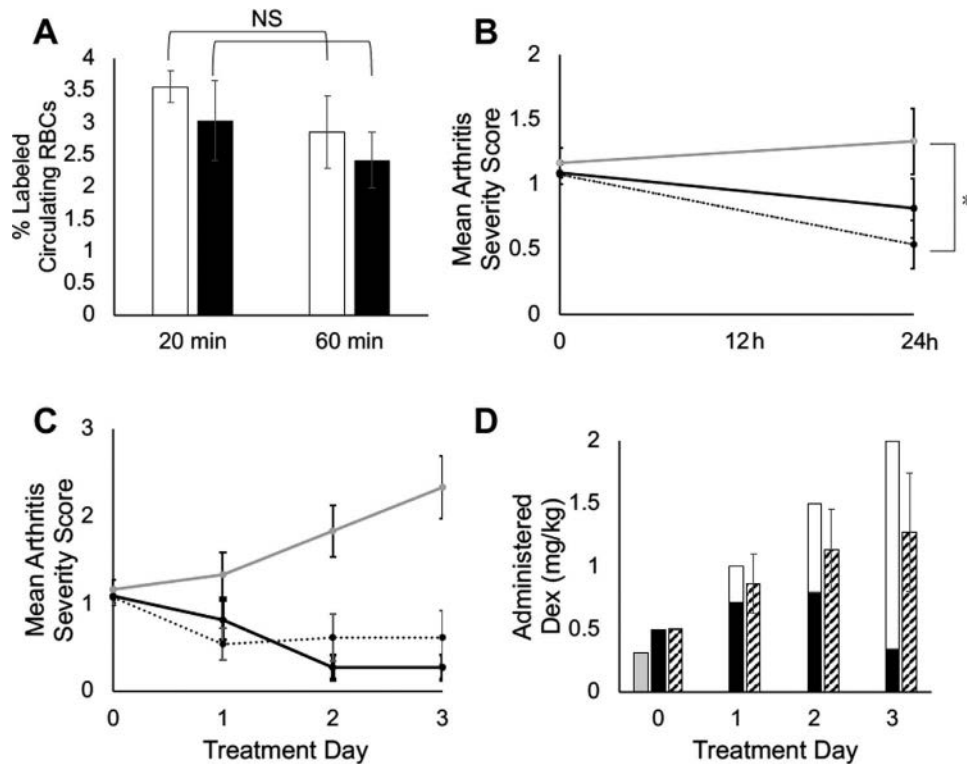


**Figure 5.** Light-stimulated Dex treatment of CAIA mice. A) Percent of loaded mRBCs circulating in mice ( $n = 3$ ) at 20 and 60 min. White bars represent control surface-loaded Dil RBCs, while black bars represent RBCs containing **2**. Statistical analysis confirmed no significant change in circulating Dil or RBCs containing **2** over 1 h (NS = not significant,  $P > 0.1$ ). B) There is significantly less inflammation ( $^*P = 0.01$ ) in mice treated with RBCs containing **1** (dotted line) than mice exposed to RBCs loaded with **2** (gray line) after the first 24 h of treatment. IP Dex serves as a positive treatment control (black line) but does not achieve a statistically significant improvement at 24 h. C) Over multiple days, mice treated with mRBCs loaded with **1** and treated with serial laser (dotted line,  $n = 13$ ) continued to maintain remission of inflammation while arthritis in IP Dex treated mice (black line,  $n = 11$ ,) improved after 1–4 injections, depending on the individual mouse. Mice in both treatment groups (mRBCs containing **1**, IP Dex) display a comparable response to therapy ( $P = 0.09$ ), and both groups are significantly different from the illuminated-daily inactive control (**2**) loaded mRBCs group, which continue to worsen (gray line,  $n = 12$ ) despite daily laser treatment ( $P < 0.0002$ ). D) Shaded bars furnish the ratio of mice that received additional doses (black) of IP Dex over the treatment course to achieve remission and the cumulative dose received. Dex from loaded mRBCs (gray,  $n = 13$ ) is compared to the average IP Dex (hatched,  $n = 11$ ). Mice treated with **1** loaded mRBCs only required 1 intravenous infusion on day 0 and subsequent daily laser application to the arthritic paw to achieve remission of inflammation (gray). The RBC group containing **1** received 78% less Dex ( $\text{mg kg}^{-1}$ ) than mice treated with IP Dex to achieve similar clinical remission of inflammation ( $P < 0.0001$ ).

#### 2.4.2. Phototherapeutic RBCs Suppress Inflammation in an Arthritic Mouse Model

The phototherapeutic efficacy of mRBCs containing **1** was evaluated using the collagen-antibody induced arthritis (CAIA) mouse model. CAIA is an accepted animal model of inflammatory arthritis,<sup>[34]</sup> including a dependence on inflammatory mononuclear cells in acute inflammation and joint erosion in end-stage disease.<sup>[35]</sup> Particular advantages to the CAIA model include its rapid onset and highly consistent penetrance of disease with minimal interexperimental variability.<sup>[36]</sup> CAIA was induced by an intraperitoneal (i.p.) injection of arthrogenic mAb 5-clone cocktail into DBA1/J mice on day 0 followed by i.p. injection of lipopolysaccharide (LPS) on day 2 according to manufacturer instructions. Arthritis was measured daily by a blinded observer using a clinical disease score index 0–4, where 0 = normal paw; 1 = mild but definite swelling of the ankle or digits; 2 = moderate redness and swelling of an ankle  $\pm$  any number of digits; 3 = moderate redness and swelling of the entire paw; and 4 =

maximal redness and swelling of the entire paw and digits, with or without ankylosis.<sup>[37]</sup> CAIA mice were tail vein injected with a 90% hematocrit of allogenic, strain-specific mRBCs containing **1** or **2** (negative control). A single arthritic paw was illuminated with a 3 mW 635 nm laser for 5 min (Scheme S5 and Figures S23 and S24, Supporting Information). In addition, a positive control treatment group was treated using a standard protocol<sup>[38]</sup> ( $0.5 \text{ mg kg}^{-1}$ ) dexamethasone sodium phosphate i.p. (“IP Dex”). Within 24 h following treatment, only mice exposed to mRBCs containing **1**, with illumination of the inflamed paw, displayed statistically diminished arthritic severity relative to animals treated with mRBCs containing **2** ( $P = 0.01$ ). By contrast, the difference in arthritic severity of laser treated paws of animals receiving IP Dex at 24 h was not significant when compared to inactive control **2** mRBC treatment (Figure 5B). If clinical paw swelling was still present in an IP Dex-treated mouse, IP Dex was continued in an individual mouse until clinical remission was achieved. Thus, IP Dex mice received between 1 and 4 doses of steroid, depending on severity of disease (Figure 5C). Specifically, on the second day

of treatment, 8 of 11 mice IP Dex mice had clinical inflammation and were treated with a second dose of IP Dex. Similarly, mice treated with RBCs containing **1** had serial laser treatments on the arthritic paw until clinical inflammation was resolved. All treatments were completed, and the experiment terminated after 4 days for all groups. The disease curves of both IP Dex and mRBCs containing **1** achieve statistical difference in arthritis severity when compared to the RBC **2** inactive control ( $P = 0.0001$  and  $P = 0.0002$ , respectively) and are comparable to each other ( $P = 0.9$ ). However, it is notable that 78% less Dex was administered in the single **1** mRBC treatment dose with serial laser treatments as compared to average systemic treatments of the IP Dex to achieve comparable remission (Figure 5D). It is also noteworthy that the RBC group containing **2** had progressive worsening of clinical inflammation in the paw that was treated with laser daily for 4 days (Figure 5C).

### 3. Conclusion

Arthritis therapies are constrained by 1) the failure to deliver sufficient drug quantities to the inflamed site to achieve the desired therapeutic effect, 2) the range of moderate to severe side effects associated with long-term systemic exposure, and 3) the inability of the patient to self-administer therapeutics in a site-targeted as-needed fashion. There is a compelling biomedical need to develop a technology to address these issues, especially given the chronic nature and prevalence of arthritis, the capricious acute episodes of pain and inflammation, interpatient heterogeneity, and different disease subtypes of arthritis that affect a broad swath of the population. We have developed a light activation strategy that triggers the delivery of the anti-inflammatory agent, Dex, in a site-specific fashion. Given the therapeutic potential established by clinical studies of internally loaded RBCs and the Red Cell Loader and ERY CAPS RBC loading devices, RBCs conveying a photoactivatable therapeutic offer the opportunity to target inflamed diseased sites in a patient-directed fashion by employing the circulatory system as a drug depot.<sup>[10,39]</sup> We have shown that RBCs harboring the phototherapeutic agent display properties similar to those of native and surface-labeled erythrocytes. Furthermore, given the red-light responsiveness of the carrier system, drug release is efficiently triggered through tissue phantoms that mimic the entire range of pale to dark skin types. We have demonstrated that the RBC-conveyed photo-anti-inflammatory agent not only induces the desired reduction in inflammation but does so at a dose that is significantly lower than the standard of care for the parent drug. Finally, we note that the inherent flexibility of the drug delivery platform, particularly with respect to designating the wavelength of photorelease, may ultimately enable a variety of arthritis drugs to be separately delivered to designated sites via wavelength modulation. These studies are in progress.

### 4. Experimental Section

*Synthesis of Dex-Cbl-Ethylenediamine (Dex-Cbl-EDA; Scheme S1, Supporting Information):* Succinyl-Dex<sup>[40]</sup> (0.041 mmol) was dissolved in dry DMF (5 mL) along with DIPEA (0.32 mmol) and HATU (0.047 mmol). The solution was stirred for 5 min to activate the carboxylic acid. After 5 min,

propylamine-Cbl-Fmoc (0.041 mmol) was added to the solution, and the reaction vessel was placed on a shake plate for 4 h. After 4 h, the solution was diluted with diethyl ether (to 50 mL) and spun down to pellet the product. Then, the supernatant was decanted. The Dex-Cbl-Fmoc pellet was allowed to dry for 4 h, and then dissolved in dry DMF (5 mL). Piperidine (0.29 mmol) was added to the solution to deprotect the Fmoc group. The solution was stirred for 4 h, and then diluted with diethyl ether (to 50 mL) to precipitate the product, which was pelleted via centrifugation. The pellet was dissolved in MeOH (10 mL) and then diluted with deionized (DI) water (to 40 mL). A 12 g Biotage C18 column with sample was prepped with 5:95 MeOH:H<sub>2</sub>O (0.1% TFA) and the solution was eluted using a MeOH:H<sub>2</sub>O (0.1% TFA) gradient from 10% to 80% MeOH. Fractions were analyzed for purity via LC-MS (Figure S1, Supporting Information) and combined, concentrated under reduced pressure, and lyophilized to yield a powdered orange solid. <sup>1</sup>H NMR (Figure S2, Supporting Information; 500 MHz, MeOH-d<sub>4</sub>).

*Synthesis of Dex-Cbl-Cy5 (1; Scheme S2, Supporting Information):* Cy5 (0.0204 g, 0.04 mmol) was dissolved in dry DMF (5 mL) creating a dark blue solution. DIPEA (0.0481 g, 0.37 mmol) and HATU (0.0113 g, 0.03 mmol) were added to solution and the reaction mixture was placed on a shake plate for 10 min. Dex-Cbl-Eda (0.0495 g, 0.025 mmol) was then added to the solution and the reaction vessel was shaken for an additional 2.5 h. The solution was diluted with diethyl ether (to 50 mL) and centrifuged to pellet the Cbl conjugate. Residual ether was removed by "air drying" for 4 h in the dark. The pellet was then dissolved in MeOH (4 mL) and diluted with DI H<sub>2</sub>O (to 15 mL). A 30 g Biotage C18 column with sample was prepped with MeOH:H<sub>2</sub>O (0.1% TFA) and the solution was eluted using a MeOH:H<sub>2</sub>O (0.1% TFA) gradient from 0% to 80% MeOH. Fractions were analyzed for purity via LC-MS (Figure S3, Supporting Information) and combined, concentrated under reduced pressure, and lyophilized to yield a blue solid (49.2 g, 80.2% yield). <sup>1</sup>H NMR (Figure S4, Supporting Information; 500 MHz, MeOH-d<sub>4</sub>).

*Encapsulation of 1 and 2 in mRBCs:* Mouse blood was collected from DBA-1J mice, and the RBCs immediately isolated by filtering through Ficol-Paque at 400 × g for 30 min. The serum and white blood cells were removed and packed mRBCs were washed three times with 1× PBS at 500 × g for 4 min. RBCs were then immediately loaded with Cbl derivatives as previously described with slight modifications to allow for stable loading of larger RBC pellets.<sup>[11]</sup> Most commonly, mRBC pellets (400 μL, 100% hematocrit) were prepared for loading by addition of a solution of **1** (13.8 × 10<sup>-3</sup> M, 8 μL) or **2** (19 × 10<sup>-3</sup> M, 6 μL) in DMSO and diluent C (164 μL) to create a mixture of mRBCs (70% hematocrit) and Cbl conjugate (200 × 10<sup>-6</sup> M). The RBC/Cbl mixture was dialyzed for 40 min in 400 mL of dialysis buffer (80 mOsm L<sup>-1</sup> PBS, 0.25% glycerol, 10 × 10<sup>-3</sup> M glucose, 2 × 10<sup>-3</sup> M ATP) at 4 °C. RBCs were removed from dialysis tubing and resealed by adding 0.1 volume 10× PBS per vol of dialyzed RBCs and by incubating for 20 min at 37 °C. Loaded, resealed RBCs were washed 5× with 1× PBS or 3× with 1× PBS and 2× with FBS. All manipulations of light-responsive compounds occurred in the dark room to prevent exposure to ambient light. The entire isolation and loading of mRBCs was completed within 6 h.

*Imaging Flow Cytometry:* RBCs loaded with the Cbl conjugates **1** or **2** or surface-loaded with Dil were washed with 1× PBS and then diluted 1000-fold with 1× PBS to achieve a concentration of 9 × 10<sup>7</sup> RBCs mL<sup>-1</sup>. Loaded cells were then evaluated using the ImageStreamX Mark II (Amnis, Seattle, USA). Samples were run at a speed of 25 μL min<sup>-1</sup> and 100 000 unique cells were imaged in two bright-field channels (intensities of 64.6 and 93.94 mW), a side scatter channel (785 nm laser at an intensity of 2 mW with a 740–800 nm filter), a Dil channel (488 nm solid state laser at an intensity of 200 mW with a 560–595 nm filter), and a Cy5 Channel (658 nm diode laser at an intensity of 150 mW with a 660–740 nm filter) at 60× magnification. Cells were gated, first filtering for focus by requiring a gradient root mean square greater than 60, then analyzing for singlet cells using a gate within an Area versus Aspect Ratio scatter plot (Figure S9, Supporting Information). The fluorescence of the cells was then analyzed using an intensity histogram of the appropriate fluorescence channel. General morphology of cells was analyzed by comparing cells using the diameter feature (Erode mask, pixel 03) as established in previous

methods and intensity of channel 6 (the side scatter channel).<sup>[25]</sup> Images were analyzed using the IDEAS Software. Characterization of mRBCs was performed on the same day as their isolation and loading.

**Automated Hemocytometry:** hRBCs were prepared as 10% hematocrit hRBC samples as described above and then analyzed via the Siemens Advia 2120i - automated CBC. RBCs were sphered and fixed and then automatically processed through a Flowcell where RBC Count, MCV, and hemoglobin content were measured using a laser diode. Hemoglobin was measured in a colorimeter by lysing all RBCs to free hemoglobin. The free hemoglobin was converted to methemoglobin and then porphyrin and the color change was measured at 546 nm. MCH was calculated by the analyzer using the following equation:  $MCH = Hgb \times 10/RBC$ . mRBCs were prepared as 10% hematocrit mRBC samples as described above. Samples were then analyzed using the IDEXX ProCyt Dx automated hematology instrument (software version 00-34 Build57) using settings for mouse whole blood. Cell recovery was assessed by measuring the RBC pellet volume before and after loading.

**Photorelease of Dex from Dex-Cbl-Cy5 (1) hRBCs (Scheme S3, Supporting Information):** Dex-Cbl-Cy5 (loaded into hRBCs, 20% hematocrit in human platelet rich plasma, 500  $\mu$ L) were photolyzed as described below. Release of Dex into supernatant after photolysis was assessed by extracting Dex from plasma and pellet with acetonitrile followed by LC-MS analysis, comparing photolyzed product fragment ion 510 and 373 in the supernatant and pellet. Exposure to the light source was performed 5–10 min so that Dex-Cbl-Cy5 was fully photolyzed, as revealed by the absence of unphotolyzed starting material via LC-MS (Figure S13, Supporting Information).

**Photolysis of Dex-Cbl-Cy5 (1) and Dex-Cbl with Fitzpatrick Skin Phantom Solutions:** Fitzpatrick skin phantom solutions were prepared following a previously reported protocol.<sup>[26]</sup> Hematocrit lysate stock solution (25% hematocrit) was prepared via sonicated lysis of RBCs in water followed by centrifuge to remove residual membranes. All skin phantom solutions contained 0.3% v/v Intralipid, 1% hemoglobin, and erythrocyte lysate solution (1% v/v) in PBS. Melanin stock solution (synthetic melanin from Sigma-Aldrich;  $\epsilon$  at 645 nm  $\approx 1-3$  mg  $mL^{-1}$   $cm^{-1}$ ; 3 mg  $mL^{-1}$  in  $100 \times 10^{-3}$  M  $NH_4OH$  solution) was added at varying concentrations depending on Fitzpatrick skin type (I–II  $\approx 8.8$   $\mu$ g  $mL^{-1}$ ; III–IV  $\approx 66$   $\mu$ g  $mL^{-1}$ ; V–VI  $\approx 130$   $\mu$ g  $mL^{-1}$ ). The skin phantom solution was inserted between the sample and the light source before illumination. Dex-Cbl ( $20 \times 10^{-6}$  M in MeOH/PBS 1:1, 200  $\mu$ L) or Dex-Cbl-Cy5 ( $20 \times 10^{-6}$  M in MeOH/PBS 1:1, 100  $\mu$ L) were placed in a cuvette and illuminated with an Oriol Xe Flash lamp (Model 60000) with a 510 nm filter (Newport 10BPF10-510, band width 10 nm) for Dex-Cbl and a 645 nm filter (Newport HPM645-50, band width 50 nm) for Dex-Cbl-Cy5. The sample was exposed to a light intensity of 1.0 mW  $cm^{-2}$ . For Dex-Cbl, the progress of photolysis was monitored by observing an absorbance increase at 350 nm as previously described.<sup>[41]</sup> For Dex-Cbl-Cy5, the progress of photolysis was monitored by observing the fluorescence decrease using at 675 nm (with  $\lambda_{ex}$  at 645 nm). Completion of photolysis was confirmed by LC-MS. Analogous experiments were conducted using Dex-Cbl-Cy5-loaded human RBCs (20% hematocrit in human platelet rich plasma, 100  $\mu$ L), which were added to 0.5 mL of human platelet rich plasma (Zen-Bio, Inc). Photolysis of the samples was performed using an Oriol Xe Flash lamp (Model 60000) (800 mJ, 62 Hz) as the light source with selective bandpass filters for  $645 \pm 10$  for 5 min (dark samples were incubated in the dark for 5 min). Photolyzed RBC suspensions were centrifuged at  $1000 \times g$  for 3 min, and the supernatant was then analyzed by LC-MS (solvent A: 0.1% formic acid/ $H_2O$ ; solvent B: 0.1% formic acid/methanol). The pellet was extracted with 0.5 mL of acetonitrile and analyzed by LC-MS as well. The photolyzed Dex product was monitored by its fragment ions 510 (Dex-aldehyde) and 373 (hydrolyzed Dex) and compared with standard photolyzed product from photolysis in PBS/MeOH (1:1). Acetonitrile was added to the supernatant in a 1:1 ratio, centrifuged at  $21\,000 \times g$  for 5 min, and removed from the pellet.

**GR $\alpha$  Localization in Human Cells:** Human HeLa or FLS cells were seeded in 24-well glass-bottom plates treated with polylysine at a density of  $5 \times 10^4$  cells  $mL^{-1}$  and allowed to adhere overnight. HeLa cells were then serum starved for 24 h while FLS cells were immediately treated after adhering overnight. The cell cultures were subsequently exposed to 100  $\mu$ L of

RBCs-(1) at 10% hematocrit ( $7.9 \times 10^8$  cells  $mL^{-1}$ ), or 100  $\mu$ L of RBCs-(2) at 10% hematocrit ( $8.5 \times 10^8$  cells  $mL^{-1}$ ), or 500  $\mu$ L Dex at  $250 \times 10^{-9}$  M, or 500  $\mu$ L ethanol vehicle in plain DMEM using Millicell Hanging Cell Culture Inserts (1  $\mu$ m, polyethylene terephthalate, Millipore). Light treated samples were exposed to a 660 nm LED board for 30 min at RT. After 30 min of exposure, hanging wells were removed and cells were incubated for an additional 30 min at 37  $^\circ$ C in a humidified environment at 5%  $CO_2$ . Cells were then washed 3 $\times$  with 1 $\times$  PBS, fixed with 4% PFA in PBS for 10 min, washed with 2  $\times$  1 $\times$  PBS (1 mL), and treated with methanol for 5 min. Fixed cells were treated with a blocking buffer (5% Donkey serum; 0.1% Triton X-100; PBS) and stained for GR $\alpha$  using monoclonal rabbit anti-GR $\alpha$  antibody (Abcam 181327) at 1:200 dilution in antibody dilution buffer (1% BSA; 0.1% Triton-X-100; PBS). Cells were then washed with PBS (3  $\times$  5 min) while stirring before incubation with anti-rabbit AlexaFluor 488 secondary antibody (Life Technologies A11034) at 1:500 dilution in antibody dilution buffer for 1 h at room temperature. Cells were washed (1  $\times$  5 min) with PBS and imaged on an inverted Olympus IX81 microscope equipped with a Hamamatsu FLASH 4V3, 60 $\times$  oil objective, and a FITC filter cube (Semrock). Images were analyzed using ImageJ. FLS cells and quantified using ImageJ's Coloc 2 program. Regions of Interest (created from the Hoechst nuclear stain) were analyzed for colocalization between the Hoechst nuclear stain and anti-GR $\alpha$  488 fluorescence in the nuclear space. Pearson's coefficients without thresholding were analyzed from four replicates (Figure S18, Supporting Information).

**Cell Viability upon Exposure to Dex:** Sup-B15 and FLS cell seeding densities were optimized to ensure cells linearly responded to MTS (Figures S19 and S20, Supporting Information). Sup-B15 cells were then seeded in 24-well glass-bottom plates at a density of  $1.7 \times 10^6$  cells  $mL^{-1}$  and allowed to settle for 1 h, while primary FLS cells were plated at a density of  $1 \times 10^4$  cells  $mL^{-1}$  and allowed to adhere overnight. Cells were then treated with 100  $\mu$ L of RBCs-(1) at 50% hematocrit ( $4.45 \times 10^9$  cells  $mL^{-1}$ ), or 100  $\mu$ L of RBCs-(2) at 50% hematocrit ( $4.3 \times 10^9$  cells  $mL^{-1}$ ), or 500  $\mu$ L free Dex at  $2 \times 10^{-6}$  M, or 500  $\mu$ L plain DMEM, which was added to wells in Millicell Hanging Cell Culture Inserts (1  $\mu$ m, polyethylene terephthalate, Millipore). Samples were exposed to a 660 nm LED board for 30 min at RT. After 30 min of exposure, hanging wells were removed and cells were incubated for 24 h at 37  $^\circ$ C in a humidified environment at 5%  $CO_2$ . Cells were then treated with 100  $\mu$ L MTS/1 mL media for 2 h (Abcam 197010) after which absorption at 492 nm was measured using a HTS 7000 BioAssay Reader (Perkin Elmer, Waltham, Ma).

**Assessment of Circulatory Viability of Modified mRBCs:** Whole blood of DBA-1J, 8–10 week, male donors was harvested on the day of loading by cardiac puncture. Internally loaded and control RBCs were prepared as described above. mRBCs loaded with 2 were resuspended in PBS at 50% hematocrit and 100  $\mu$ L of cell suspension was drawn into syringes circumferentially covered with tape to block light. Surface-loaded control mRBCs (Dil) and internally (2) loaded mRBCs were mixed 1:1 v/v and 100  $\mu$ L of the mixture was loaded in a syringe at 90% hematocrit and circumferentially taped to block light. Samples were injected into DBA-1J mice via the tail vein. At the described time points, blood was collected from mice via tail nicks. Mice were euthanized via  $CO_2$  inhalation according to approved UNC IACUC protocol #19-048.0. Whole blood was diluted  $\approx 1000$ –1500-fold and analyzed on the Attune NxT flow cytometer as described below.

**Attune NxT Flow Cytometry:** mRBCs loaded with the Cbl conjugates 1 or 2, or surface-loaded with Dil, or unmodified were diluted 1000-fold with 1 $\times$  PBS to achieve a concentration of  $1 \times 10^7$  RBCs  $mL^{-1}$ . Diluted samples were analyzed using the Attune NxT (ThermoFisher). First, a scatter plot of side scatter area (SSC-A) to side scatter height (SSC-H) was used to gate for single cells. Then, Cy5 from 2 was excited and measured using the 637 nm 100 mW laser and the RL1 detector (Mirror 654LP, Filter 670/14). Data were processed using FCS Express v.7.04 ensuring even flow of sample through the instrument by plotting time versus forward scatter area (FSC-A). Final data allowed for RBC size characterization via scatter plots of FSC-A versus SSC-A and loading uniformity via Cy5 fluorescence-RL1-area and Dil fluorescence-BL1-area.

**CAIA Animal Model:** CAIA was induced in forty-five 8–10 week old male DBA/1J mice via the i.p. injection of Chondrex Arthrogen-CIA 5-Clone Cocktail (1.6 mg per mouse) followed by an i.p. injection of

lipopolysaccharide from *Escherichia coli* (25 mg) 3 days later, as per the manufacturer's instructions. Arthritis was measured daily by a blinded observer with a clinical disease score index and measurement of paw swelling. The clinical disease score index was performed with the following scoring system: 0 = normal paw; 1 = mild but definite swelling of the ankle or digits; 2 = moderate redness and swelling of an ankle  $\pm$  any number of digits; 3 = moderate redness and swelling of the entire paw; and 4 = moderate redness and swelling of all three joints in the paw.<sup>[37,42]</sup> The maximum score/paw was 4. This method had been previously validated in inflammatory arthritis models.<sup>[42]</sup> Assessment of disease occurred while the mouse was anesthetized using isoflurane. All procedures performed were approved by the Institutional Animal Care and Use Committees of UNC-CH (#19-048.0) and Duke University Medical Center (#A185-17-08).

**Treatment of Mice with IP Dex or RBCs Containing 1 or 2 (Scheme S5, Supporting Information):** Mice were randomized after symptom onset in at least one paw with a clinical score  $\geq 1$  to one of three groups that received the following injections: mRBCs containing 1 delivered intravenously (1 mRBC; experimental treatment); mRBCs containing 2 delivered intravenously (2 mRBC; inactive control, no drug); or Dex sodium phosphate solution delivered i.p. (IP Dex; positive control). The 1 mRBC group received mRBCs (90% hematocrit, 100  $\mu$ L) internally loaded with  $\approx 0.0065$  mg Dex-Cbl-Cy5 (1), equivalent to 0.31 mg kg<sup>-1</sup> per mouse, and the IP Dex group received 0.5 mg kg<sup>-1</sup> per mouse. Individual mice in the IP Dex group with persistent disease would be treated with additional injections of 0.5 mg kg<sup>-1</sup> daily to achieve a clinical score of 0 in the arthritic paw. Injections of loaded RBCs were performed via the tail vein by a single, blinded technician using a 27G needle. A laser was applied to the first observed affected joint (only one paw per mouse) in all RBC groups for 5 min immediately following injection and each day until experiment termination at day 4. Mice were euthanized via CO<sub>2</sub> inhalation according to approved Duke IACUC protocol #A1851708. An RS laser diode (Power Technology Inc., Alexander AR, USA), 635 nm, 3 mW (Figure S23, Supporting Information) was used for laser treatment of the arthritic paw (clinical score  $\geq 1$ ). If two or more joints were simultaneously affected, then the laser-treated paw was selected at random. A single, blinded experimenter performed all laser treatments and both lower and upper extremity paws were treated in the study. The laser was applied to the selected joint at an angle that allowed for illumination of the entire joint and paw and was held in position for a total of 5 min per animal. Mice were anesthetized using isoflurane during laser treatment. Treatment was applied to the same paw daily from day of injection until termination.

**Statistical Analysis:** All plots were presented as the mean  $\pm$  standard deviation. Data were analyzed by an unpaired Student's *t* test. GraphPad Prism software was used for statistical analysis. A *P*-value of less than 0.05 was statistically significant. It had been previously demonstrated that 10 animals per group are needed to achieve 80% power to detect a medium effect size (0.22) at a 0.05 level of significance in the CAIA model.<sup>[42]</sup> There were >10 animals per group for each of the three experimental groups in this study. The area under the curve (AUC) of the arthritis severity score-time curve was calculated for laser paws in each treatment group. AUC differences were estimated by ANOVA. Comparisons were made across all three treatment groups, and pairwise comparisons were performed using Tukey's test based on the LSMEANS statement. All analyses were conducted using SAS 9.4 (Cary, North Carolina). A one-way ANOVA was used for comparing laser-paw treatment groups at 24 h and was found to be significant (*P* = 0.05). A subsequent Mann-Whitney *U* test comparing laser-paw Dex-Cbl-Cy5 (1) RBCs (*n* = 13) with H<sub>2</sub>O-Cbl-Cy5 (2) RBC control (*n* = 12) identified significant difference (*P* = 0.01) at 24 h, whereas IP DEX (*n* = 11) did not achieve statistical significance from the control. An unpaired *t*-test was used to analyze the cumulative steroid dose used to achieve clinical remission of the laser-treated paw between IP Dex (*n* = 11) mice and Dex-Cbl-Cy5 (1) RBCs (*n* = 13) mice, where IP Dex mice were treated daily with 0.5 mg kg<sup>-1</sup> IP until the arthritis subsided (ranging between 1 and 4 steroid doses + laser) and Dex-Cbl-Cy5 (1) RBC mice received a single dose (0.31 mg kg<sup>-1</sup> intracellularly loaded within 50% Hct) injected intravenously followed by daily laser for 3 additional days.

## Supporting Information

Supporting Information is available from the Wiley Online Library or from the author.

## Acknowledgements

D.S.L. and T.K.T. thank the Rheumatology Research Foundation and D.S.L. thanks the National Institutes of Health (1R01HL153744). E.M.Z. was supported from a T32 CA71341 training grant. Research reported in this publication was supported in part by the North Carolina Biotech Center Institutional Support Grants 2017-IDG-1025, 1UM2AI30836-01, and 1 S10 OD017984-01A1. The UNC Flow Cytometry Core Facility is supported in part by P30 CA016086 Cancer Center Core Support Grant to the UNC Lineberger Comprehensive Cancer Center. Animal clinical services were performed by the Animal Histopathology & Laboratory Medicine Core at the University of North Carolina, which is supported in part by an NCI Center Core Support Grant (5P30CA016086-41) to the UNC Lineberger Comprehensive Cancer Center. Animal studies were performed within the UNC Lineberger Animal Studies Core Facility and Duke Division of Laboratory Animal Resources at the University of North Carolina at Chapel Hill and Duke University, respectively. The UNC Lineberger Animal Studies Core is supported in part by an NCI Center Core Support Grant (P30 CA16086) to the UNC Lineberger Comprehensive Cancer Center.

## Conflict of Interest

The authors declare no conflict of interest.

## Data Availability Statement

Research data are not shared.

## Keywords

arthritis, dexamethasone, drug delivery, photoactivatable therapeutics, red blood cells

Received: July 20, 2021

Revised: October 1, 2021

Published online:

- [1] K. A. Theis, D. W. Roblin, C. G. Helmick, R. Luo, *Disabil. Health J.* **2018**, *11*, 108.
- [2] Centers for Disease Control and Prevention, <https://www.cdc.gov/chronicdisease/resources/publications/factsheets/arthritis.htm> (accessed: July 2021).
- [3] S. Mitragotri, J. W. Yoo, *Arch. Pharmacol Res.* **2011**, *34*, 1887.
- [4] a) W. Ulbrich, A. Lamprecht, *J. R. Soc., Interface* **2010**, *7*, S55; b) J. Bullock, S. A. A. Rizvi, A. M. Saleh, S. S. Ahmed, D. P. Do, R. A. Ansari, J. Ahmed, *Med. Princ. Pract.* **2018**, *27*, 501; c) C. Fiehn, *Clin. Exp. Rheumatol.* **2010**, *28*, S40.
- [5] J. L. Hollander, E. M. Brown Jr., R. A. Jessar, C. Y. Brown, *J. Am. Med. Assoc.* **1951**, *147*, 1629.
- [6] A. Reum Son, D. Y. Kim, S. Hun Park, J. Yong Jang, K. Kim, B. Ju Kim, X. Yun Yin, J. Ho Kim, B. Hyun Min, D. Keun Han, M. Suk Kim, *Sci. Rep.* **2015**, *5*, 14713.
- [7] V. A. Wickenheisser, E. M. Zywoot, E. M. Rabjohns, H. H. Lee, D. S. Lawrence, T. K. Tarrant, *Curr. Allergy Asthma Rep.* **2019**, *19*, 37.



- [8] F. Lühder, H. M. Reichardt, *Int. J. Mol. Sci.* **2017**, *18*, 1836.
- [9] a) S. Ding, C. P. O'Banion, J. G. Welfare, D. S. Lawrence, *Cell Chem. Biol.* **2018**, *25*, 648; b) X. Han, C. Wang, Z. Liu, *Bioconjugate Chem.* **2018**, *29*, 852; c) L. Koleva, E. Bovt, F. Ataullakhanov, E. Sinauridze, *Pharmaceutics* **2020**, *12*, 276; d) T. Hanley, R. Vankayala, C.-H. Lee, J. C. Tang, J. M. Burns, B. Anvari, *Biomolecules* **2021**, *11*, 729; e) D. Sun, J. Chen, Y. Wang, H. Ji, R. Peng, L. Jin, W. Wu, *Theranostics* **2019**, *9*, 6885.
- [10] V. Bourgeaux, J. M. Lanao, B. E. Bax, Y. Godfrin, *Drug Des., Dev. Ther.* **2016**, *10*, 665.
- [11] C. M. Marvin, S. Ding, R. E. White, N. Orlova, Q. Wang, E. M. Zywot, B. M. Vickerman, L. Harr, T. K. Tarrant, P. A. Dayton, D. S. Lawrence, *Small* **2019**, *15*, 1901442.
- [12] R. M. Hughes, C. M. Marvin, Z. L. Rodgers, S. Ding, N. P. Oien, W. J. Smith, D. S. Lawrence, *Angew. Chem., Int. Ed. Engl.* **2016**, *55*, 16080.
- [13] T. A. Shell, D. S. Lawrence, *Acc. Chem. Res.* **2015**, *48*, 2866.
- [14] T. A. Shell, J. R. Shell, Z. L. Rodgers, D. S. Lawrence, *Angew. Chem., Int. Ed. Engl.* **2014**, *53*, 875.
- [15] a) R. Weinstein, T. Slanina, D. Kand, P. Klan, *Chem. Rev.* **2020**, *120*, 13135; b) H. Kobayashi, M. Ogawa, R. Alford, P. L. Choyke, Y. Urano, *Chem. Rev.* **2010**, *110*, 2620.
- [16] V. Bourgeaux, J. M. Lanao, B. E. Bax, Y. Godfrin, *Drug Des., Dev. Ther.* **2016**, *10*, 665.
- [17] A. V. Gothoskar, *Pharm. Technol.* **2004**, *28*, 140.
- [18] A. T. Makley, M. D. Goodman, L. A. W. Friend, J. A. Johannigman, W. C. Dorlac, A. B. Lentsch, T. A. Pritts, *Shock* **2010**, *34*, 40.
- [19] a) F. Pierigè, N. Bigini, L. Rossi, M. Magnani, *Wiley Interdiscip. Rev.: Nanomed. Nanobiotechnol.* **2017**, *9*, e1454; b) G. L. Dale, D. G. Villacorte, E. Beutler, *Biochem. Med.* **1977**, *18*, 220; c) J. Deloach, G. Ihler, *Biochim. Biophys. Acta* **1977**, *496*, 136.
- [20] H. Aujla, M. Wozniak, T. Kumar, G. J. Murphy, REDJUVENATE Investigators, *Vox Sang.* **2018**, *113*, 509 <https://onlinelibrary.wiley.com/doi/full/10.1111/vox.12666>.
- [21] a) S. R. Stowell, J. S. Liepkalns, J. E. Hendrickson, K. R. Girard-Pierce, N. H. Smith, C. M. Arthur, J. C. Zimring, *J. Immunol.* **2013**, *191*, 5013; b) R. Mukthavaram, G. Shi, S. Kesari, D. Simberg, *J. Controlled Release* **2014**, *183*, 146.
- [22] K. Doig, B. Zhang, *Clin. Lab. Sci.* **2017**, *30*, 173.
- [23] C. Martinez-Torres, B. Laperrousaz, L. Berguiga, E. Boyer-Provera, J. Elezgaray, F. E. Nicolini, V. Maguer-Satta, A. Arneodo, F. Argoul, *J. Biomed. Opt.* **2015**, *20*, 096005.
- [24] J. Pichler, D. Printz, D. Scharner, D. Trbojevic, J. Siekmann, G. Fritsch, *Cytometry* **2002**, *50*, 231.
- [25] S. M. Johnson, A. Banyard, C. Smith, A. Mironov, M. G. McCabe, *Int. J. Mol. Sci.* **2020**, *21*, 8723.
- [26] Z. L. Rodgers, R. M. Hughes, L. M. Doherty, J. R. Shell, B. P. Molesky, A. M. Brugh, M. D. Forbes, A. M. Moran, D. S. Lawrence, *J. Am. Chem. Soc.* **2015**, *137*, 3372.
- [27] C. E. Tedford, S. DeLapp, S. Jacques, J. Anders, *Lasers Surg. Med.* **2015**, *47*, 312.
- [28] a) A. N. Sharma, B. C. Patel, *StatPearls*, StatPearls Publishing, Treasure Island, FL **2021**; b) A. E. Karsten, J. E. Smit, *Photochem. Photobiol.* **2012**, *88*, 469; c) J. E. Smit, A. F. Grobler, R. W. Sparrow, *Photochem. Photobiol.* **2011**, *87*, 64.
- [29] R. S. Hardy, K. Raza, M. S. Cooper, *Nat. Rev. Rheumatol.* **2020**, *16*, 133.
- [30] S. Ramamoorthy, J. A. Cidowski, *Rheum Dis. Clin. North Am.* **2016**, *42*, 15.
- [31] A. G. Karra, M. Konstantinou, M. Tzortziou, I. Tsialtas, F. D. Kalousi, C. Garagounis, J. M. Hayes, A. G. Psarra, *Int. J. Mol. Sci.* **2018**, *20*, 94.
- [32] P. V. Kasperkovitz, T. C. Timmer, T. J. Smeets, N. L. Verbeet, P. P. Tak, L. G. van Baarsen, B. Baltus, T. W. Huizinga, E. Pieterman, M. Fero, G. S. Firestein, T. C. van der Pouw Kraan, C. L. Verweij, *Arthritis Rheum.* **2005**, *52*, 430.
- [33] a) K. Andreau, C. Lemaire, V. Souvannavong, A. Adam, *Immunopharmacology* **1998**, *40*, 67; b) D. Lill-Elghanian, K. Schwartz, L. King, P. Fraker, *Exp. Biol. Med.* **2002**, *227*, 763.
- [34] a) G. Kollias, P. Papadaki, F. Apparailly, M. J. Vervoordeldonk, R. Holmdahl, V. Baumans, C. Desaintes, J. Di Santo, J. Distler, P. Gar-side, M. Hegen, T. W. Huizinga, A. Jungel, L. Klareskog, I. McInnes, I. Ragoussis, G. Schett, B. Hart, P. P. Tak, R. Toes, W. van den Berg, W. Wurst, S. Gay, *Ann. Rheum. Dis.* **2011**, *70*, 1357; b) R. Dinser, *Best Pract. Res., Clin. Rheumatol.* **2008**, *22*, 253; c) K. K. Keller, L. M. Lindgaard, L. Wogensen, F. Dagnaes-Hansen, J. S. Thomsen, S. Sakaguchi, K. Stengaard-Pedersen, E. M. Hauge, *Rheumatol. Int.* **2013**, *33*, 1127; d) N. Sakaguchi, T. Takahashi, H. Hata, T. Nomura, T. Tagami, S. Yamazaki, T. Sakihama, T. Matsutani, I. Negishi, S. Nakat-suru, S. Sakaguchi, *Nature* **2003**, *426*, 454.
- [35] K. S. Nandakumar, R. Holmdahl, *Arthritis Res. Ther.* **2006**, *8*, 223.
- [36] T. K. Tarrant, P. Liu, R. R. Rampersad, D. Esserman, L. R. Rothlein, R. G. Timoshchenko, M. W. McGinnis, D. J. Fitzhugh, D. D. Patel, A. M. Fong, *Arthritis Rheum.* **2012**, *64*, 1379.
- [37] L. M. Khachigian, *Nat. Protoc.* **2006**, *1*, 2512.
- [38] J. J. Inglis, G. Criado, M. Medghalchi, M. Andrews, A. Sandison, M. Feldmann, R. O. Williams, *Arthritis Res. Ther.* **2007**, *9*, R113.
- [39] C. H. Villa, A. C. Anselmo, S. Mitragotri, V. Muzykantov, *Adv. Drug Delivery Rev.* **2016**, *106*, 88.
- [40] A. D. McLeod, D. R. Friend, T. N. Tozer, *J. Pharm. Sci.* **1994**, *83*, 1284.
- [41] A. Juzeniene, Z. Nizauskaite, *J. Photochem. Photobiol., B.* **2013**, *122*, 7.
- [42] a) P. M. Giguere, M. J. Billard, G. Laroche, B. K. Buckley, R. G. Timoshchenko, M. W. McGinnis, D. Esserman, O. Foreman, P. Liu, D. P. Siderovski, T. K. Tarrant, *Mol. Immunol.* **2013**, *54*, 193; b) T. K. Tarrant, M. J. Billard, R. G. Timoshchenko, M. W. McGinnis, D. S. Serafin, O. Foreman, D. A. Esserman, N. J. Chao, W. E. Lento, D. M. Lee, D. Patel, D. P. Siderovski, *J. Leukocyte Biol.* **2013**, *94*, 1243.



# Cell-Based Therapy for Canavan Disease Using Human iPSC-Derived NPCs and OPCs

Lizhao Feng, Jianfei Chao, E Tian, Li Li, Peng Ye, Mi Zhang, Xianwei Chen, Qi Cui, Guihua Sun, Tao Zhou, Gerardo Felix, Yue Qin, Wendong Li, Edward David Meza, Jeremy Klein, Lucy Ghoda, Weidong Hu, Yonglun Luo, Wei Dang, David Hsu, Joseph Gold, Steven A. Goldman, Reuben Matalon, and Yanhong Shi\*

Canavan disease (CD) is a fatal leukodystrophy caused by mutation of the aspartoacylase (ASPA) gene, which leads to deficiency in ASPA activity, accumulation of the substrate N-acetyl-L-aspartate (NAA), demyelination, and spongy degeneration of the brain. There is neither a cure nor a standard treatment for this disease. In this study, human induced pluripotent stem cell (iPSC)-based cell therapy is developed for CD. A functional ASPA gene is introduced into patient iPSC-derived neural progenitor cells (iNPCs) or oligodendrocyte progenitor cells (iOPCs) via lentiviral transduction or TALEN-mediated genetic engineering to generate ASPA iNPC or ASPA iOPC. After stereotactic transplantation into a CD (Nur7) mouse model, the engrafted cells are able to rescue major pathological features of CD, including deficient ASPA activity, elevated NAA levels, extensive vacuolation, defective myelination, and motor function deficits, in a robust and sustainable manner. Moreover, the transplanted mice exhibit much prolonged survival. These genetically engineered patient iPSC-derived cellular products are promising cell therapies for CD. This study has the potential to bring effective cell therapies, for the first time, to Canavan disease children who have no treatment options. The approach established in this study can also benefit many other children who have deadly genetic diseases that have no cure.

## 1. Introduction

Canavan disease (CD) is a rare, autosomal recessive neurodevelopmental disorder that affects children from infancy.<sup>[1]</sup> Most children with infantile-onset CD, the most prevalent form of the disease, will die within the first decade of life. There is neither a cure nor a standard treatment for this disease. CD is caused by genetic mutation in the aspartoacylase (ASPA) gene, which encodes a metabolic enzyme synthesized by oligodendrocytes in the brain.<sup>[1]</sup> The ASPA enzyme breaks down N-acetyl-aspartate (NAA), an amino acid derivative in the brain. The cycle of production and breakdown of NAA appears to be critical for maintaining the white matter of the brain, which consists of nerve fibers covered by myelin. Mutation of the ASPA gene results in a deficiency in the ASPA enzyme, which in turn leads to accumulation of the NAA substrate, spongy degeneration (vacuolation), and myelination defect in the brain. The clinical symptoms

Dr. L. Feng, Dr. J. Chao, Dr. E Tian, Dr. L. Li, Dr. P. Ye, Dr. M. Zhang, Dr. X. Chen, Dr. Q. Cui, Dr. T. Zhou, G. Felix, Dr. Y. Qin, Dr. W. Li, E. D. Meza, J. Klein, Dr. L. Ghoda, Prof. Y. Shi  
Division of Stem Cell Biology Research  
Department of Developmental and Stem Cell Biology  
Beckman Research Institute of City of Hope  
1500 E. Duarte Rd., Duarte, CA 91010, USA  
E-mail: yshi@coh.org

Dr. G. Sun  
Diabetes and Metabolism Research Institute at City of Hope  
1500 E. Duarte Rd., Duarte, CA 91010, USA


G. Felix  
Irell & Manella Graduate School of Biological Sciences  
Beckman Research Institute of City of Hope  
1500 E. Duarte Rd., Duarte, CA 91010, USA

Dr. W. Hu  
Department of Molecular Imaging and Therapy  
Beckman Research Institute of City of Hope  
1500 E. Duarte Rd., Duarte, CA 91010, USA

Dr. Y. Luo  
Department of Biomedicine  
Aarhus University  
Aarhus 8000, Denmark

Dr. W. Dang, Dr. D. Hsu, Dr. J. Gold  
Center for Biomedicine and Genetics  
Beckman Research Institute of City of Hope  
1500 E. Duarte Rd., Duarte, CA 91010, USA

Prof. S. A. Goldman  
Center for Translational Neuromedicine  
University of Rochester Medical Center  
Rochester, NY 14642, USA

 The ORCID identification number(s) for the author(s) of this article can be found under <https://doi.org/10.1002/advs.202002155>

© 2020 The Authors. Published by Wiley-VCH GmbH. This is an open access article under the terms of the Creative Commons Attribution License, which permits use, distribution and reproduction in any medium, provided the original work is properly cited.

DOI: 10.1002/advs.202002155

of CD include impaired motor function, mental retardation, and early death.<sup>[2]</sup>

There is currently no approved therapy for this condition. The closest therapeutic candidate under clinical development for this disease is the delivery of a functional *ASPA* gene directly into the brain via adeno-associated viral (AAV) transduction<sup>[3]</sup> or liposome-mediated transfection.<sup>[4]</sup> The AAV product has undergone a phase 1 clinical trial with 13 patients, while the liposome *ASPA* gene transfer has been tested in 2 patients. The results of the studies showed reasonable safety profiles, however, the clinical benefits to the patients were limited.<sup>[3,4]</sup> There is a clear, unmet medical need for an effective therapy for CD.

Stem cell technology holds great promise for the treatment of intractable human diseases. Several clinical trials are ongoing using cells derived from human embryonic stem cells or human induced pluripotent stem cells.<sup>[5]</sup> iPSCs could provide an autologous and expandable donor source for the generation of specific somatic cell types and tissues from individual patients.<sup>[6]</sup> Furthermore, patient-specific iPSCs are tailored to specific individuals, and therefore could reduce the potential for immune rejection. Neural progenitor cells (NPCs) have been used in clinical trials and shown a favorable safety profile.<sup>[7]</sup> The high expandability and short differentiation time<sup>[8]</sup> make iPSC-derived NPCs (iNPCs) a desirable cell source for cell therapy.

Because CD is a demyelination disease with oligodendrocyte loss in the brain of CD patients, oligodendrocyte progenitor cells (OPCs), the precursor cells of oligodendrocytes, could also be a good candidate for CD cell therapy.<sup>[9]</sup> OPCs have been successfully derived from human iPSCs.<sup>[10]</sup> They are highly migratory after intracerebral engraftment, and can differentiate into oligodendrocytes and myelinate dysmyelinated loci throughout the brain.<sup>[10a,b,11]</sup>

In this study, we developed good manufacturing practice (GMP)-compatible processes for human iPSC derivation, expansion, and differentiation. We generated iPSCs from CD patients and differentiated CD iPSCs into iNPCs using GMP-compatible processes we established. A functional *ASPA* gene was introduced into CD iNPCs by lentiviral transduction. The resultant *ASPA* iNPCs were transplanted into the brains of an immunodeficient CD (Nur7) mouse model. The efficacy and preliminary safety of the transplanted *ASPA* iNPCs were evaluated. Furthermore, we introduced a wild type *ASPA* gene into a defined locus in CD iPSCs by TALEN-mediated gene editing. These gene-edited iPSCs were further differentiated into OPCs. The resultant *ASPA* iOPCs were also transplanted into CD (Nur7) mouse brains to determine their efficacy and preliminary safety.

## 2. Results

### 2.1. Manufacturing Canavan Disease Patient iPSCs and Differentiating Them into iNPCs

The objective of this study is to establish human iPSC-based cell therapies for CD. We have demonstrated that research-grade NPCs derived from CD patient iPSCs that were transduced with a wild type *ASPA* gene are able to ameliorate disease phenotypes in a CD (Nur7) mouse model in our developmental stage study. In order to move the therapeutic candidate to the clinic, we developed GMP-compatible processes to manufacture the CD patient iPSC-derived cellular product, in order to transfer the processes to GMP manufacturing. We established a GMP-compatible process to derive human iPSCs by episomal reprogramming<sup>[12]</sup> in an integration-free, xeno-free, and feeder-free manner. We further developed methods to expand human iPSCs and differentiate them iNPCs under chemically defined, xeno-free, and feeder-free, GMP-compatible conditions.

We derived iPSCs from fibroblasts generated from six CD patients using the GMP-compatible manufacturing process we established. The cohort of the CD patients include patients CD#59 and CD#60 who carry the G176E and A305E mutations in the *ASPA* gene, patient CD#68 who carries the E285A mutation in the *ASPA* gene, patient CD#92 who has one nucleotide insertion in exon 2 of the *ASPA* gene, CD#00 who has a H244R mutation in the *ASPA* gene, and CD#01 who has a deletion and two point mutations in the *ASPA* gene (Figure 1A). Among the *ASPA* mutations, A305E is the most common mutation (60%) in non-Jewish CD patients,<sup>[13]</sup> while E285A is the predominant mutation (accounting for over 82% of mutations) among the Ashkenazi Jewish population.<sup>[14]</sup> The CD patient-derived fibroblast cells were reprogrammed via nucleofection to generate iPSCs using episomal vectors encoding the reprogramming factors human OCT4, SOX2, KLF4, L-MYC, and LIN28. At least three iPSC colonies with typical human embryonic stem cell (ESC) morphology and marker expression (Figure S1A, Supporting Information) were selected and expanded for each patient fibroblast line.

For each patient, one line of iPSCs that express the pluripotency genes and human ESC surface markers (Figure S1A, Supporting Information) and exhibit normal karyotype (Figure S2A, Supporting Information) was selected for in-process testing. All six lines were negative for microbial and mycoplasma contamination (Table S1, Supporting Information). Short tandem repeat (STR) analysis confirmed that all CD iPSC clones exhibited the same STR pattern as their parental fibroblast cells on all loci tested (Table S2, Supporting Information). For each CD patient iPSC line, flow cytometry analysis showed that more than 90% cells express the pluripotency marker OCT4 and the human ESC surface marker SSEA4 (Table S3, Supporting Information).

Reverse transcription polymerase chain reaction (RT-PCR) analysis was performed to confirm the activation of the endogenous pluripotency genes and detect any residual exogenous reprogramming factors in each CD iPSC line. The activation of the endogenous OCT4, SOX2, and NANOG gene expression was detected in iPSCs derived from each CD patient fibroblast line, whereas the exogenous reprogramming factors, OCT4, KLF4,

---

Prof. S. A. Goldman  
Center for Translational Neuromedicine  
Faculty of Health and Medical Sciences  
University of Copenhagen  
Copenhagen DK-2200, Denmark

Prof. R. Matalon  
Department of Pediatrics  
the University of Texas Medical Branch at Galveston  
301 University Blvd, Galveston, TX 77555-0359, USA

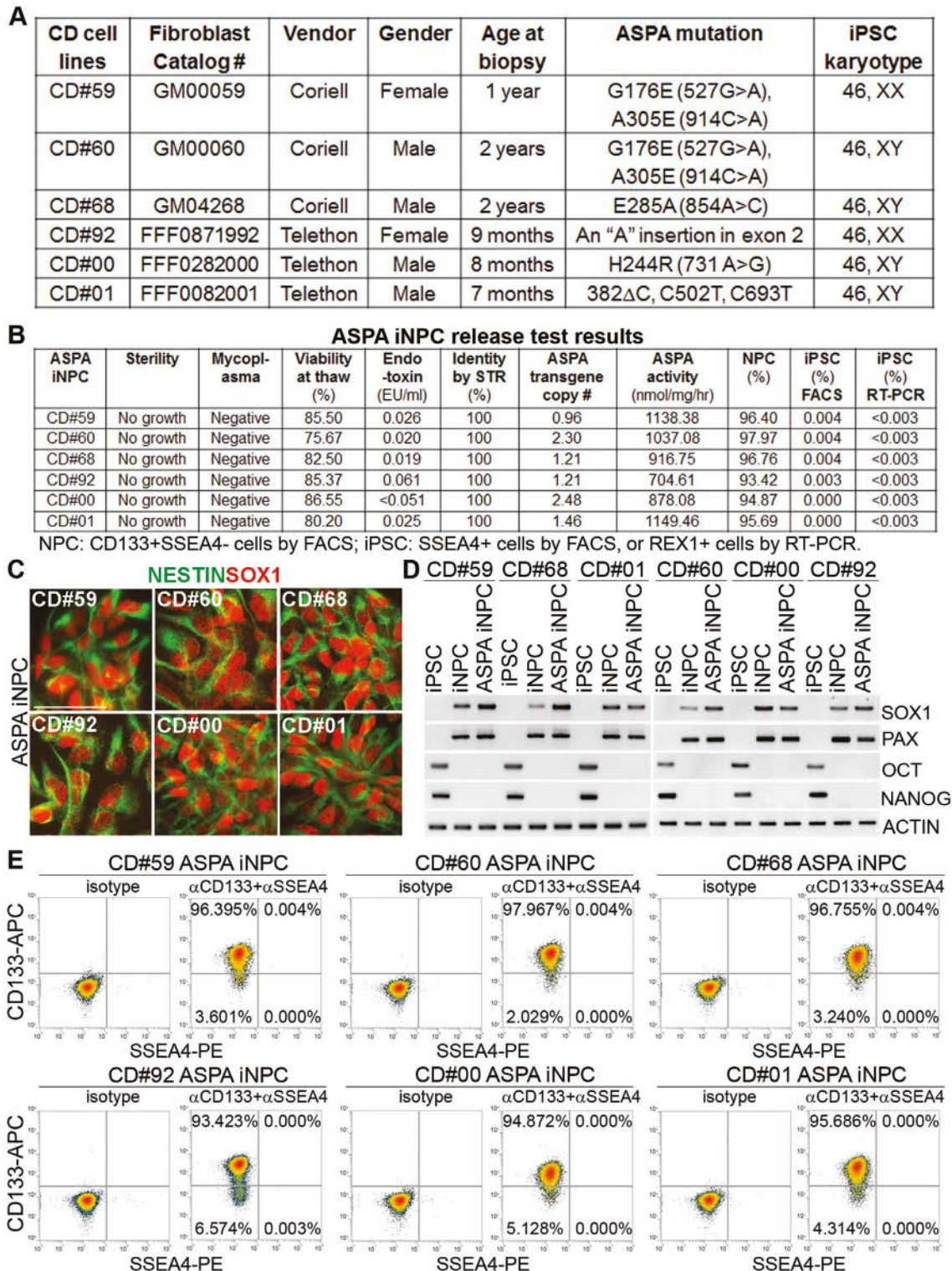


**Figure 1.** Characterization of the ASPA iNPCs. A) iPSC lines used in the study. B) The ASPA iNPC release test results. The ASPA activity was expressed as the increase of aspartic acid in nmol per mg cell lysates per hour at 37 °C. %NPC was determined as the percent of CD133<sup>+</sup>SSEA4<sup>-</sup> cells in ASPA iNPCs by FACS. % residual iPSCs was determined as the percent of SSEA4<sup>+</sup> cells by FACS or the percent of REX1<sup>+</sup> cells by RT-qPCR. C) Immunostaining of ASPA iNPCs for the NPC markers NESTIN and SOX1. Scale bar: 50  $\mu$ m. D) RT-PCR analysis of ASPA iNPCs for the expression of the NPC markers SOX1 and PAX6 and lack of expression of the pluripotency factors OCT4 and NANOG. ACTIN was included as a loading control. E) Flow cytometry analysis to determine the percentage of CD133<sup>+</sup>SSEA4<sup>-</sup> NPC population and the residual SSEA4<sup>+</sup> iPSC population in ASPA iNPCs. Isotype IgG was included as the negative control.



MYC, and LIN28, were not detectable in any iPSCs by passage 6 (Figure S1B,C, Supporting Information). Sanger sequencing confirmed that each CD patient-derived iPSC line harbored the same ASPA mutation as the corresponding CD patient (Figure S2B, Supporting Information).

After in-process testing, the CD iPSCs that met the specifications were differentiated into CD iNPCs. The CD iNPCs lines were expanded up to passage 6. At this stage, all CD iNPC lines were tested for sterility and mycoplasma and confirmed to be free of contamination.

## 2.2. Generating ASPA iNPCs by Lentiviral Transduction of a Functional ASPA Gene into CD iNPCs

Because CD is caused by *ASPA* gene mutations, which lead to deficient *ASPA* enzymatic activity, a functional *ASPA* gene was introduced into CD iNPCs by transducing CD iNPCs with a lentiviral vector. The lentiviral vector consisting of the sequence of a functional human *ASPA* gene (R132G ASPA) under the control of the constitutive human *EF1 $\alpha$*  promoter was called LV-*EF1 $\alpha$* -hASPA. The R132G mutation created outside of the catalytic center for the purpose of tracking did not disrupt the *ASPA* enzymatic activity, but increased *ASPA* activity mildly (Figure S2C, Supporting Information). The LV-*EF1 $\alpha$* -hASPA was used for genetic modification of CD iNPCs. The resultant cellular product was termed ASPA iNPCs.

The ASPA iNPCs were sampled during manufacturing (in-process, Tables S1–S3, Supporting Information) and at final product stage (Figure 1B; and Table S4, Supporting Information) for characterization. According to the established procedures, the ASPA iNPCs were characterized for sterility, mycoplasma, viability at thaw, endotoxin, STR profiling, *ASPA* transgene copy#, *ASPA* activity, %NPC (CD133<sup>+</sup>SSEA4<sup>-</sup> cells), and % residual iPSC (SSEA4<sup>+</sup> cells by FACS and REX1<sup>+</sup> cells by RT-qPCR). The copy number of the virally transduced *ASPA* transgene in the ASPA iNPCs was determined by TaqMan real time PCR following a published protocol.<sup>[15]</sup> The copy number of the transgene is less than five in all 6 ASPA iNPC lines. The *ASPA* activity was measured using a coupled enzymatic reaction<sup>[16]</sup> and robust *ASPA* activity was detected in each ASPA iNPC line (Figure 1B).

We also characterized ASPA iNPCs to confirm that they expressed typical NPC markers PAX6, SOX1, NESTIN, and CD133. We showed that all 6 lines of ASPA iNPC lines expressed typical NPC markers, including NESTIN, SOX1, and PAX6, as revealed by immunostaining (for NESTIN and SOX1) and RT-PCR (for SOX1 and PAX6) analyses (Figure 1C,D), whereas no expression of the pluripotency factors OCT4 and NANOG was detected in ASPA iNPCs (Figure 1D). FACS analysis was performed to determine the percentage of CD133<sup>+</sup>SSEA4<sup>-</sup> NPC population, which ranged from 93.42% to 97.97% in six lines of ASPA iNPCs, and confirmed the lack of residual iPSCs in ASPA iNPCs (0–0.004% by SSEA4 FACS and <0.003% by REX1 RT-qPCR) (Figure 1E). ASPA iNPCs derived from 6 CD patients all met the release testing criteria. In summary, we have successfully established GMP-compatible manufacturing processes and generated genetically modified ASPA iNPCs from CD patients using these processes.

## 2.3. Generation of Immunodeficient CD (Nur7) Mice for ASPA iNPC Transplantation

The *Aspa*<sup>nur7/nur7</sup> mouse contains a nonsense mutation (Q193X) in the *ASPA* gene.<sup>[17]</sup> Because *Aspa*<sup>nur7/nur7</sup> mice exhibit key pathological phenotypes resembling those of CD patients, including loss of *ASPA* enzymatic activity, elevated NAA levels, and extensive spongy degeneration in various brain regions,<sup>[17]</sup> it is considered a relevant animal model for CD. Therefore, the *Aspa*<sup>nur7/nur7</sup> mouse provides an excellent platform for testing the therapeutic effects of the ASPA iNPCs.

Because we needed to transplant human cells into CD (Nur7) mice, we generated an immunodeficient *ASPA*<sup>nur7/nur7</sup> mouse model by breeding the *Aspa*<sup>nur7/nur7</sup> mice with immunodeficient *Rag2*<sup>-/-</sup> mice, which lack mature B and T lymphocytes.<sup>[18]</sup> The resultant *Aspa*<sup>nur7/nur7</sup>/*Rag2*<sup>-/-</sup> mice were termed “CD (Nur7) mice” for short. These mice exhibit a range of pathological features of CD (see results below) and were used for transplantation studies to evaluate the efficacy of the ASPA iNPC cellular product. All CD (Nur7) mice used for transplantation were verified to carry homozygous *nur7* and *Rag2* genetic mutations by genotyping. Postnatal day (PND) 1–4 pups of both sexes were used for transplantation.

## 2.4. The Distribution and Cell Fate of ASPA iNPCs in the Transplanted CD (Nur7) Mouse Brains

Three lines of ASPA iNPCs derived from three different CD patients, including CD#59, CD#60, and CD#68, were injected into CD (Nur7) mouse brains individually. The injection was performed bilaterally into six sites. The injection sites include the corpus callosum, the subcortical white matter, and the brain stem (Figure 2A). The ASPA iNPC-transplanted mice were evaluated at organismal, histological, and biochemical levels. The wild type (WT, *ASPA*<sup>+/+</sup> / *Rag2*<sup>-/-</sup>) and/or heterozygous (Het, *ASPA*<sup>nur7/+</sup> / *Rag2*<sup>-/-</sup>) mice were included as the positive control, while the non-transplanted CD (Nur7) mice (*ASPA*<sup>nur7/nur7</sup> / *Rag2*<sup>-/-</sup>) were included as the negative control for the preclinical efficacy studies. In addition, the medium for ASPA iNPCs was injected into CD (Nur7) mouse brains using the same coordinates and procedure as for cell transplantation as a sham control.

First, we determined the survival, distribution, and cell fate of the ASPA iNPCs in brains of the transplanted mice by immunohistochemical staining for human nuclear antigen (hNu) and markers of various neural lineage cells. 3 months after transplantation, brains of the transplanted mice were harvested. The survival of the transplanted ASPA iNPCs was determined by immunostaining the transplanted mouse brains for hNu. We were able to detect the signal of hNu in multiple regions of the transplanted brain, including the corpus callosum, the subcortical region, and the brain stem region (Figure S3A, Supporting Information). The ASPA iNPCs were distributed around the injection sites, without extensive migration, in the transplanted CD (Nur7) mouse brain (Figure 2B).

Double staining of the transplanted brains with antibodies for hNu and the NPC marker PAX6 revealed that a small portion of the ASPA iNPCs was maintained as NPCs (Figure 2C,D; and Figure S3A,B, Supporting Information). Double staining

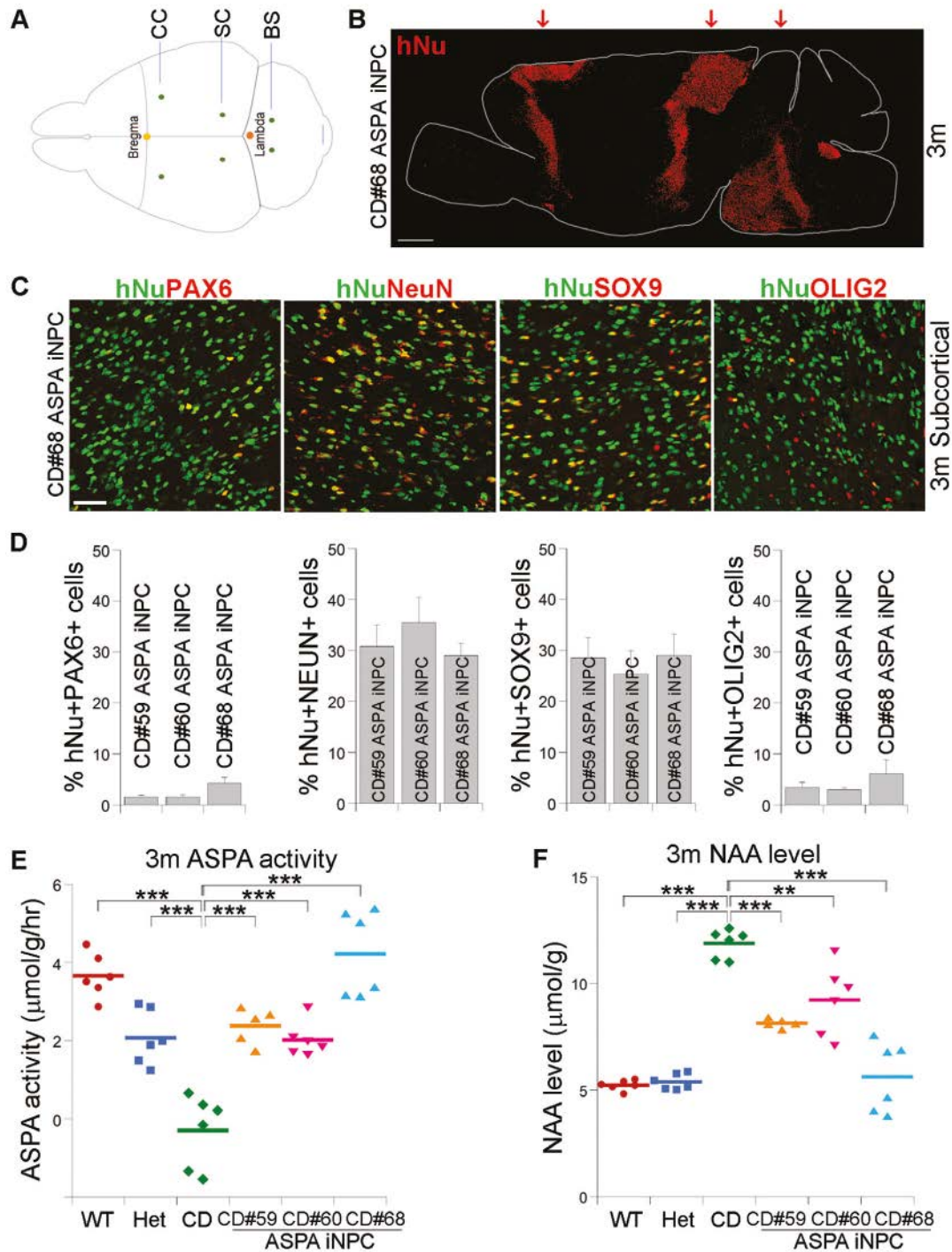


**Figure 2.** Elevated ASPA activity and reduced NAA level in ASPA iNPC-transplanted CD (Nur7) mouse brains. A) Illustration of the injection sites in mouse brains. The bilateral injection sites were indicated in green dots. B) The ASPA iNPCs were distributed around the injection sites in the transplanted CD (Nur7) mouse brains 3 months after transplantation. The dot map of the human nuclear antigen (hNu) staining is shown. The injection sites were indicated by arrows. Scale bar: 1 mm. C) The ASPA iNPCs gave rise to neurons, astrocytes, and oligodendroglial lineage cells in the transplanted mouse brains. 3 months after transplantation, the ASPA iNPC-transplanted brains were immunostained for hNu and the NPC marker PAX6, the neuronal marker NeuN, the astrocyte marker SOX9, and the oligodendroglial lineage marker OLIG2, respectively. The images from the subcortical white matter was shown. Scale bar: 50 µm. D) The percentage of hNu<sup>+</sup> and the neural lineage marker<sup>+</sup> cells in the transplanted brains. *n* = 9 fields from 3 mice for each group. E, F) Elevated ASPA activity E) and reduced NAA level F) in ASPA iNPC-transplanted CD (Nur7) mouse brains 3 months after transplantation. The NAA level was measured using NMR. The ASPA activity was measured by NMR and expressed as reduced NAA level per gram of brain tissue within an hour (h) ( $\mu\text{mol g}^{-1} \text{h}^{-1}$ ). Each dot represents the result from an individual mouse. *n* = 6 mice for the WT, Het, and CD (Nur7) mice, 5 for the CD#59 ASPA iNPC, and 6 for the CD#60 ASPA iNPC and CD#68 ASPA iNPC-transplanted mice, respectively. Error bars are SE of the mean. \*\*\**p* < 0.001 by one-way ANOVA followed by Dunnett's multiple comparisons test for panels (E, F).



for hNu and the neuronal marker NeuN, the astrocyte marker SOX9, and the oligodendroglial lineage marker OLIG2, respectively, revealed that the ASPA iNPCs could give rise to neurons, astrocytes, and oligodendroglial lineage cells in the transplanted brains (Figure 2C,D; and Figure S3A,B, Supporting Information). There was no obvious difference in the fate of the transplanted cells in the regions where they were located, including the corpus callosum, the subcortical, and the brain stem white matters (Figure 2C,D; and Figure S3A,B, Supporting Information), presumably because they were all white matter tracks.

### 2.5. Increased ASPA Activity and Reduced NAA Levels in ASPA iNPC-Transplanted CD (Nur7) Mouse Brains

Because the deficiency in ASPA enzymatic activity is the underlying cause of disease phenotypes in both CD patients and animal models, we sought to determine the ASPA enzymatic activity in ASPA iNPC-transplanted CD (Nur7) mouse brains. 3 months after transplantation, brains of the ASPA iNPC-transplanted mouse brains were evaluated for ASPA enzymatic activity and NAA levels. Potent ASPA enzymatic activity was detected in brains of all ASPA iNPC-transplanted mice, compared to that in control CD (Nur7) mouse brains without transplantation (Figure 2E). In contrast, the medium-treated CD (Nur7) mice exhibited deficient ASPA activity, similar to the control CD (Nur7) mice (Figure S4A, Supporting Information). Further comparison revealed that the ASPA activity in the ASPA iNPC-transplanted CD (Nur7) mouse brains is similar to or higher than the ASPA activity in the Het mice. Of interest, both Het human subjects and Het CD (Nur7) mice are phenotypically normal,<sup>[17]</sup> although the ASPA activity in the Het mouse brains is about 50–60% of that in the WT brains (Figure 2E). It has been shown that ASPA deficiency leads to elevated NAA level in brains of both CD patients and mouse models.<sup>[1,17,19]</sup> Consistent with elevated ASPA enzymatic activity, we detected reduced NAA level in the ASPA iNPC-transplanted CD (Nur7) mouse brains, compared to that in control CD (Nur7) mouse brains (Figure 2F). In contrast, the NAA level remained to be elevated in medium-treated CD (Nur7) mouse brains (Figure S4B, Supporting Information). These results together indicate that transplantation with the ASPA iNPCs was able to rescue the deficiency of ASPA enzymatic activity and reduce NAA level, both of which are major defects in CD patients and mouse models, and that the therapeutic effect was resulted from the cell products instead of the procedure by itself because medium control exhibited no effect on either ASPA activity or NAA level.

### 2.6. Rescue of Spongy Degeneration in ASPA iNPC-Transplanted CD (Nur7) Mouse Brains

Extensive spongy degeneration is a key pathological feature of CD patients and mouse models, which is revealed by vacuolation in various brain regions.<sup>[1,17,19]</sup> Indeed, we observed extensive vacuolation in brains of the CD (Nur7) mice, compared to brains of the Het mice, which have intact brain parenchyma (Figure 3A–C). In contrast, hematoxylin and eosin (H&E) staining revealed substantially reduced vacuolation in various brain regions of the ASPA iNPC-transplanted CD (Nur7) mice, including the subcor-

tical white matter, the brain stem and the cerebellum (Figure 3A–C), but not in medium-treated CD (Nur7) mice (Figure S4C,D).

The extent of rescue in the cerebellum region was not as extensive as the subcortical white matter and the brain stem regions, presumably because the cerebellum is too far away from the injection sites. The ASPA iNPCs derived from three different CD patients all led to substantial rescue, in a comparable manner (Figure 3A–C). These results indicate that transplantation with ASPA iNPCs was able to rescue the spongy degeneration phenotype in CD (Nur7) mouse brains, supporting the therapeutic potential of ASPA iNPCs for their ability to ameliorate the pathological phenotypes of CD.

### 2.7. Improved Myelination in ASPA iNPC-Transplanted CD (Nur7) Mouse Brains

It has been suggested that vacuolation results from myelin destruction in brains of CD (Nur7) mice.<sup>[17]</sup> Consistent with the extensive vacuolation detected in brains of the CD (Nur7) mice, we observed substantially reduced number of normal myelin sheaths in brains of the CD (Nur7) mice, compared to that of the Het mice, as revealed by electron microscopy (EM) analysis (Figure 4A,B) and myelin basic protein (MBP) staining (Figure S5, Supporting Information). G ratio, the ratio of the inner diameter to the outer diameter of myelin sheaths, was also altered in CD (Nur7) mouse brains. Increased G ratio was detected in brains of the CD (Nur7) mice, compared to that in the heterozygous mice (Figure 4A,C). Transplantation with ASPA iNPCs led to substantially improved myelination in CD (Nur7) mouse brains. The number of normal myelin sheaths in the ASPA iNPC-transplanted CD brains was much higher than that in the control CD brains, reaching the level in the Het mouse brains (Figure 4A,B). Moreover, the G ratio of myelin sheaths in the transplanted brains resembled that in the Het mouse brains, both of which were much lower than that in that in the control CD brains (Figure 4A,C), indicating that the myelin sheaths in the transplanted brains are thicker than those in the untreated control CD brains. The reduced myelin sheaths and disordered nerve tracts could also be found in CD (Nur7) mouse brains by immunostaining for MBP, a marker of myelination (Figure S5, Supporting Information). Transplantation with the ASPA iNPCs improved myelination as revealed by enhanced MBP staining and better-organized nerve tracts (Figure S5, Supporting Information).

### 2.8. Rescue of Gross Motor and Neuromuscular Function in ASPA iNPC-Transplanted CD (Nur7) Mice

Defect in motor performance is typical of CD patients and animal models.<sup>[1,17,19]</sup> To determine if transplantation with the ASPA iNPCs could rescue the defective motor performance in CD (Nur7) mice, we tested the ASPA iNPC-transplanted CD (Nur7) mice in two motor skill paradigms at 3 months after transplantation. First, the transplanted mice were tested using an accelerating rotarod, a device that is designed for testing motor coordination and balance.<sup>[20]</sup> Transplantation with ASPA iNPCs improved rotarod performance substantially in CD (Nur7) mice transplanted with any of the three ASPA iNPC lines, compared to the control CD (Nur7) mice (Figure 4D). A grip strength test was

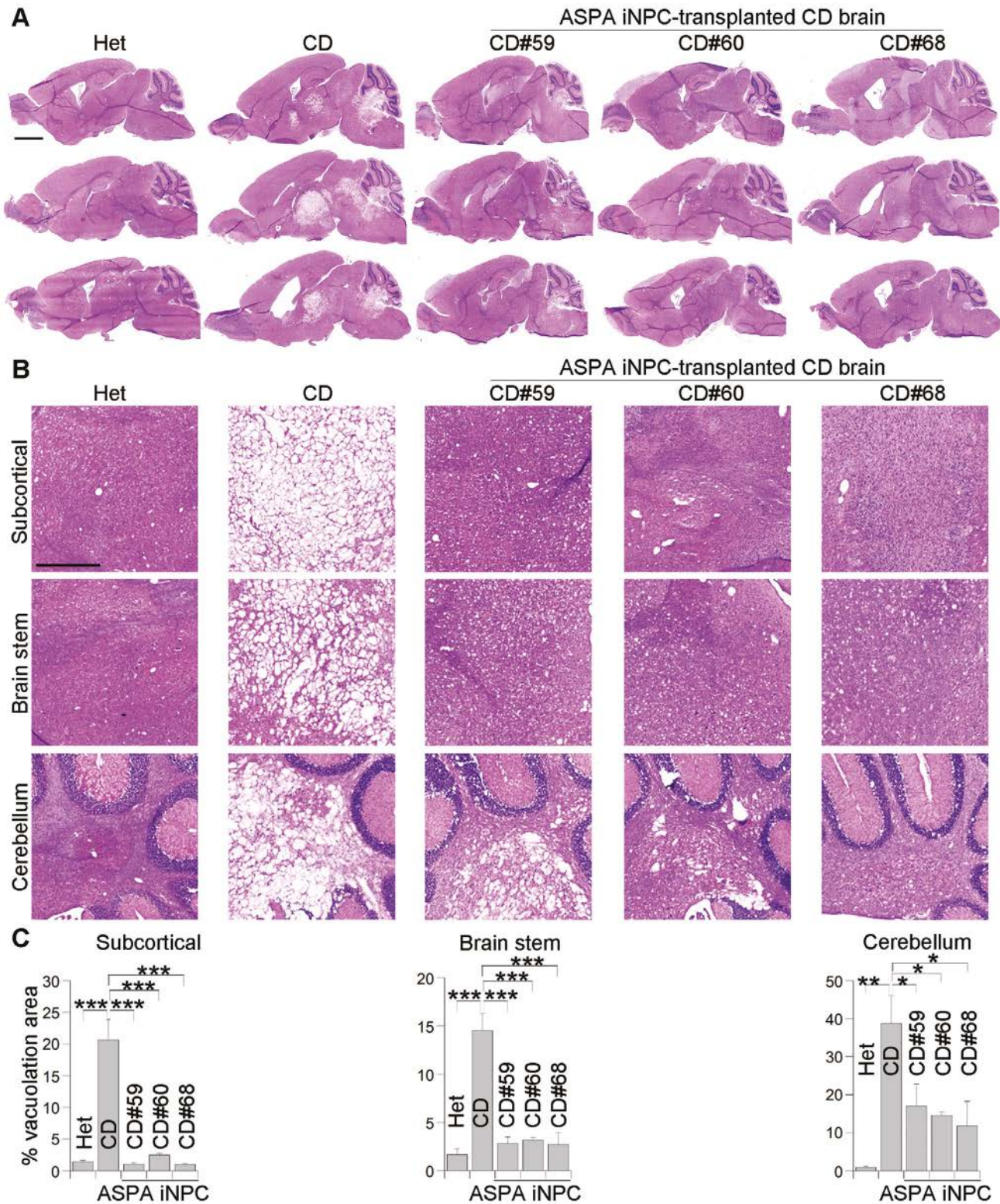


**Figure 3.** Reduced vacuolation in the ASPAs iNPC-transplanted CD (Nur7) mouse brains. A) Reduced vacuolation in brains of the ASPAs iNPC-transplanted CD (Nur7) mice 3 months after transplantation as revealed by H&E staining. Three whole brain sagittal sections of one mouse from each group are shown. The heterozygous (Het) mice were included as the positive control and the homozygous CD (Nur7) mice as the negative control. Scale bar: 2000  $\mu$ m. B) Enlarged H&E images of the subcortical white matter, the brain stem and the cerebellum are shown. Scale bar: 500  $\mu$ m. C) Quantification of the vacuolation area in the subcortical, the brain stem, and the cerebellum white matter.  $n = 3$  mice per group. Error bars are SE of the mean. \* $p < 0.05$ , \*\* $p < 0.01$ , and \*\*\* $p < 0.001$  by one-way ANOVA followed by Dunnett's multiple comparisons test.



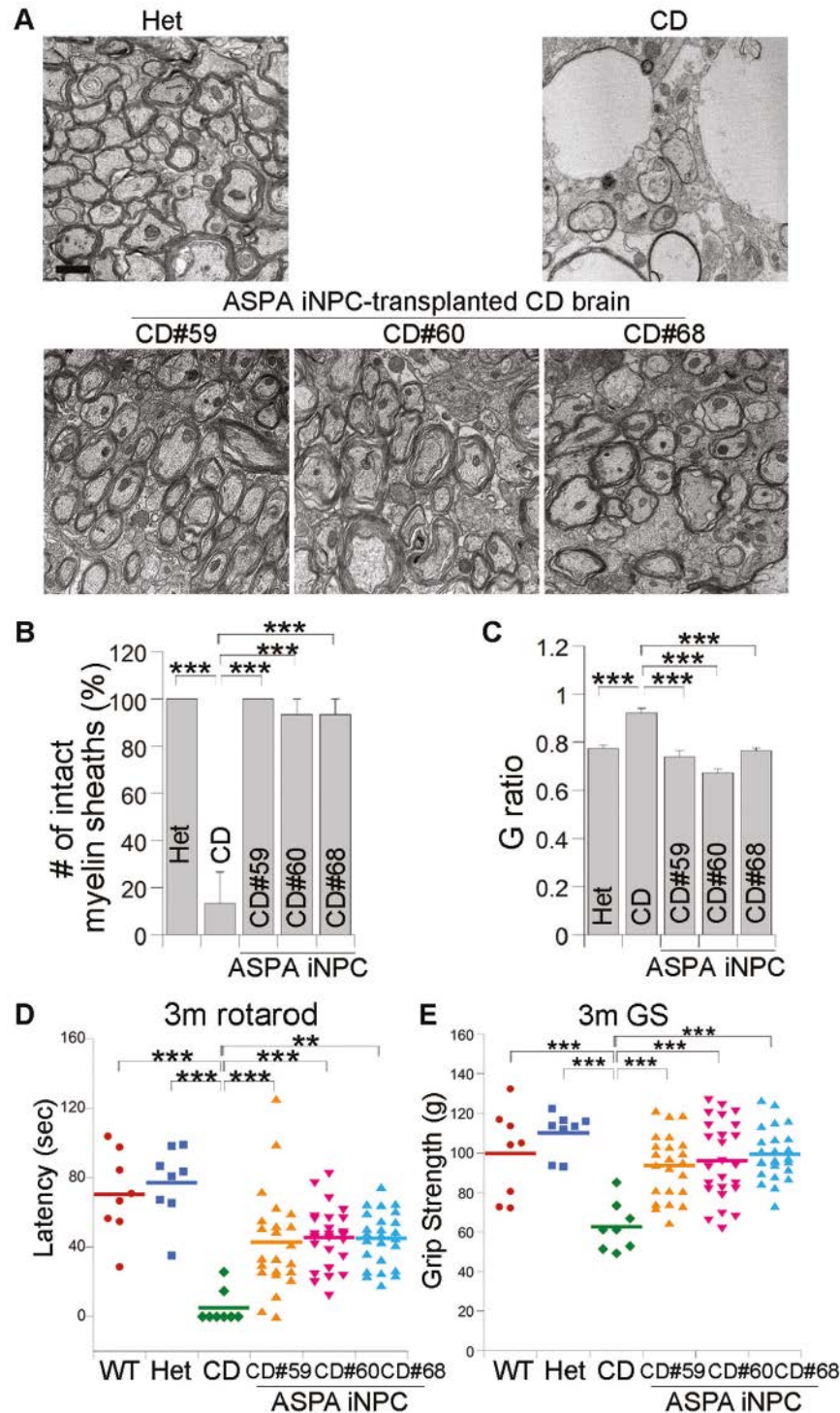


**Figure 4.** Improved myelination and motor function in ASPA iNPC-transplanted CD (Nur7) mice. **A)** Improved myelination in the ASPA iNPC-transplanted CD (Nur7) mouse brains 3 months after transplantation. Improved myelination was shown by electron microscope and revealed by increased number of intact myelin sheaths and enhanced thickness of myelin sheaths in brains of the transplanted mice, compared to control CD (Nur7) mice. The subcortical white matter was processed and analyzed. Scale bar: 1  $\mu$ m. **B,C)** Quantification showing increased number of intact myelin sheaths **B)** and enhanced thickness of myelin sheaths as revealed by reduced G ratio **C)** in brains of the ASPA iNPC-transplanted mice CD (Nur7) mice, compared to that in control CD (Nur7) mice.  $n = 15$  myelin sheaths from one mouse brain for each group. 3 transplanted brains (one brain for each line) were analyzed. Error bars are SE of the mean. **D,E)** Improved motor function in ASPA iNPC-transplanted CD (Nur7) mice 3 months after transplantation revealed by rotarod **D)** and grip strength (GS, **E)** tests. Each dot represents the result from an individual mouse.  $n = 8$  mice for the WT, Het, and CD (Nur7) mice, 23, 25, and 25 for the CD#59 ASPA iNPC, CD#60 ASPA iNPC, and CD#68 ASPA iNPC-transplanted mice, respectively, for panels **(D,E)**.  $*p < 0.05$ ,  $**p < 0.01$ , and  $***p < 0.001$  by one-way ANOVA followed by Tukey's multiple comparisons test for panels **(B,C)** and by Dunnett's multiple comparisons test.

performed to evaluate the forepaw strength as an indication of neuromuscular function,<sup>[21]</sup> using a grip strength meter. Substantial enhancement of the grip strength was also detected in CD (Nur7) mice, compared to that in the control CD (Nur7) mice transplanted with any of the three lines of ASPA iNPCs (Figure 4E). In contrast, treatment with the medium control exhibited no effect on either the rotarod performance or the grip strength of the CD (Nur7) mice (Figure S4E, F, Supporting Information). These results indicate that the ASPA iNPCs can substantially improve motor functions in a mouse model of CD. These results together provide a proof-of-concept that the ASPA iNPCs have great therapeutic potential to ameliorate the pathological phenotypes of CD.

## 2.9. Sustained Rescue of Disease Phenotypes in ASPA iNPC-Transplanted CD (Nur7) Mice

The ASPA iNPCs were sustained in brains of the transplanted mice 6 months after transplantation and the cell fate was largely maintained (Figure S6A,B, Supporting Information), although there is a mild increase in the astrocyte (hNu<sup>+</sup>SOX9<sup>+</sup>) and the oligodendroglial (hNu<sup>+</sup>OLIG2<sup>+</sup>) populations, and a mild reduction in the NPC (hNu<sup>+</sup>PAX6<sup>+</sup>) and neuronal (hNu<sup>+</sup>NeuN<sup>+</sup>) populations from the transplanted cells 6 months post-transplantation, compared to 3 months post-transplantation (Figure S6C, Supporting Information).

To determine if transplantation with the ASPA iNPCs could lead to sustained ASPA activity, brains of the CD68 ASPA iNPC-transplanted CD (Nur7) mouse brains were evaluated for ASPA activity 6 months after transplantation. Substantially higher ASPA enzymatic activity was detected in brains of ASPA iNPC-transplanted CD (Nur7) mice, compared to that in control CD (Nur7) mice (Figure 5A). The ASPA activity in the ASPA iNPC-transplanted CD (Nur7) mouse brains is similar to or even slightly higher than the ASPA activity in the Het mice 6 months after transplantation (Figure 5A). Consistent with elevated ASPA enzymatic activity, we detected dramatically reduced NAA level in brains of ASPA iNPC-transplanted CD (Nur7) mice, compared to that in control CD (Nur7) mice (Figure 5B). These results together indicate that transplantation with ASPA iNPCs was able to rescue the deficiency of ASPA enzymatic activity and reduce NAA level in a sustainable manner.

To determine if ASPA iNPC transplantation could have long-term beneficial effect, we examined brains of the ASPA iNPC-transplanted CD (Nur7) mice for vacuolation. Substantially reduced vacuolation in various brain regions of the CD#68 ASPA iNPC-transplanted CD (Nur7) mice, including the subcortical white matter, the brain stem, and the cerebellum, was detected 6 months after transplantation (Figure 5C,D,E). These results indicate that transplantation with the ASPA iNPCs was able to rescue the spongy degeneration phenotype in CD (Nur7) mouse brains in a sustainable manner.

To determine if transplantation with the ASPA iNPCs could lead to sustained improvement of motor function in CD (Nur7) mice, we tested the ASPA iNPC-transplanted CD (Nur7) mice at 6 months after transplantation. The ASPA iNPCs improved rotarod performance in transplanted CD (Nur7) mice substantially 6 months after transplantation, compared to the control CD

(Nur7) mice (Figure 5F). Considerable enhancement of the grip strength was also detected in the ASPA iNPC-transplanted CD (Nur7) mice 6 months after transplantation, compared to the control CD (Nur7) mice (Figure 5G). This result indicates that the engrafted ASPA iNPCs can sustain improved motor functions in CD (Nur7) mice.

## 2.10. The ASPA iNPC-Transplanted Mice Exhibit Prolonged Survival

We monitored the ASPA iNPC-transplanted CD (Nur7) mice for up to 10 months to track their life span. The WT and Het mice were included as the positive control and the CD (Nur7) mice as the negative control. We observed substantially prolonged lifespan in the ASPA iNPC-transplanted mice, compared to the control CD (Nur7) mice (Figure 5H). While 45% of the control CD (Nur7) mice ( $n = 20$ ) died before 10 months, only one ASPA iNPC-transplanted CD (Nur7) mouse out of a total of 20 transplanted mice died before 10 months. Taken together, the results from the preclinical efficacy study provide a proof-of-concept that the ASPA iNPCs have great therapeutic potential to ameliorate the pathological phenotypes of CD in a robust and sustainable manner.

## 2.11. Preliminary Safety of the ASPA iNPCs in the Transplanted CD (Nur7) Mice

For a preliminary safety study, CD (Nur7) mice transplanted with the ASPA iNPCs were monitored monthly for up to 10 months, and no signs of tumor formation or other adverse effects were observed. At the end of 3 and 6 months, brains of the transplanted mice were harvested and analyzed. No tumor tissue was found in the transplanted brain sections. The lack of tumor formation in the ASPA iNPC-transplanted brains was confirmed by Ki67 staining. A low mitotic index, as revealed by the low percentage (1.35–4.32%) of hNu and Ki67 double positive (hNu<sup>+</sup>Ki67<sup>+</sup>) cells out of total hNu<sup>+</sup> cells, was detected in the ASPA iNPC-transplanted brains at both 3 and 6 months post-transplantation (Figure 5I–K; and Figure S6D, Supporting Information). Furthermore, although separate animal brains were observed at 3- and 6-months after transplantation, the percent of hNu<sup>+</sup>Ki67<sup>+</sup> cells out of total hNu<sup>+</sup> cells appeared not to increase but to actually decrease in the transplanted brains, from 4.32% (at 3 months) to 2.20% (at 6 months) in CD#68 ASPA iNPC-transplanted brains (Figure 5K). These results demonstrate preliminary safety of ASPA iNPCs in transplanted brains.

## 2.12. The ASPA iOPCs Exhibit Widespread Distribution in Transplanted CD (Nur7) Mice

As an alternative to introducing a functional ASPA gene into CD iNPCs through lentiviral transduction, we also knocked in a WT ASPA gene into the AAVS1 safe harbor site in CD68 iPSCs through TALEN-mediated gene editing (Figure 6A). The WT ASPA gene was linked to a truncated CD19 (CD19t) surface marker through T2A. The gene-edited iPSCs were selected by flow cytometry using a CD19-specific antibody. Single cell-derived colonies were picked and expanded. One of the colonies,

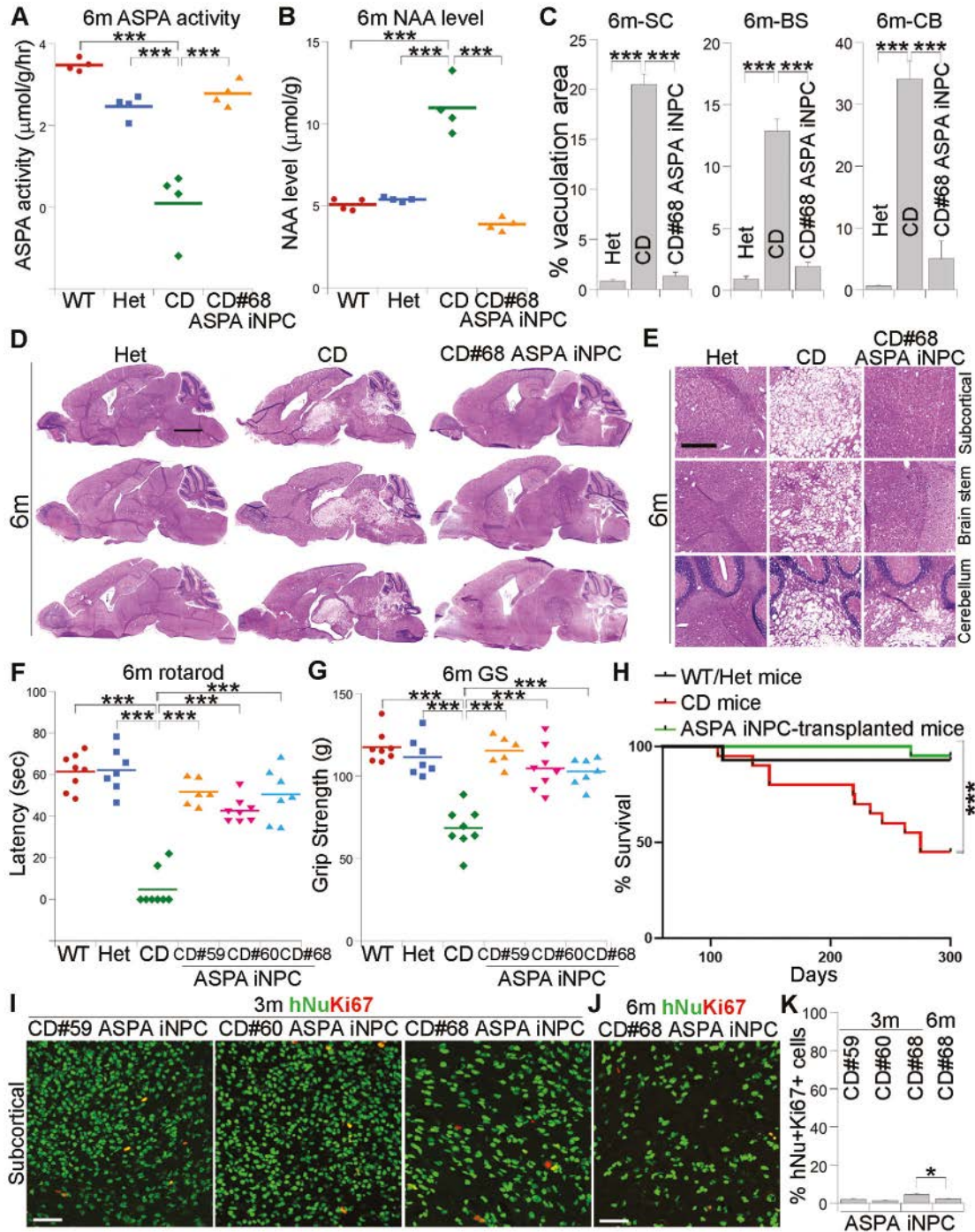


**Figure 5.** Sustained efficacy of ASPA iNPCs in transplanted CD (Nur7) mice 6 months after transplantation. A,B) Elevated ASPA activity A) and reduced NAA level B) in ASPA iNPC-transplanted CD (Nur7) mouse brains 6 months after transplantation. The ASPA activity and NAA level was measured using NMR as described earlier.  $n = 4$  mice for each group. C–E) Reduced vacuolation in brains of ASPA iNPC-transplanted CD (Nur7) mouse brains as revealed by H&E staining. Quantification is shown in panel (C), and enlarged H&E images are shown in panel (E).  $n = 3$  mice for each group. Scale bar: 2000  $\mu\text{m}$  for D and 500  $\mu\text{m}$  for (E). F,G) Improved motor function in ASPA iNPC-transplanted CD (Nur7) mice 6 months after transplantation, as revealed by rotarod F) and grip strength (GS, G) tests.  $n = 8$  mice for WT, Het and CD (Nur7) mice, respectively, 6 for CD#59 ASPA iNPC, 8 for CD#60 ASPA iNPC, and 7 for CD#68 ASPA iNPC-transplanted mice. H) Life span of ASPA iNPC-transplanted CD (Nur7) mice. The survival of the transplanted mice was monitored over 10 months. The CD (Nur7) mice were included as the negative control and the WT/Het mice as the positive control.  $n = 20$  for CD, 14 for WT/Het, and 20 for the transplanted mice. I,J) Low mitotic index in ASPA iNPC-transplanted CD (Nur7) mouse brains as revealed by hNu and Ki67 costaining 3 I) or 6 months J) after transplantation. The images from the subcortical white matter was shown Scale bar: 50  $\mu\text{m}$ . K) The percentage of the hNu<sup>+</sup>Ki67<sup>+</sup> cells out of total hNu<sup>+</sup> cells in the transplanted brains.  $n = 9$  fields from 3 mice for each group. Error bars are SE of the mean. \*\*\* $p < 0.001$  by one-way ANOVA followed by Dunnett's multiple comparisons test for panels (A–C,F,G). \*\*\* $p < 0.001$  by Log-rank test between CD (Nur7) mice and ASPA iNPC-transplanted mice for panel (H). \* $p < 0.05$  by one-way ANOVA followed by Dunnett's multiple comparisons test for panel (K).



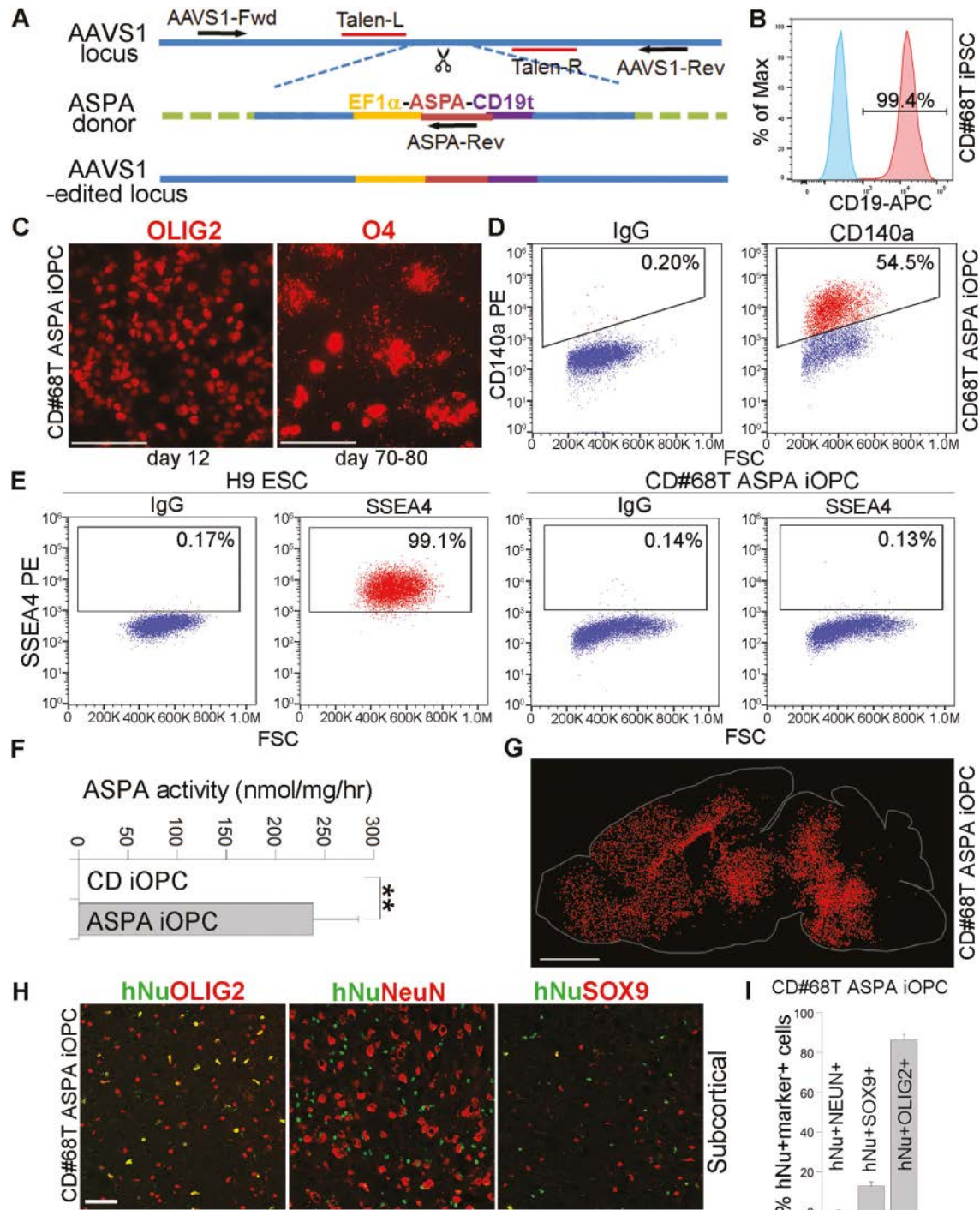


**Figure 6.** Characterization of ASPA iOPC. A) Schematic for introducing the WT ASPA gene into the AAVS1 locus in CD iPSCs by TALEN-mediated gene editing. B) Flow cytometry analysis of the CD#68T-13 ASPA iPSCs using CD19-specific antibody. The isotype IgG was included as the negative control (blue). The ASPA-T2A-CD19t-positive cells were shown in red. C) Immunostaining of the CD#68T-13 ASPA iOPCs for the oligodendroglial lineage markers OLIG2 and O4. D) Flow cytometry analysis of the ASPA iOPCs using CD140a-specific antibody. The isotype IgG was included as the negative control. E) Lack of residual SSEA4-positive iPSCs in ASPA iOPCs as revealed by flow cytometry. The isotype IgG was included as the negative control, which showed similar SSEA4<sup>+</sup> population to that of SSEA4 antibody-based flow. F) The ASPA iOPCs displayed potent ASPA enzymatic activity, compared to the control CD iOPCs.  $n = 3$  replicates.  $**p < 0.01$  by Student's  $t$ -test (two tailed). G) Dot map shows widespread distribution of the transplanted ASPA iOPCs in CD (Nur7) mouse brains by immunostaining for hNu 3 months after transplantation. H) Costaining of the transplanted CD (Nur7) mouse brains for human nuclear antigen hNu and the oligodendroglial lineage marker OLIG2, the neuronal marker NeuN, or the astrocyte marker SOX9, respectively. The images from the subcortical white matter were shown. I) The percentage of the hNu<sup>+</sup>NeuN<sup>+</sup>, hNu<sup>+</sup>SOX9<sup>+</sup>, and hNu<sup>+</sup>OLIG2<sup>+</sup> population in the ASPA iOPC-transplanted (Nur7) mouse brains.  $n = 9$  fields from 3 mice for each group. Scale bar: 100  $\mu$ m for (C), 2000  $\mu$ m for (G), and 50  $\mu$ m for (H). Error bars are SE of the mean for panels (F,I).

CD68T-13 ASPA iPSCs, was chosen for further analysis based on colony morphology. Flow cytometry analysis using CD19-specific antibody confirmed that the CD68T-13 ASPA iPSC colony contained more than 99% ASPA-CD19t-positive cells (Figure 6B), confirming successful knock-in. The CD68T-13 ASPA iPSCs exhibited normal karyotype (Figure S7A, Supporting Information) and lacked off-target mutation as revealed by whole genome sequencing (Table S5, Supporting Information).

Next we differentiated the CD68T-13 ASPA iPSCs into iOPCs following a published protocol.<sup>[10c,d]</sup> The ASPA iPSC were first differentiated into OLIG2<sup>+</sup> pre-OPCs, followed by induction into O4<sup>+</sup> OPCs (Figure 6C). These ASPA iPSC-derived OPCs were termed ASPA iOPCs. Flow cytometry analysis revealed enrichment of CD140a (PDGF $\alpha$ R)<sup>+</sup> OPCs (54.5%) in the differentiated cell population<sup>[22]</sup> (Figure 6D). In contrast, the CD68T ASPA iOPCs contained no detectable SSEA4<sup>+</sup> residual pluripotent stem cells (0.13% detected by SSEA4 antibody minus 0.14% by IgG control) (Figure 6E). A pure population of ASPA iOPCs could be obtained by CD140a-directed magnetic-activated cell sorting. The ASPA iOPCs exhibited potent ASPA enzymatic activity, compared to control CD68 iOPCs without ASPA knock-in (Figure 6F).

The ASPA iOPCs were then transplanted into brains of CD (Nur7) mice for efficacy evaluation using the same procedure as used for ASPA iNPC transplantation (Figure 2A). The distribution and cell fate of the engrafted ASPA iOPCs were analyzed 3 months after transplantation. In contrast to the ASPA iNPCs, the ASPA iOPCs showed widespread distribution throughout the brain as evidenced by immunostaining with hNu at 3 months after transplantation (Figure 6G). The ASPA iOPCs were detected in the forebrain, the subcortical, and the brain stem regions, although not the cerebellum, which may be too far away from the injection sites. Costaining for hNu and different cell lineage markers revealed that most donor cells were oligodendroglial lineage cells. The proportion of hNu<sup>+</sup>OLIG2<sup>+</sup> cell reached  $86.35 \pm 2.90\%$ . The remaining transplanted cells mostly became astrocytes ( $12.92 \pm 1.97\%$  hNu<sup>+</sup>SOX9<sup>+</sup> cells). Only very few human cell-derived neurons were detected in the transplanted brain ( $0.33 \pm 0.33\%$  hNu<sup>+</sup>NeuN<sup>+</sup> cells) (Figure 6H,I; and Figure S7B,C, Supporting Information). These results indicate that the ASPA iOPCs could migrate and gave rise to oligodendroglial lineage cells in the transplanted brains.

### 2.13. The ASPA iOPCs Exhibit Robust Efficacy and Preliminary Safety in Transplanted CD (Nur7) Mice

To determine the efficacy of ASPA iOPCs, we transplanted ASPA iOPCs into CD (Nur7) mice and the transplanted mice were evaluated 3 months after transplantation. Biochemically, the ASPA iOPCs was able to reconstitute ASPA enzymatic activity and reduce NAA level in the transplanted CD (Nur7) mouse brains (Figure 7A,B). The spongy degeneration was also rescued substantially in brains of the ASPA iOPC-transplanted CD (Nur7) mice, compared to the control CD (Nur7) mice (Figure 7C–E). Transplantation with the ASPA iOPCs also improved myelination in CD (Nur7) mice brains as revealed by enhanced MBP staining (Figure S5, Supporting Information). Moreover, the motor function in the ASPA iOPC-transplanted CD (Nur7) mice was improved considerably, as revealed by increased latency on the ro-

tarod (Figure 7F) and enhanced grip strength (Figure 7G), compared to the control CD (Nur7) mice. These results indicate that ASPA iOPCs have the potential to ameliorate the pathological phenotypes of CD.

Importantly, no sign of tumor formation or other adverse effect was observed during 3 months after ASPA iOPC transplantation. Ki67 staining showed minimal number of hNu<sup>+</sup>Ki67<sup>+</sup> cells out of total hNu<sup>+</sup> cells in the ASPA iOPC-transplanted brains (Figure 7H; and Figure S7D, Supporting Information). These results together demonstrate robust preclinical efficacy and preliminary safety of the ASPA iOPC cell product for CD therapy development.

## 3. Discussion

CD is a devastating neurological disease that has neither a cure nor a standard treatment.<sup>[23]</sup> In this study, we established human iPSC-based cell therapeutic candidates for CD. To facilitate the transfer of the cell therapeutic candidates to the clinic, we first established GMP-compatible processes for human iPSC derivation, expansion, and differentiation. We then generated iPSCs from CD patient fibroblast cells and differentiated these iPSCs into iNPCs using the GMP-compatible processes we established. To reconstitute ASPA activity which is deficient in both CD patients and mouse models, we developed ASPA iNPCs by introducing a functional ASPA gene through lentiviral transduction. We transplanted the ASPA iNPCs into CD (Nur7) mouse brains and showed that these cells were able to improve the disease symptoms dramatically, as revealed by increased ASPA activity, decreased NAA levels, substantially reduced spongy degeneration in various brain regions, and rescued motor functions of the transplanted mice. The therapeutic effect is long-lasting, showing no diminishing effect by 6 months compared to 3 months post-transplantation. Moreover, the transplanted CD (Nur7) mice exhibited much prolonged survival.

As an alternative strategy to introducing a functional ASPA gene by lentiviral transduction at the iNPC stage, we introduced a WT ASPA gene together with a truncated CD19 (CD19t) into the AAVS1 safe harbor site in CD iPSCs through TALEN-mediated gene editing. The CD19t sequence has been used in a previous clinical trial and confirmed to be safe.<sup>[24]</sup> The CD19t tag provides a cell surface marker for in vivo tracking of transplanted cells in patient brains by flow cytometry and immunohistochemistry approaches and can induce cell elimination through antibody-dependent cellular cytotoxicity in case of adverse tumorigenic events.<sup>[24,25]</sup> We chose TALEN-based editing for introducing the WT ASPA gene into CD iPSCs to generate the ASPA iOPC cell product because of the low off-target activity associated with TALEN.<sup>[26]</sup> Indeed, our whole genome sequencing revealed no off-target effects in the top 99 potential off-target sites. The TALEN-edited ASPA iPSCs were differentiated into iOPCs using an established protocol.<sup>[10d,11]</sup> After being transplanted into CD (Nur7) mouse brains, these cells showed an ability to rescue the CD phenotype that is comparable to that of ASPA iNPCs. Moreover, the ASPA iOPCs had better migration and more than 80% transplanted ASPA iOPCs went to the oligodendroglial lineage. Importantly, no tumorigenesis or other adverse effect was observed in mice transplanted with either the ASPA iNPCs or the ASPA iOPCs. These results indicate that the ASPA iNPCs and



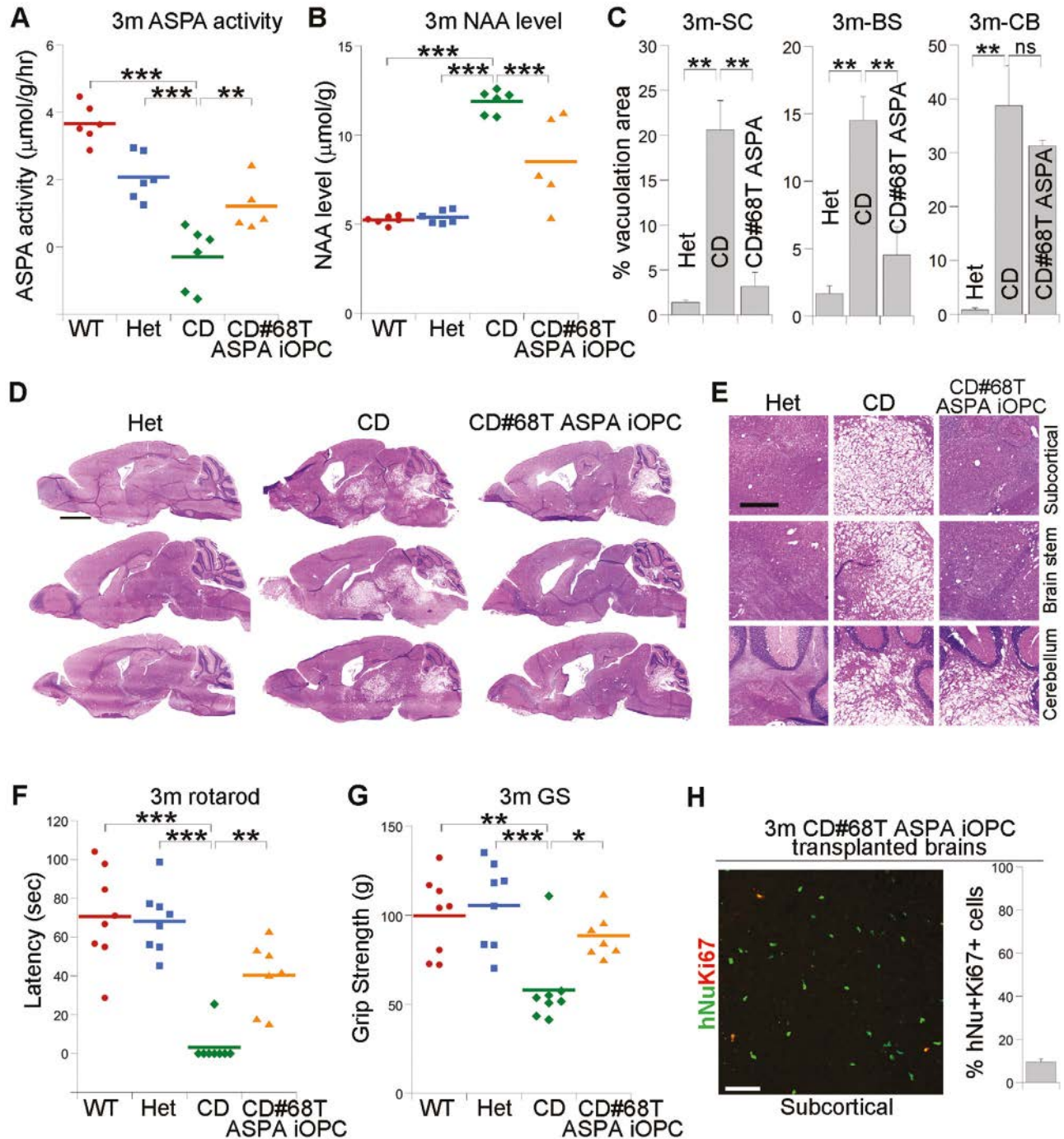


**Figure 7.** The ASPA iOPCs rescued multiple deficits in CD (Nur7) mice. A,B) Elevated ASPA activity A) and reduced NAA level B) in ASPA iOPC-transplanted CD (Nur7) mouse brains 3 months after transplantation measured by NMR. The ASPA activity was expressed as reduced NAA level per gram of brain tissue in an hour ( $\mu\text{mol g}^{-1} \text{h}^{-1}$ ). The same data for the WT, Het, and CD (Nur7) mice from Figure 2E,F as were included here as controls. Each dot represents the result from an individual mouse for panels (A,B).  $n = 6$  mice for WT, Het, and CD (Nur7) mice, respectively, and 5 for the CD#68T ASPA iOPC-transplanted mice. C–E) Reduced vacuolation in brains of ASPA iOPC-transplanted CD (Nur7) mouse brains as revealed by H&E staining. Quantification is shown in panel (C), and enlarged H&E images are shown in panel (E).  $n = 9$  fields from 3 mice for panel (C). Scale bar: 2000  $\mu\text{m}$  for (D) and 500  $\mu\text{m}$  for (E). F,G) Improved motor function in ASPA iOPC-transplanted CD (Nur7) mice 3 months after transplantation as revealed by rotarod (F) or grip strength (GS, G) test. Each dot represents the result from an individual mouse for panels (F,G).  $n = 8$  mice for WT, Het, and CD (Nur7) mice, respectively, and 7 for the CD#68T ASPA iOPC-transplanted mice. The same data for the WT mice from Figure 2C were included here as a control. H) The ASPA iOPCs showed low mitotic index in transplanted mouse brains as revealed by hNu and Ki67 costaining and the low percentage of the hNu+Ki67+ cells out of total hNu+ cells. The images from the subcortical white matter was shown.  $n = 9$  fields from 3 mice for panel (H). Error bars are SE of the mean. \* $p < 0.05$ , \*\* $p < 0.01$ , and \*\*\* $p < 0.001$  by one-way ANOVA followed by Dunnett’s multiple comparisons test for panels (A–C,F,G). ns stands for not statistically significant ( $p < 0.05$ ).

the ASPA iOPCs both have the potential to serve as cell therapy candidates for CD.

Great efforts have been directed toward therapeutic development for CD. While most other approaches resulted in limited functional recovery, gene therapy seems a promising clinical option for CD.<sup>[23b]</sup> When the WT human *ASPA* gene was delivered into brains of CD animal models by recombinant adeno-associated virus (rAAV), encouraging results were seen.<sup>[3,4,27]</sup> However, the early clinical trial using AAV to deliver the *ASPA* gene into CD patient brains was unable to reach the desired therapeutic efficacy, although the safety profile was good.<sup>[3]</sup> Recent studies showed that knockdown of the neuronal NAA-synthesizing enzyme *Nat8l* by antisense oligonucleotide or AAV-delivered shRNA to reduce NAA level improved disease phenotypes in *ASPA*<sup>nut7/nut7</sup> mice,<sup>[28]</sup> suggesting that targeting *Nat8l* could be a candidate approach to treat CD, although how to achieve sustained efficacy using this approach remains to be addressed.

Compared to direct gene therapy, the combined cell and gene therapy approach used in this study allowed extensive *in vitro* characterization of the genetically modified cells before applying these cells to *in vivo* study. The ASPA iNPCs were examined for transgene copy number and all six ASPA iNPC lines had less than five copies of the transgene. The ASPA iPSCs that underwent TALEN-mediated gene editing were subjected to whole genome sequencing to make sure there were no adverse off-target effects before differentiation and transplantation. Furthermore, the lentivirus or TALEN-introduced *ASPA* transgene will likely be more stable because of integration events, therefore allowing sustained *ASPA* activity in the host brains, unlike AAV-mediated transgene delivery which is episomal, thus can have more transient expression. Our patient iPSC-derived autologous cellular products could also avoid potential immunogenicity associated with the AAV vector,<sup>[29]</sup> and have the added benefit of regenerative potential linked to cell therapy.<sup>[5b]</sup>

NPCs have been used in clinical trials and shown a favorable safety profile.<sup>[7a-d]</sup> NPCs isolated from human fetal brains have been transplanted into Pelizaeus–Merabacher disease patient brains and exhibited long-term safety after 5 years of follow up.<sup>[7c,30]</sup> No tumors or other long-term adverse effects were observed.<sup>[7c]</sup> Besides the favorable safety profile, the expandability and short manufacturing protocol make iNPCs a relatively economic and accessible cell source for cell therapy.

OPCs are another desirable cell therapy candidate for leukodystrophies including Canavan disease.<sup>[9,31]</sup> This study and previous studies<sup>[10b,32]</sup> have shown that OPCs can migrate widely after intracerebral transplantation, rendering OPCs a desired vector for widespread delivery. Moreover, it has been shown that the transplanted OPCs can differentiate into oligodendrocytes and myelinate dysmyelinated loci throughout the brain.<sup>[10b,11,32]</sup> In this study, we showed that the ASPA iOPCs can migrate out of the injection sites, and rescue disease phenotypes dramatically in a leukodystrophy mouse model. However, compared to iNPCs, the differentiation protocol for iOPCs is more complex (requiring multiple growth factors), more time-consuming and costly. It takes about 70 days or more to differentiate from human iPSCs to iOPCs,<sup>[10a,c]</sup> whereas differentiation from human iPSCs to iNPC only needs 8 days.<sup>[8]</sup> Moreover, the iNPCs are of high purity and can be easily expanded to produce enough cells for

human applications.<sup>[30]</sup> The current protocol for iOPC differentiation can only produce limited number of cells and iOPCs are not as easy to maintain and expand. Further optimized protocol for iOPC differentiation with shorter differentiation time, simpler procedure with less expensive reagents, and higher differentiation efficiency may facilitate the application of iOPCs into the clinic in the future.

It is worth noting that although the ASPA iNPCs did not migrate in the brain after transplantation, they were able to rescue the disease phenotypes in a robust and sustainable manner. One explanation for these unexpected results is because NAA travels in the brain through an intercompartmental cycling via extracellular fluids, between its anabolic compartment in neurons and catabolic compartment in oligodendrocytes<sup>[33]</sup> or transplanted ASPA iNPCs in this case. After NAA is released from neurons, it can move to the transplanted cells that have ASPA activity through a concentration gradient, therefore leading to widespread reduction of NAA level, and consequently extensive rescue of spongy degeneration and myelination defect in the brain.

Unlimited source of cells derived from iPSCs and the low risk of immune rejection associated with autologous cell transplantation render human iPSC-based autologous cellular products great potential for regenerative medicine.<sup>[5b]</sup> Indeed, the first clinical study using human iPSC-based product was initiated in 2014, in which autologous retinal pigment epithelium sheets derived from patient's own iPSCs were transplanted back to the patient. This treatment has resulted in favorable outcome, halting macular degeneration in the absence of anti-VEGF drug administration.<sup>[34]</sup>

Despite the huge advantage associated with human iPSC-derived cellular products, there remain issues related to iPSC-based cell therapy, including teratoma formation and high cost of individualized cell products. To address the safety concern associated with potential development of teratoma from iPSC products, we developed a standard operation procedure (SOP) that allows efficient and reproducible differentiation of iPSCs into iNPCs with undetectable residual iPSCs. Whether there were any residual iPSCs in ASPA iNPCs was tested using both FACS analysis and RT-qPCR assay and a stringent release specification was set for the ASPA iNPC products. The residual iPSCs in all six ASPA iNPC products were below the detection limit for both FACS and RT-qPCR analyses. Furthermore, continuous monitoring of the ASPA iNPC-transplanted mice for up to 10 months and the ASPA iOPC-transplanted mice for 3 months revealed no sign of tumorigenesis. These results suggest the preclinical safety of our cellular products.

The use of autologous iPSCs as the source of cell therapy products comes at high cost. Ideally, an off-the-shelf allogenic product would address this concern. The use of allogeneic iPSCs, in which a single lot of cells could be used to treat multiple patients, would bring down the cost for iPSC-based cell product manufacturing. However, this would come at the price of immune rejection caused by human leukocyte antigen (HLA) mismatching and, thus, poses a major challenge for allogeneic transplantation. The rejection issue has typically been addressed through immunosuppression, which has been effective but can itself be costly and its serious side effects for long term application<sup>[35]</sup> would further complicate the management of these CD patients.



The approach taken in Japan by using iPSC stocks from HLA homozygous donors to cover most HLA haplotypes<sup>[36]</sup> would not likely be effective in CD which is associated with a diverse genetic background. An alternative approach manipulates the immune responses through gene editing to overcome immune rejection associated with allogeneic transplantation.<sup>[37]</sup> This approach has great potential to generate universal donor cells, but brings its own safety concerns, for example, the potential of increased tumorigenicity due to compromised immune surveillance. From the immunological point of view, autologous transplantation is ideal for cell therapy because these cells may avoid any potential immune-mediated complications. It is anticipated that the cost of iPSC-based cell therapy manufacturing will be reduced with the availability of low-cost reagents,<sup>[38]</sup> and derisking of GMP manufacturing through the development of GMP-compatible processes as described in this study that are cost-effective and easily transferrable to GMP.

#### 4. Conclusion

Leukodystrophies are among the most debilitating neurological disorders, and are appealing targets for cell therapies because there is no need for the grafted cells to integrate into the existing neural network.<sup>[9]</sup> This study provides important preclinical efficacy data for developing a therapeutic candidate for CD, a devastating leukodystrophy that has neither a cure nor a standard treatment. This is the first application of human iPSC technology in developing a stem cell therapy for CD. It provides a robust proof-of-principle for cell therapy development of this and other diseases of this kind. The feasibility and efficacy study presented here represents a critical step toward bringing the human iPSC-derived cellular products into the clinic for the treatment of CD and related diseases.

#### 5. Experimental Section

**CD iPSC Production:** CD iPSCs were manufactured using an integration-free, xeno-free, and feeder-free method by following the specific SOP was established in this study. Specifically, CD patient fibroblasts CD59 (Coriell, GM00059), CD60 (Coriell, GM00060), CD68 (Coriell, GM04268), CD92 (ID 21 282, Biobank code FFF0871992, Telethon), CD00 (ID 22 217, Biobank code FFF0282000, Telethon), and CD01 (ID 22 276, Biobank code FFF0082001, Telethon) were reprogrammed using episomal vectors expressing human OCT4, SOX2, KLF4, L-MYC, LIN28, and p53 shRNA (sh-p53) (Addgene plasmids pCXLE-hSK, pCXLEhUL, pCXLE-hOCT3/4-shp53-F, and pCXWB-EBNA1, Table S6, Supporting Information) as described.<sup>[12]</sup> Cells electroporated with the reprogramming vectors using 4D Nucleofector (Lonza) were seeded onto plates coated with recombinant human Laminin-521 matrix (Thermo Fisher, A29249) and maintained in Essential 8 (E8) medium (Thermo Fisher, A1517001), a xeno-free medium. iPSC clones were picked around day 20 and expanded in E8 medium. For immunostaining, iPSCs were passage and seeded on 12-well Laminin-521-coated plates for 2–3 days. The resultant iPSC clones were ready for staining.

**Differentiation of CD iPSCs into CD iNPCs:** CD iPSCs were differentiated iNPCs on recombinant human Laminin-521-coated plates by following the SOP that was developed following an established protocol.<sup>[8]</sup> To start neural induction, human iPSCs were dissociated into single cells, seeded onto Laminin-521-coated plate, and cultured in E8 medium. After 2 days, cells were switched to Neural Induction Medium 1 (NIM-1) containing Dulbecco's Modified Eagle Medium: Nutrient Mixture F-

12 (DMEM/F12, Thermo Fisher, 11 330 032), 1x N2 (Thermo Fisher, 17502048), 1x B27 (Thermo Fisher, 12587010), 1x NEAA (Gibco, 11 140 076),  $2 \times 10^{-3}$  M GlutaMAX (Thermo Fisher, 35 050 061),  $0.1 \times 10^{-6}$  M RA (Sigma, R2625),  $4 \times 10^{-6}$  M CHIR99021 (Cellagen Technology, C2447),  $3 \times 10^{-6}$  M SB431542 (Peppercell, 04-0010-10),  $2 \times 10^{-6}$  M Dorsomorphin (Sigma, P5499), and  $10 \text{ ng mL}^{-1}$  hLIF (Millipore Sigma, GF342). Cells were cultured in NIM-1 for 2 days, then switched to Neural Induction Medium 2 (NIM-2) containing DMEM/F12, 1x N2, 1x B27, 1x NEAA,  $2 \times 10^{-3}$  M GlutaMAX,  $0.1 \times 10^{-6}$  M RA,  $4 \times 10^{-6}$  M CHIR99021,  $3 \times 10^{-6}$  M SB431542, and  $10 \text{ ng mL}^{-1}$  hLIF with daily medium change for 5 days. The resultant iNPCs were dissociated and cultured in Neural Progenitor Maintenance Medium containing DMEM/F12, 1x N2, 1x B27,  $2 \times 10^{-3}$  M GlutaMAX,  $0.1 \times 10^{-6}$  M RA,  $3 \times 10^{-6}$  M CHIR99021,  $2 \times 10^{-6}$  M SB431542,  $10 \text{ ng mL}^{-1}$  EGF (PeproTech, 100–18b), and  $10 \text{ ng mL}^{-1}$  FGF (PeproTech, 100–15), with medium change every other day. The CD iNPCs were expanded and cells before passage 6 were used. For immunostaining, dissociated single cells were seeded on Matrigel (Corning, 354 230)-coated coverslip in 24 well plates for 2–3 days.

**ASPA Viral Preparation and Transduction:** The cloned DNA that was used for genetic modification of CD iNPCs consists of the sequence of a functional human ASPA gene under the control of the constitutive human EF1 $\alpha$  promoter. The human ASPA coding sequence was PCR-amplified using the ASPA cDNA clone MGC:34 517 (IMAGE: 5 180 104) as the template. The ASPA cDNA was cloned into the pSIN lentiviral vector downstream of the EF1 $\alpha$  promoter. The EF1 $\alpha$  promoter and the ASPA cDNA fragments were subsequently PCR-amplified using the pSIN-ASPA as the template and subcloned into the self-inactivating pHIV7 lentiviral vector described previously.<sup>[24,39]</sup> The resultant lentiviral vector was called LV-EF1 $\alpha$ -hASPA. In order to track the transplanted cells in patient brain, a point mutation was created in the ASPA gene by changing the codon of Arginine (AGG) at amino acid residue 132 to that of Glycine (GGG). Arginine 132 was selected for mutation because it is located outside of the catalytic center of the ASPA protein. To package the ASPA-expressing lentivirus, the LV-EF1 $\alpha$ -hASPA transgene vector, together with the VSV-G, REV, and MDL packaging vectors were transfected into HEK 293T cells using the calcium phosphate transfection method as was described previously.<sup>[40]</sup> 48 h after transfection, virus was harvested, concentrated by ultracentrifugation and stocked in  $-80^\circ\text{C}$ . For lentiviral transduction,  $1.5 \times 10^6$  dissociated single NPCs were seed in T25 flask and viruses were added when cells were attached. Then ASPA iNPCs were lifted and expanded in suspension culture. The ASPA iNPC before passage 6 were used for characterization and transplantation.

**Generation of the ASPA-CD68 iPSCs Using TALEN Editing:** The ASPA-CD68 iPSCs were generated by TALEN-mediated gene editing. The hAAVS1 TALEN left and right vectors were used for TALEN-mediated targeting of the AAVS1 locus as described.<sup>[41]</sup> The donor vector was constructed using the AAVS1-CAG-hrGFP vector by inserting the EF1 $\alpha$ -ASPA-T2A-CD19t fragment between the AAVS1 left and right arm. The hAAVS1 TALEN left and right vectors and the donor plasmid were delivered via nucleofection into CD68 iPSCs. The transfected iPSCs were sorted by using the CD19 antibody and seeded as single cells. The single cell-derived clones were picked and screened by PCR. Three primers: AAVS1-Fwd, AAVS1-Rev, and ASPA-Rev, were designed for genotyping of the iPSC clones. Three iPSC clones with homozygous insertion were chosen, expanded, and stocked. The CD68T-13 iPSC clone was randomly selected from these three clones for further experiments. The hAAVS1 TALEN Right, hAAVS1 TALEN Left, and AAVS1-CAG-hrGFP vectors were gifts from Dr. Su-Chun Zhang (Table S6, Supporting Information).

**Whole Genome Sequencing and TALEN Off-Target Analysis:** Genomic DNA from control CD iPSCs and TALEN-edited ASPA iPSCs were subjected to whole genome sequencing using the BGISEQ 500 (MGI Tech). High quality genomic DNA was purified from the cells using Wizard SV Genomic DNA Purification System (Promega, A2360) and quantified using Qubit 3.0 fluorometer. For sequencing library generation, the genomic DNA was fragmented into sizes of 50–800 bp using ultrasound-based fragmentation (Covaris E220). The fragmented DNA were further selected with AMPure XP beads (Beckman Coulter, A63881) to enrich DNA of 100–300 bp, which were then repaired with a blunt ending enzyme and by

addition of 3' A overhang. A \*T\* tailed adapter was ligated to both ends of the DNA fragments and amplified by PCR (8 cycles). The PCR product was then denatured and annealed with a single strand bridging DNA that is reverse-complemented to both ends of the PCR product to generate single-strand circular DNA. The single-strand molecule was ligated using a DNA ligase. The excessive linear molecule was digested with the exonuclease. DNA nanoballs (DNB) were then generated from the single-strand circular DNA according to the manufacturer's instruction (MGI Tech) and sequenced with BGISEQ-500 using pair-end 100 cycles. For each sample, coverage of over 30X was generated. The sequences of DNBs were base called using the base calling software Zebra call. Calling for variants were carried out with BWA<sup>[42]</sup> and GATK.<sup>[43]</sup> Structure variation was analyzed using breakDancer (<http://www.nature.com/nmeth/journal/v6/n9/abs/nmeth.1363.html>). The potential off-target sites of TALEN were predicted using a genome wide TALEN off-target site prediction tool TALENoffer.<sup>[44]</sup> A total of 100 sites including the target site and the top 99 potential off-target sites were export from TALENoffer. The potential off-target sites were evaluated using whole genome sequencing. No mutation was found on any of these sites (Table S5, Supporting Information).

**Differentiation of ASPA-CD68 iPSCs into iOPCs:** The ASPA-CD68 iPSCs were differentiated into iOPCs by following a previously published protocol.<sup>[10c,d]</sup> Briefly, ASPA-CD68 iPSCs were dissociated into single cells and induced by OPC-I Medium containing DMEM/F12, 1x N2,  $2 \times 10^{-3}$  M GlutaMAX,  $0.1 \times 10^{-3}$  M RA (Sigma, R2625),  $10 \times 10^{-3}$  M SB431542 (Peprcell, 04-0010-10), and  $250 \times 10^{-9}$  M LDN-193189 (Peprcell, 04-0074-10) for 8 days. Then cells were switched to OPC-II Medium containing DMEM/F12, 1x N2,  $2 \times 10^{-3}$  M GlutaMAX,  $0.1 \times 10^{-6}$  M RA, and  $1 \times 10^{-6}$  M SAG (Sigma, ML1314) for another 4 days. After 12 days of culture, cells were dissociated and cultured in flasks for overnight to form spheres. The resultant pre-OPC spheres were switched to OPC-III Medium containing DMEM/F12, 1x N2, 1x B27 minus vitamin A (Thermo Fisher, 12587010),  $2 \times 10^{-3}$  M GlutaMAX,  $0.1 \times 10^{-6}$  M RA, and  $1 \times 10^{-6}$  M SAG for 8 days, and then switched to PDGF medium containing DMEM/F12, 1x N2, 1x B27 minus vitamin A,  $2 \times 10^{-3}$  M GlutaMAX,  $10 \text{ ng mL}^{-1}$  PDGF-AA (R&D, 221-AA-050),  $10 \text{ ng mL}^{-1}$  IGF-1 (R&D, 291-GG-01M),  $5 \text{ ng mL}^{-1}$  HGF (R&D, 294-HG-250),  $10 \text{ ng mL}^{-1}$  NT3 (EMD Millipore, GF031; and PeprTech, AF-450-03),  $60 \text{ ng mL}^{-1}$  T3 (Sigma, T2877),  $100 \text{ ng mL}^{-1}$  Biotin (Sigma, 4639),  $1 \times 10^{-6}$  M cAMP (Sigma, D0627), and  $25 \text{ } \mu\text{g mL}^{-1}$  Insulin (Sigma, I9278) for 10 days. After 18 days of suspension culture, the spheres were attached on Matrigel-coated plates and cultured for 30–60 days in the PDGF medium. OPCs could be detected by flow cytometry with a CD140a antibody and by live staining with an O4 antibody after 30 days of attached culture. After 30–60 days of attached culture, OPCs were collected for transplantation.

**Flow Cytometry:** Human H9 ESCs (WiCell, WA09) were used as the positive control for FACS analysis to detect the pluripotency marker OCT4 and the human ESC cell surface marker SSEA4. HEK293T cells were used as the negative cell control for iPSC and NPC marker detection. Cells were dissociated and passed through a  $70 \text{ } \mu\text{m}$  cell strainer to make single cell suspension. For cell surface marker staining, cells were directly incubated with fluorophore-conjugated primary antibodies for 20 min on ice. The same fluorophore-conjugated IgGs were included as the isotype controls. For intracellular OCT4 staining, cells were first fixed and permeabilized using a Fixation/Permeabilization Solution Kit (BD, 554714) before incubation with the PE-conjugated anti-Oct3/4 primary antibody. The PE-conjugated mouse IgG1 was included as the isotype control. Cells were washed twice and resuspended in phosphate-buffered saline (PBS) containing DAPI and 0.1% donkey serum. The samples were run on Attune NxT Flow Cytometer (ThermoFisher Scientific) and data were analyzed by FlowJo v10. The detailed information of all the primary antibodies and isotype controls used were listed in Table S7 (Supporting Information).

**Immunocytochemistry:** Cells were fixed with 4% paraformaldehyde (PFA) at room temperature (RT) for 10 min. After fixation, cells were washed with PBS twice and blocked with 5% donkey serum diluted in PBS with 0.1% triton (PBST) for 1 h at RT. The fixed cells were then incubated with primary antibodies at 4 °C for overnight. On the following day, cells were washed with PBS twice, incubated with secondary antibodies at RT for 1 h, and washed. Cells were counterstained with DAPI before mounting

for imaging. Images were taken using Nikon ECLIPSE TE2000-S or Nikon Ti-2. The detailed information of the primary antibodies used was listed in Table S7 (Supporting Information).

**Viability Assay:** The vials with frozen cells were thawed in a 37 °C water bath and the content was transferred to a 15 mL conical tube. 3 mL medium was added drop by drop and the cell suspension was centrifuged at  $200 \times g$  for 3 min. The cell pellet was resuspended in Perfusion Fluid CNS (CMAP000151, Harvard Apparatus). A small aliquot of cell suspension was further diluted by Trypan blue solution. Live and dead cells were counted by Hemocytometer. Three cryopreserved vials were tested for each cell lines.

**Sterility and Endotoxin Test:** 1–2 mL media were collected from culturing plates or flasks and sent to Department of Pathology in City of Hope to test for sterility. 1 mL media were collected from culturing plates or flasks and sent to Center for Biomedicine and Genetics and Analytical Pharmacology Core Facility of City of Hope to test for endotoxin.

**Karyotype and STR Analysis:** iPSCs in culture were directly sent to the Cytogenetics Core of City of Hope for karyotype analysis using standard G-banding method. Total 20 metaphase cells were analyzed for each sample. For STR assay, DNA was first purified from fibroblasts, iPSCs, and ASPA iNPCs. Geneprint 10 System PCR Amplification Kit (Promega, B9510) was used to generate a 10-locus DNA profile that is unique to each individual. PCR products were sent to City of Hope Integrative Genomics Core for fragment analysis. The results were analyzed using the GeneMapper Software 5 (Thermo Fisher).

**Exon Sequencing of the ASPA Genomic DNA:** Genomic DNAs were extracted from CD iPSCs using QuickExtract DNA Extraction Solution (Lucigen, QE09050). The primers used for sequencing each exon were listed in Table S8 (Supporting Information).

**ASPA Enzymatic Activity Assay for ASPA iNPCs:** The ASPA enzymatic assay was developed in the laboratory based on a published protocol.<sup>[16,45]</sup> Cell lysates were prepared using radioimmunoprecipitation assay buffer (RIPA) buffer with phenylmethylsulfonyl fluoride (PMSF) and protein concentration was determined by Bradford. For the first reaction,  $100 \text{ } \mu\text{g}$  protein lysates in  $50 \text{ } \mu\text{L}$  RIPA buffer was mixed with  $50 \text{ } \mu\text{L}$  2x Assay Buffer I with the final concentration of  $50 \times 10^{-3}$  M Tris-HCl, pH8.0,  $50 \times 10^{-3}$  M NaCl,  $0.1 \times 10^{-3}$  M DTT, 0.05% IGEPAL CA-630,  $2.5 \times 10^{-3}$  M CaCl<sub>2</sub>, and  $5 \times 10^{-3}$  M NAA. The reaction mixture was incubated at 37 °C for 1 h, and the reaction was stopped by heating the tubes at 100 °C for 3 min. After centrifugation at  $15\,000 \text{ g}$  for 5 min, the supernatant was collected for the second reaction. For the second reaction,  $90 \text{ } \mu\text{L}$  of the first reaction supernatant was added to  $90 \text{ } \mu\text{L}$  2x Assay Buffer II with the final concentration of  $50 \times 10^{-3}$  M Tris-HCl pH 8.0,  $50 \times 10^{-3}$  M NaCl,  $2.5 \times 10^{-3}$  M alpha-ketoglutarate (AKG),  $1 \text{ mg mL}^{-1}$  BSA,  $5 \times 10^{-6}$  M PLP,  $0.5 \times 10^{-3}$  M  $\beta$ -NADH, 10 units MDH, and 10 unit glutamate-oxalacetate transaminase (GOT). 20 min later, OD340 nm was determined by luminescence reader. The ASPA activity is defined by the production of aspartate in nmol by 1 mg protein lysate in 1 h at 37 °C.

**ASPA Transgene Copy Number Analysis:** Because the human ASPA transgene in the lentiviral vector was integrated into the genome together with the PBS/psi region, the copy number of the human ASPA transgene was measured by detecting the PBS/psi region.<sup>[46]</sup> Specifically, the ASPA transgene copy number was detected by TaqMan real time PCR using Step One Plus real-time PCR system (Applied Biosystems) with primers in the PBS/psi region: PBS/psi-Fwd and PBS/psi-Rev, and the PBS/psi-TaqMan probe. The Albumin gene is a single copy gene in the genome (2 copies per cell). It was included as an internal control and amplified using primers: Albumin-Fwd and Albumin-Rev, and the Albumin-TaqMan probe. The gBlock DNA fragment mixtures of psi and albumin with different ratio were amplified to create a standard curve to determine the relationship between  $\Delta\text{Ct}$  (psi-albumin) and  $\log_2$ (psi copy number). If the  $\log_2$  (psi copy number) is n for the unknown sample, the transduced hASPA copy number/Cell = power (2, n). The Ct values were determined by TaqMan real time PCR, and used to calculate the copy numbers of both Albumin and the ASPA transgene based on the standard curves. The primers and gBlocks used were listed in Table S8 (Supporting Information).

**RNA Preparation and RT-PCR Analysis:** Total RNAs were extracted from cells using TRIzol (Invitrogen, 15596018). Reverse transcription was

performed with 1  $\mu\text{g}$  of RNA using the Tetro cDNA synthesis kit (Bioline, BIO-65043). Real-time PCR was performed using DyNAmo Flash SYBR Green qPCR mix on a StepOnePlus system (Applied Biosciences) and normalized to  $\beta$ -actin. The primers used for PCR are listed in Table S8 (Supporting Information).

**Generation and Maintenance of Immunodeficient CD (Nur7) Mice:** All animal housing conditions and surgical procedures were approved by and conducted according to the Institutional Animal Care and Use Committee of City of Hope.  $ASPA^{Nur7/+}$  ( $ASPA^{Nur7/J}$ , 008607) and  $Rag2^{-/-}$  mice (B6(Cg)- $Rag2^{tm1.1Cgn/J}$ , 008449) were purchased from the Jackson Laboratory.  $ASPA^{Nur7/+}$  mice were backcrossed with  $Rag2^{-/-}$  mice for four generations and screened for homozygosity of  $ASPA^{Nur7/Nur7}$  and  $Rag2^{-/-}$  mutations. The  $ASPA^{Nur7/Nur7}/Rag2^{-/-}$  mice were called CD (Nur7) mice. The survival of the WT, Het, and CD (Nur7) mice, and the ASPA iNPC-transplanted CD (Nur7) mice was monitored for 10 months. Animal death was not counted during the first 2 months for mice of all genotypes, because death resulted from pathology versus death resulted from events associated with fostering, cannibalization, and weaning occurred during this period was not differentiated.

**Stereotaxic Transplantation:** Postnatal day 1–4 (PND 1–4) mice were anesthetized on ice for 6–7 min and then placed onto a stereotaxic device. The ASPA iNPCs in suspension were transplanted with about 600 000 cells (in 1.5  $\mu\text{L}$ ) per site into six sites in the mouse brain bilaterally using a Hamilton syringe with 33 gauge needle. The following coordinates, which were modified from a published study,<sup>[47]</sup> were used for transplantation: the corpus callosum (+3.0,  $\pm$ 1.6, –1.3), the subcortical (0.5,  $\pm$ 1.0, –2.5), and the brain stem (–1.6,  $\pm$ 0.8, –3.0). For pups with weight over 2 g and/or with head size obviously bigger than usual, slightly modified coordinates were used: the corpus callosum (+3.5,  $\pm$ 1.7, –1.4), the subcortical (0.5,  $\pm$ 1.0, –2.5), and the brain stem (–1.6,  $\pm$ 1.0, –3.1). All the coordinates are (A, L, V) with reference to Lambda. “A” stands for anteroposterior from midline, “L” stands for lateral from midline, and “V” stands for ventral from the surface of brain, respectively. The ASPA iNPCs were transplanted with about 60 000 cells (in 1.5  $\mu\text{L}$ ) per site into six sites per mouse brain using the same coordinates.

**Immunohistochemistry:** Immunohistochemistry was performed on PFA-fixed tissues. Animals were deeply anesthetized and transcardially perfused with ice cold 0.9% saline followed by 4% PFA. Perfused brains were removed and postfixed in 4% PFA, then cryoprotected with 30% sucrose. Cryoprotected brains were flash frozen and stored at –20 °C. Then the brains were serially cryosectioned at sagittal planes. Specifically, slides were first labeled. Serial sections were collected onto labeled slides with one section per slide, until all slides were used for collection. Repeat the procedure until all sections from a brain were collected. For immunohistochemistry analysis, brain sections were permeabilized in PBST for 2  $\times$  10 min, blocked with 5% donkey serum in PBST for 1 h at RT. Sections were then incubated with primary antibodies (Table S7, Supporting Information) at 4 °C for overnight. Following primary antibody incubation and washes, sections were incubated with secondary antibodies at RT for 2 h, washed with 1  $\times$  PBS, counterstained with Dapi, and mounted with the mounting medium. Cell fate and proliferation status were assessed by double immunostaining using the antihuman nuclear antigen (hNA) together with antibodies against PAX6, NeuN, SOX9, OLIG2, or Ki67. Confocal microscopy was performed on a Zeiss LSM 700 microscope (Zeiss), and the resulting images were analyzed with Zen 2.3 lite software (Zeiss). For quantification, images of transplanted cells in all three targeting sites including the corpus callosum, the subcortical and the brain stem regions were taken. Total human cells and double positive cells were counted for each brain. Three brains were analyzed in each group. Tiled whole section sagittal images were taken using Nikon Ti-2 and dot maps were made using Photoshop CS4 based on the hNu<sup>+</sup> signal from the tiled whole section sagittal images.

**NAA Level and ASPA Activity Measurement in Brain Tissues:** Aqueous metabolites were extracted from mouse brains using the method of perchloric acid (PCA, Sigma, 244 252) as described.<sup>[48]</sup> Briefly, mouse brains were rapidly chopped into small pieces, mixed well and divided into aliquots. Two aliquots were placed into two 1.5 mL Eppendorf tubes. Brain tissues in one tube were subjected to PCA extraction directly, while tissues

in another tube were incubated at 37 °C for 1 h followed by PAC extraction. 6% ice-cold PCA was added into each tube at 5 mL  $\text{g}^{-1}$  of wet brain tissues, followed by vortexing for 30 s. The samples were incubated on ice for additional 10 min. The mixture was centrifuged at 12 000  $\times$  g for 10 min at 4 °C. The supernatant was transferred into a new tube, neutralized with 2 M  $\text{K}_2\text{CO}_3$ , and placed on ice with lids open to allow  $\text{CO}_2$  to escape. Each sample was incubated on ice for 30 min to precipitate the potassium perchlorate salt. Supernatant was collected and pH was adjusted. Samples were centrifuged at 12 000  $\times$  g for 10 min at 4 °C. Supernatant was transferred to Eppendorf tubes and frozen on dry ice. Samples were then subjected to NMR analysis at the NMR Core Facility of City of Hope. The ASPA activity was calculated using the difference of NAA levels before and after 1 h incubation at 37 °C, and expressed as decreased NAA level in nmol per gram of brain tissue per hour.

**Hematoxylin and Eosin Staining and Vacuolation Analysis:** A one-in-six series of whole brain slides were stained with H&E at the Pathology Core of City of Hope. The whole slide was scanned under Nanozoomer HT (Hamamatsu Photonics, Japan) at the Light Microscopy Core of City of Hope. The surface area of the vacuolated brain regions and the intact brain regions was measured using Image-Pro Premier 9.2 for all sections. The percent vacuolation = [(the area of vacuolated brain region)/(the area of vacuolated brain region + the area of intact brain region)]  $\times$  100. All sections from one representative slide of each brain were analyzed and at least three brains were analyzed for each mouse group.

**EM and G-Ratio Analysis of Myelin Sheaths:** Mice were deeply anesthetized with isoflurane, and perfused with 0.9% saline followed by 0.1 M Millonig’s buffer containing 4% PFA and 2.5% glutaraldehyde. Brain tissues were dissected and postfixed in the same fixative overnight. We followed a heavy metal staining protocol developed by Dr. Mark Ellisman’s group.<sup>[49]</sup> Target tissues were cut into about 150  $\mu\text{m}$  vibratome sections using a Leica VT 1000S vibratome. The subcortical white matter of the brain was microdissected and embedded in Durcupan ACM resin (Electron Microscopy Sciences). Ultrathin sections were cut using a Leica Ultracut UCT ultramicrotome and picked onto EM grids. Transmission electron microscopy was performed on an FEI Tecnai 12 transmission electron microscope equipped with a Gatan Ultrascan 2K CCD camera at the EM Core Facility of City of Hope. Three to four images were randomly taken for each sample in the subcortical region (3 images for the HET and the transplanted mice, respectively, and four images for CD (Nur7) mice). The inner axonal diameter and the total outer diameter of total 15 myelin sheaths in the brain of the Het and the transplanted mice, respectively, and 17 myelin sheaths in the brain of the CD (Nur7) mice were measured using Image-Pro Premier 9.2. The g-ratio is the ratio of the inner axonal diameter to the total outer diameter. The abnormal myelin sheaths were further identified based on the layer structure of the myelin sheaths which exhibited substantial difference between the Het and the CD (Nur7) mice.

**Rotarod Test:** The motor performance of the ASPA iNPC-transplanted mice was evaluated using a rotarod treadmill (Rotamex, Columbus Instruments) as described.<sup>[17]</sup> Mice were tested for the latency on the rod when the rod was rotating at the accelerating speed (2–65 rpm) in a 2 min trial session. Each mouse was monitored for the latency 4 times per test. At least 6 mice for each group were tested.

**Grip Strength Test:** The forelimb strength of the transplanted mice was measured using a grip strength meter (BIO-GS3, Bioseb) to detect motor coordination and motor function. Mouse was allowed to grip a metal grid tightly. The grip strength of the mouse was recorded by gently pulling the tail of the mouse backward until release. Four sequential measurements were performed, and the average strength was calculated. At least 6 mice for each group were tested.

**Mycoplasma Test:** All cell culture products including iPSCs, iNPCs, and iOPCs were checked for potential mycoplasma contamination using MycoAlert PLUS Mycoplasma Detection Kit (Lonza). 500  $\mu\text{L}$  culture medium was harvested from each cell line and centrifuged at 200  $\times$  g for 5 min to eliminate cell debris. 100  $\mu\text{L}$  medium was used for each reaction and duplicate reactions were run for each sample. The result was determined by luminescence reading according to the established SOP. All cellular products used in this study were mycoplasma negative.



**Statistical Analyses:** Data are shown as means  $\pm$  SE as specified in the figure legends and analyzed with GraphPad Prism 8 (San Diego, CA) and KaleidaGraph 4.0 (Reading, PA). The number of mice analyzed per treatment group is indicated as “*n*” in the corresponding figure legends. No exclusion criteria were applied. Animals were assigned randomly to treatment groups. The study was not blinded. Student’s *t*-test (two tailed), Log-rank test, and One-Way ANOVA followed by Dunnett’s multiple comparisons test or Tukey’s multiple comparisons test were used for statistical analysis as reported in each figure legend.  $P < 0.05$  was considered statistically significant. \* $P < 0.05$ , \*\* $P < 0.01$ , and \*\*\* $P < 0.001$ .

## Supporting Information

Supporting Information is available from the Wiley Online Library or from the author.

## Acknowledgements

L.F., J.C., E.T., and L.L. contributed equally to this work. The authors would like to thank Dr. J. Zaia for his advice throughout the study, Dr. X. Wang for sharing the CD19t-expressing vector, Dr. T. Reignier for SOP editing, Shafnez Iqbal, Elizabeth Tannous, Padmaja Thomas, Rebecca Shakeley, and Yasmine Shad for quality assurance, Ariana Silva-Torres, Kevin Zhao, Samuel Crawford, Marvin Huynhle, Cheng Wang, WooSung Ahn, Mingzi Zhang, Xingqiang Li, and Lingzhi Li for technical assistance. This work was supported by the Louise and Herbert Horvitz Charitable Foundation, the Sidell Kagan Foundation, California Institute for Regenerative Medicine TRAN1-08525, and the National Institute of Aging of the National Institutes of Health R01 AG056305, R01 AG061794, and R56 AG061171 to Y.S. Research reported in this publication was also supported by the National Cancer Institute of the National Institutes of Health under Award No. P30CA33572. The content is solely the responsibility of the authors and does not necessarily represent the official views of the National Institutes of Health.

## Conflict of Interest

The authors declare no conflict of interest.

## Keywords

Canavan disease, iPSCs, leukodystrophy, neural progenitor cells (NPCs), neurological diseases, oligodendrocyte progenitor cells (OPCs), stem cell therapy

Received: June 9, 2020

Revised: August 22, 2020

Published online: October 29, 2020

- [1] R. Matalon, K. Michals, D. Sebesta, M. Deanching, P. Gashkoff, J. Casanova, *Am. J. Med. Genet.* **1988**, 29, 463.
- [2] a) R. M. Matalon, K. Michals-Matalon, *Front Biosci.* **2000**, 5, D307; b) L. van Bogaert, I. Bertrand, *Acta Neurol.* **1949**, 49, 572.
- [3] P. Leone, D. Shera, S. W. McPhee, J. S. Francis, E. H. Kolodny, L. T. Bilaniuk, D. J. Wang, M. Assadi, O. Goldfarb, H. W. Goldman, A. Freese, D. Young, M. J. During, R. J. Samulski, C. G. Janson, *Sci. Transl. Med.* **2012**, 4, 165ra163.
- [4] P. Leone, C. G. Janson, L. Bilaniuk, Z. Wang, F. Sorgi, L. Huang, R. Matalon, R. Kaul, Z. Zeng, A. Freese, S. W. McPhee, E. Mee, M. J. During, *Ann. Neurol.* **2000**, 48, 27.

- [5] a) M. Desgres, P. Menasche, *Cell Stem Cell* **2019**, 25, 594; b) Y. Shi, H. Inoue, J. C. Wu, S. Yamanaka, *Nat. Rev. Drug Discovery* **2017**, 16, 115.
- [6] a) K. Takahashi, K. Tanabe, M. Ohnuki, M. Narita, T. Ichisaka, K. Tomoda, S. Yamanaka, *Cell* **2007**, 131, 861; b) J. Yu, M. A. Vodyanik, K. Smuga-Otto, J. Antosiewicz-Bourget, J. L. Frane, S. Tian, J. Nie, G. A. Jonsdottir, V. Ruotti, R. Stewart, Slukvin II, J. A. Thomson, *Science* **2007**, 318, 1917; c) W. E. Lowry, L. Richter, R. Yachechko, A. D. Pyle, J. Tchiew, R. Sridharan, A. T. Clark, K. Plath, *Proc. Natl. Acad. Sci. USA* **2008**, 105, 2883; d) I. H. Park, R. Zhao, J. A. West, A. Yabuuchi, H. Huo, T. A. Ince, P. H. Lerou, M. W. Lensch, G. Q. Daley, *Nature* **2008**, 457, 141.
- [7] a) E. Curtis, J. R. Martin, B. Gabel, N. Sidhu, T. K. Rzesiewicz, R. Manville, S. Van Gorp, M. Leerink, T. Tadokoro, S. Marsala, C. Jamieson, M. Marsala, J. D. Ciacci, *Cell Stem Cell* **2018**, 22, 941; b) J. D. Glass, V. S. Hertzberg, N. M. Boullis, J. Riley, T. Federici, M. Polak, J. Bordeau, C. Fournier, K. Johe, T. Hazel, M. Cudkowicz, N. Atassi, L. F. Borges, S. B. Rutkove, J. Duell, P. G. Patil, S. A. Goutman, E. L. Feldman, *Neurology* **2016**, 87, 392; c) N. Gupta, R. G. Henry, S. M. Kang, J. Strober, D. A. Lim, T. Ryan, R. Perry, J. Farrell, M. Ulman, R. Rajalingam, A. G. Pyle, S. L. Huhn, A. J. Barkovich, D. H. Rowitch, *Stem Cell Rep.* **2019**, 13, 254; d) J. A. Steinbeck, L. Studer, *Neuron* **2015**, 86, 187; e) E. S. Rosenzweig, J. H. Brock, P. Lu, H. Kumamaru, E. A. Salegio, K. Kadoya, J. L. Weber, J. J. Liang, R. Moseanko, S. Hawbecker, J. R. Huie, L. A. Havton, Y. S. Nout-Lomas, A. R. Ferguson, M. S. Beattie, J. C. Bresnahan, M. H. Tuszynski, *Nat. Med.* **2018**, 24, 484.
- [8] G. H. Liu, J. Qu, K. Suzuki, E. Nivet, M. Li, N. Montserrat, F. Yi, X. Xu, S. Ruiz, W. Zhang, U. Wagner, A. Kim, B. Ren, Y. Li, A. Goebel, J. Kim, R. D. Soligalla, I. Dubova, J. Thompson, J. Yates, 3rd, C. R. E., I. Sancho-Martinez, J. C. Izpisua Belmonte, *Nature* **2012**, 491, 603.
- [9] S. A. Goldman, *Cell Stem Cell* **2016**, 18, 174.
- [10] a) J. Piao, T. Major, G. Auyeung, E. Polcarpio, J. Menon, L. Droms, P. Gutin, K. Uryu, J. Tchiew, D. Soulet, V. Tabar, *Cell Stem Cell* **2015**, 16, 198; b) S. Wang, J. Bates, X. Li, S. Schanz, D. Chandler-Militello, C. Levine, N. Maherali, L. Studer, K. Hochedlinger, M. Windrem, S. A. Goldman, *Cell Stem Cell* **2013**, 12, 252; c) P. Douvaras, V. Fossati, *Nat. Protoc.* **2015**, 10, 1143; d) L. Li, E. Tian, X. Chen, J. Chao, J. Klein, Q. Qu, G. Sun, G. Sun, Y. Huang, C. D. Warden, P. Ye, L. Feng, X. Li, Q. Cui, A. Sultan, P. Douvaras, V. Fossati, N. E. Sanjana, A. D. Riggs, Y. Shi, *Cell Stem Cell* **2018**, 23, 239.
- [11] P. Douvaras, J. Wang, M. Zimmer, S. Hanchuk, M. A. O’Bara, S. Sadiq, F. J. Sim, J. Goldman, V. Fossati, *Stem Cell Rep.* **2014**, 3, 250.
- [12] a) K. Okita, Y. Matsumura, Y. Sato, A. Okada, A. Morizane, S. Okamoto, H. Hong, M. Nakagawa, K. Tanabe, K. Tezuka, T. Shibata, T. Kunisada, M. Takahashi, J. Takahashi, H. Saji, S. Yamanaka, *Nat. Methods* **2011**, 8, 409; b) K. Okita, T. Yamakawa, Y. Matsumura, Y. Sato, N. Amano, A. Watanabe, N. Goshima, S. Yamanaka, *Stem Cells* **2013**, 31, 458; c) C. Kime, T. A. Rand, K. N. Ivey, D. Srivastava, S. Yamanaka, K. Tomoda, *Curr. Protoc. Hum. Genet.* **2015**, 87, 21.2.1.
- [13] R. Kaul, G. P. Gao, M. Aloya, K. Balamurugan, A. Petrosky, K. Michals, R. Matalon, *Am. J. Hum. Genet.* **1994**, 55, 34.
- [14] a) R. Matalon, K. Michals-Matalon, *Adv. Pediatr.* **1999**, 46, 493; b) R. Kaul, G. P. Gao, K. Balamurugan, R. Matalon, *Nat. Genet.* **1993**, 5, 118.
- [15] S. Charrier, M. Ferrand, M. Zerbato, G. Precigout, A. Viorneri, S. Bucher-Laurent, S. Benkhalifa-Ziyyat, O. W. Merten, J. Perea, A. Galy, *Gene Ther.* **2011**, 18, 479.
- [16] C. N. Madhavarao, J. A. Hammer, R. H. Quarles, M. A. Nambodiri, *Anal. Biochem.* **2002**, 308, 314.
- [17] M. Traka, R. L. Wollmann, S. R. Cerda, J. Dugas, B. A. Barres, B. Popko, *J. Neurosci.* **2008**, 28, 11537.
- [18] Y. Shinkai, G. Rathbun, K. P. Lam, E. M. Oltz, V. Stewart, M. Mendelsohn, J. Charron, M. Datta, F. Young, A. M. Stall, F. W. Alt, *Cell* **1992**, 68, 855.



- [19] a) R. Matalon, P. L. Rady, K. A. Platt, H. B. Skinner, M. J. Quast, G. A. Campbell, K. Matalon, J. D. Ceci, S. K. Tying, M. Nehls, S. Surendran, J. Wei, E. L. Ezell, S. Szucs, *J. Gene Med.* **2000**, *2*, 165; b) N. Mersmann, D. Tkachev, R. Jelinek, P. T. Roth, W. Mobius, T. Ruhwedel, S. Ruhle, W. Weber-Fahr, A. Sartorius, M. Klugmann, *PLoS One* **2011**, *6*, e20336.
- [20] a) N. W. Dunham, T. S. Miya, *J. Am. Pharm. Assoc.* **1957**, *46*, 208; b) B. J. Jones, D. J. Roberts, *J. Pharm. Pharmacol.* **1968**, *20*, 302.
- [21] J. N. Crawley, *Brain Res.* **1999**, *835*, 18.
- [22] F. J. Sim, C. R. McClain, S. J. Schanz, T. L. Protack, M. S. Windrem, S. A. Goldman, *Nat. Biotechnol.* **2011**, *29*, 934.
- [23] a) R. Matalon, K. Michals, R. Kaul, *J. Pediatr.* **1995**, *127*, 511; b) S. S. Ahmed, G. Gao, *JIMD Rep.* **2015**, *19*, 11; c) H. Hoshino, M. Kubota, *Pediatr. Int.* **2014**, *56*, 477.
- [24] C. E. Brown, D. Alizadeh, R. Starr, L. Weng, J. R. Wagner, A. Naranjo, J. R. Ostberg, M. S. Blanchard, J. Kilpatrick, J. Simpson, A. Kurien, S. J. Priceman, X. Wang, T. L. Harshbarger, M. D'Apuzzo, J. A. Ressler, M. C. Jensen, M. E. Barish, M. Chen, J. Portnow, S. J. Forman, B. Badie, *N. Engl. J. Med.* **2016**, *375*, 2561.
- [25] X. Wang, W. C. Chang, C. W. Wong, D. Colcher, M. Sherman, J. R. Ostberg, S. J. Forman, S. R. Riddell, M. C. Jensen, *Blood* **2011**, *118*, 1255.
- [26] a) J. P. Guilinger, V. Pattanayak, D. Reyon, S. Q. Tsai, J. D. Sander, J. K. Joung, D. R. Liu, *Nat. Methods* **2014**, *11*, 429; b) D. Hockemeyer, H. Wang, S. Kiani, C. S. Lai, Q. Gao, J. P. Cassidy, G. J. Cost, L. Zhang, Y. Santiago, J. C. Miller, B. Zeitler, J. M. Cherone, X. Meng, S. J. Hinkley, E. J. Rebar, P. D. Gregory, F. D. Urnov, R. Jaenisch, *Nat. Biotechnol.* **2011**, *29*, 731; c) C. Mussolino, R. Morbitzer, F. Lutge, N. Danneemann, T. Lahaye, T. Cathomen, *Nucleic Acids Res.* **2011**, *39*, 9283; d) M. Boettcher, M. T. McManus, *Mol. Cell* **2015**, *58*, 575.
- [27] a) C. Janson, S. McPhee, L. Bilaniuk, J. Haselgrove, M. Testaiuti, A. Freese, D. J. Wang, D. Shera, P. Hurh, J. Rupin, E. Saslow, O. Goldfarb, M. Goldberg, G. Larijani, W. Sharrar, L. Liouterman, A. Camp, E. Kolodny, J. Samulski, P. Leone, *Hum. Gene Ther.* **2002**, *13*, 1391; b) R. Matalon, S. Surendran, P. L. Rady, M. J. Quast, G. A. Campbell, K. M. Matalon, S. K. Tying, J. Wei, C. S. Peden, E. L. Ezell, N. Muzyczka, R. J. Mandel, *Mol. Ther.* **2003**, *7*, 580; c) S. W. McPhee, J. Francis, C. G. Janson, T. Serikawa, K. Hyland, E. O. Ong, S. S. Raghavan, A. Freese, P. Leone, *Mol. Brain Res.* **2005**, *135*, 112; d) S. W. McPhee, C. G. Janson, C. Li, R. J. Samulski, A. S. Camp, J. Francis, D. Shera, L. Lioutermann, M. Feely, A. Freese, P. Leone, *J. Gene Med.* **2006**, *8*, 577; e) S. S. Ahmed, H. Li, C. Cao, E. M. Sikoglu, A. R. Denninger, Q. Su, S. Eaton, A. A. Liso Navarro, J. Xie, S. Szucs, H. Zhang, C. Moore, D. A. Kirschner, T. N. Seyfried, T. R. Flotte, R. Matalon, G. Gao, *Mol. Ther.* **2013**, *21*, 2136; f) J. S. Francis, I. Wojtas, V. Markov, S. J. Gray, T. J. McCown, R. J. Samulski, L. T. Bilaniuk, D. J. Wang, D. C. De Vivo, C. G. Janson, P. Leone, *Neurobiol. Dis.* **2016**, *96*, 323; g) S. S. Ahmed, S. A. Schattgen, A. E. Frakes, E. M. Sikoglu, Q. Su, J. Li, T. G. Hampton, A. R. Denninger, D. A. Kirschner, B. Kaspar, R. Matalon, G. Gao, *Mol. Ther.* **2016**, *24*, 1030; h) D. J. Gessler, D. Li, H. Xu, Q. Su, J. Sanmiguel, S. Tuncer, C. Moore, J. King, R. Matalon, G. Gao, *JCI insight* **2017**, *2*, e90807; i) G. von Jonquieres, Z. H. T. Spencer, B. D. Rowlands, C. B. Klugmann, A. Bongers, A. E. Harasta, K. E. Parley, J. Cederholm, O. Teahan, R. Pickford, F. Delerue, L. M. Ittner, D. Frohlich, C. A. McLean, A. S. Don, M. Schneider, G. D. Housley, C. D. Rae, M. Klugmann, *Acta Neuropathol.* **2018**, *135*, 95; j) M. H. Baslow, *J. Inherited Metab. Dis.* **2017**, *40*, 627; k) S. Starling, *Nat. Rev. Neurol.* **2018**, *14*, 4.
- [28] a) V. Hull, Y. Wang, T. Burns, S. Zhang, S. Sternbach, J. McDonough, F. Guo, D. Pleasure, *Ann. Neurol.* **2020**, *87*, 480; b) P. Bannerman, F. Guo, O. Chechneva, T. Burns, X. Zhu, Y. Wang, B. Kim, N. K. Singhal, J. A. McDonough, D. Pleasure, *Mol. Ther.* **2018**, *26*, 793.
- [29] P. Colella, G. Ronzitti, F. Mingozi, *Mol. Ther.–Methods Clin. Dev.* **2018**, *8*, 87.
- [30] N. Gupta, R. G. Henry, J. Strober, S. M. Kang, D. A. Lim, M. Bucci, E. Caverzasi, L. Gaetano, M. L. Mandelli, T. Ryan, R. Perry, J. Farrell, R. J. Jeremy, M. Ulman, S. L. Huhn, A. J. Barkovich, D. H. Rowitch, *Sci. Transl. Med.* **2012**, *4*, 155ra137.
- [31] S. A. Goldman, M. Nedergaard, M. S. Windrem, *Science* **2012**, *338*, 491.
- [32] a) M. S. Windrem, S. J. Schanz, M. Guo, G. F. Tian, V. Washco, N. Stanwood, M. Rasband, N. S. Roy, M. Nedergaard, L. A. Havton, S. Wang, S. A. Goldman, *Cell Stem Cell* **2008**, *2*, 553; b) M. S. Windrem, M. C. Nunes, W. K. Rashbaum, T. H. Schwartz, R. A. Goodman, G. McKhann, 2nd, N. S. Roy, S. A. Goldman, *Nat. Med.* **2004**, *10*, 93.
- [33] M. H. Baslow, *Neurochem. Res.* **2003**, *28*, 941.
- [34] M. Mandai, Y. Kurimoto, M. Takahashi, *N. Engl. J. Med.* **2017**, *377*, 792.
- [35] J. I. Pearl, L. S. Kean, M. M. Davis, J. C. Wu, *Sci. Transl. Med.* **2012**, *4*, 164ps25.
- [36] M. Umekage, Y. Sato, N. Takasu, *Inflammation Regener.* **2019**, *39*, 17.
- [37] a) G. G. Gornalusse, R. K. Hirata, S. E. Funk, L. Riobobos, V. S. Lopes, G. Manske, D. Prunkard, A. G. Colunga, L. A. Hanafi, D. O. Clegg, C. Turtle, D. W. Russell, *Nat. Biotechnol.* **2017**, *35*, 765; b) Z. Rong, M. Wang, Z. Hu, M. Stradner, S. Zhu, H. Kong, H. Yi, A. Goldrath, Y. G. Yang, Y. Xu, X. Fu, *Cell Stem Cell* **2014**, *14*, 121; c) T. Deuse, X. Hu, A. Gravina, D. Wang, G. Tediashvili, C. De, W. O. Thayer, A. Wahl, J. V. Garcia, H. Reichenspurner, M. M. Davis, L. L. Lanier, S. Schrepfer, *Nat. Biotechnol.* **2019**, *37*, 252; d) H. Xu, B. Wang, M. Ono, A. Kagita, K. Fujii, N. Sasakawa, T. Ueda, P. Gee, M. Nishikawa, M. Nomura, F. Kitaoka, T. Takahashi, K. Okita, Y. Yoshida, S. Kaneko, A. Hotta, *Cell Stem Cell* **2019**, *24*, 566.
- [38] H. H. Kuo, X. Gao, J. M. DeKeyser, K. A. Fetterman, E. A. Pinheiro, C. J. Weddle, H. Fonoudi, M. V. Orman, M. Romero-Tejeda, M. Jouni, M. Blancard, T. Magdy, C. L. Epting, A. L. George Jr., P. W. Burridge, *Stem Cell Rep.* **2020**, *14*, 256.
- [39] a) P. Y. Yam, S. Li, J. Wu, J. Hu, J. A. Zaia, J. K. Yee, *Mol. Ther.* **2002**, *5*, 479; b) D. L. DiGiusto, A. Krishnan, L. Li, H. Li, S. Li, A. Rao, S. Mi, P. Yam, S. Stinson, M. Kalos, J. Alvarnas, S. F. Lacey, J. K. Yee, M. Li, L. Couture, D. Hsu, S. J. Forman, J. J. Rossi, J. A. Zaia, *Sci. Transl. Med.* **2010**, *2*, 36ra43.
- [40] a) Q. Qu, G. Sun, W. Li, S. Yang, P. Ye, C. Zhao, R. T. Yu, F. H. Gage, R. M. Evans, Y. Shi, *Nat. Cell Biol.* **2010**, *12*, 31; b) Q. Cui, S. Yang, P. Ye, E. Tian, G. Sun, J. Zhou, G. Sun, X. Liu, C. Chen, K. Murai, C. Zhao, K. T. Azizian, L. Yang, C. Warden, X. Wu, M. D'Apuzzo, C. Brown, B. Badie, L. Peng, A. D. Riggs, J. J. Rossi, Y. Shi, *Nat. Commun.* **2016**, *7*, 10637; c) Y. Shi, C. D. Lie, P. Taupin, K. Nakashima, J. Ray, R. T. Yu, F. H. Gage, R. M. Evans, *Nature* **2004**, *427*, 78.
- [41] K. Qian, C. T. Huang, H. Chen, L. W. T. Blackburn, Y. Chen, J. Cao, L. Yao, C. Sauvey, Z. Du, S. C. Zhang, *Stem Cells* **2014**, *32*, 1230.
- [42] H. Li, R. Durbin, *Bioinformatics* **2009**, *25*, 1754.
- [43] A. McKenna, M. Hanna, E. Banks, A. Sivachenko, K. Cibulskis, A. Kernytzky, K. Garimella, D. Altshuler, S. Gabriel, M. Daly, M. A. Depristo, *Genome Res.* **2010**, *20*, 1297.
- [44] J. Grau, J. Boch, S. Posch, *Bioinformatics* **2013**, *29*, 2931.
- [45] A. Prokesch, H. J. Pelzmann, A. R. Pessentheiner, K. Huber, C. T. Madreiter-Sokolowski, A. Drougard, M. Schittmayer, D. Kolb, C. Magnes, G. Trausinger, W. F. Graier, R. Birner-Gruenberger, J. A. Pospisilik, J. G. Bogner-Strauss, *Sci. Rep.* **2016**, *6*, 23723.
- [46] S. Charrier, M. Ferrand, M. Zerbato, G. Précigout, A. Viorner, S. Bucher-Laurent, S. Benkhelifa-Ziyyat, O. W. Merten, J. Perea, A. Galy, **2011**, *18*, 479.
- [47] N. Uchida, K. Chen, M. Dohse, K. D. Hansen, J. Dean, J. R. Buser, A. Riddle, D. J. Beardsley, Y. Wan, X. Gong, T. Nguyen, B. J. Cummings, A. J. Anderson, S. J. Tamaki, A. Tsukamoto, I. L. Weissman, S. G. Matsumoto, L. S. Sherman, C. D. Kroenke, S. A. Back, *Sci. Transl. Med.* **2012**, *4*, 155ra136.
- [48] J. E. Le Belle, N. G. Harris, S. R. Williams, K. K. Bhakoo, *NMR Biomed.* **2002**, *15*, 37.
- [49] J. B. West, Z. Fu, T. J. Deerinck, M. R. Mackey, J. T. Obayashi, M. H. Ellisman, *Respir. Physiol. Neurobiol.* **2010**, *170*, 202.

# WJMSC-derived small extracellular vesicle enhance T cell suppression through PD-L1

Meizhang Li<sup>1</sup> | Rupal Soder<sup>2</sup> | Sunil Abhyankar<sup>2,3,4</sup> | Haitham Abdelhakim<sup>3</sup> | Mitchell W. Braun<sup>1</sup> | Camille V. Trinidad<sup>5</sup> | Harsh B. Pathak<sup>1,4</sup> | Ziyang Pessetto<sup>1</sup> | Clayton Deighan<sup>6</sup> | Siddhartha Ganguly<sup>3</sup> | Buddhadeb Dawn<sup>2,7</sup> | Joseph McGuirk<sup>3,4</sup> | Neil Dunavin<sup>3,8</sup> | Andrew K. Godwin<sup>1,4,5</sup>

<sup>1</sup> Department of Pathology and Laboratory Medicine, University of Kansas Medical Center, Kansas City, Kansas, USA

<sup>2</sup> Midwest Stem Cell Therapy Center, University of Kansas Medical Center, Kansas City, Kansas, USA

<sup>3</sup> Division of Hematologic Malignancies and Cellular Therapeutics, University of Kansas Medical Center, Kansas City, Kansas, USA

<sup>4</sup> The University of Kansas Cancer Center, University of Kansas Medical Center, Kansas City, Kansas, USA

<sup>5</sup> Department of Microbiology, Molecular Genetics and Immunology, Kansas City, Kansas, USA

<sup>6</sup> NanoView Biosciences, Boston, Massachusetts, USA

<sup>7</sup> Department of Medicine, University of Nevada, Las Vegas, Nevada, USA

<sup>8</sup> Division of Hematology and Blood and Marrow Transplant, University of California San Francisco, San Francisco, California, USA

## Correspondence

Andrew K. Godwin, University of Kansas Medical Center, 3901 Rainbow Blvd. 4019 Wahl Hall East, MS 3040, Kansas City, KS 66160, USA.  
Email: agodwin@kumc.edu

Neil Dunavin and Andrew K. Godwin Contributed equally.

## Funding information

NIGMS, Grant/Award Number: P20 GM130423; The University of Kansas Cancer Center Support, Grant/Award Number: P30 CA168524

## Abstract

Both mesenchymal stem cells (MSCs) and their corresponding small extracellular vesicles (sEVs, commonly referred to as exosomes) share similar immunomodulatory properties that are potentially beneficial for the treatment of acute graft versus host disease (aGvHD). We report that clinical grade Wharton's Jelly-derived MSCs (WJMSCs) secrete sEVs enriched in programmed death-ligand 1 (PD-L1), an essential ligand for an inhibitory immune checkpoint. A rapid increase in circulating sEV-associated PD-L1 was observed in patients with aGvHD and was directly associated with the infusion time of clinical grade WJMSCs. In addition, in vitro inhibitory antibody mediated blocking of sEV-associated PD-L1 restored T cell activation (TCA), suggesting a functional inhibitory role of sEVs-PD-L1. PD-L1-deficient sEVs isolated from WJMSCs following CRISPR-Cas9 gene editing fail to inhibit TCA. Furthermore, we found that PD-L1 is essential for WJMSC-derived sEVs to modulate T cell receptors (TCRs). Our study reveals an important mechanism by which therapeutic WJMSCs modulate TCR-mediated TCA through sEVs or sEV-carried immune checkpoints. In addition, our clinical data suggest that sEV-associated PD-L1 may be not only useful in predicting the outcomes from WJMSC clinical administration, but also in developing cell-independent therapy for aGvHD patients.

## KEYWORDS

acute graft-versus-host disease, PD-L1, small extracellular vesicles, T cell receptor, Wharton's Jelly-derived mesenchymal stem cells

## 1 | INTRODUCTION

Allogeneic hematopoietic cell transplantation (HCT) provides a potential cure for hematological malignancies, which depends in part on the immune graft-versus-leukemia (GvL) effects mediated by donor T cells (Chakraverty & Sykes, 2007; Ito & Shizuru, 1999). However, HCT may also cause the serious complication of immune acute graft-versus-host disease (aGvHD) due to donor

This is an open access article under the terms of the [Creative Commons Attribution](#) License, which permits use, distribution and reproduction in any medium, provided the original work is properly cited.

© 2021 The Authors. *Journal of Extracellular Vesicles* published by Wiley Periodicals, LLC on behalf of the International Society for Extracellular Vesicles

T cells recognizing and attacking the recipient's non-malignant tissues (Blazar et al., 2012; Ratanatharathorn et al., 2001; Zeiser & Blazar, 2017).

Programmed death ligand-1 (PD-L1) is a member of the B7 family, consisting of structurally related, cell-surface proteins that regulate T cell activation (TCA) and tolerance through the T cell receptor (TCR) (Greaves & Gribben, 2013). Depending on its interaction with either receptor PD-1 or CD80 expressed on the T cells, PD-L1 can function differently as either a coinhibitory or costimulatory checkpoint signal for the T cells (Butte et al., 2007; Butte et al., 2008; Freeman et al., 2000; Fumihiko Tsushima et al., 2007; Keir et al., 2007). It has been suggested that donor CD8<sup>+</sup> T cells expressing high levels of CD80 that leads in PD-L1/CD80 interaction in lymphoid tissue with subsequent CD8<sup>+</sup> T cell expansion to promote GvL effects (Cassady et al., 2018; Ni et al., 2017). However, in non-malignant target tissues, the binding of PD-L1 to PD-1 induces the anergy, exhaustion or apoptosis to establish donor's T cell tolerance and prevent GvHD (Cassady et al., 2018; Fujiwara et al., 2014; Kitazawa et al., 2007; Saha et al., 2016).

Mesenchymal stem cells (MSCs) have been widely applied to treat aGvHD (Dotoli et al., 2017; Kebriaei et al., 2020; Kurtzberg et al., 2020; Maziarz et al., 2015; Muroi et al., 2016), and one of their important mechanisms is their immunomodulatory effects related to PD-L1 (Ankrum et al., 2014; Pittenger et al., 2019; Shi et al., 2018). In GvHD patients, infused MSCs inhibit the cellular proliferation and activation of CD4<sup>+</sup> and CD8<sup>+</sup> T-cells through PD-L1-PD1 signalling (Zhang et al., 2020). The release of PD-L1 from MSCs is regulated by pro-inflammatory cytokines (Davies et al., 2017; Francisco et al., 2009; Guan et al., 2018) and is a pivotal 'licensing' step to maintain MSCs' immunomodulatory capabilities (Carvalho et al., 2019; Krampera, 2011). The role of secretory factors is crucial to explain the immunomodulatory function for MSCs from the bone marrow *in vivo*, given that MSCs migrate to the lungs and cannot reach systemic circulation in humans after infusion (Barbash et al., 2003; Eggenhofer et al., 2012).

Extracellular vesicles (EVs) represent a heterogeneous group of lipid bilayer membranous structures, which originate from the endosomal system (Van Niel et al., 2018). Small EVs (sEVs, also referred to as exosomes) usually have an average size between 30–150 nm. These sEVs can communicate with other cells and reshape surrounding microenvironments by transporting and delivering bioactive molecules (Barile & Vassalli, 2017). It has been demonstrated that tumour-associated exosomes suppress anti-tumour immune activities through inhibitory PD-L1-PD1 (Boussiotis, 2016; Daassi et al., 2020). For example, exosomal PD-L1 inhibit CD8<sup>+</sup> T cells activation associated with anti-PD1-PD-L1 therapy (Chen et al., 2018; Poggio et al., 2019; Ricklefs et al., 2018), and, if exosomal PD-L1 is suppressed, systemic anti-tumour immunity and memory will be recovered (Poggio et al., 2019; Ricklefs et al., 2018). Recent studies also have found that MSC-secreted exosomes inhibited the activation of CD4<sup>+</sup> and CD8<sup>+</sup> T cells (Fujii et al., 2018; Lai et al., 2018) and induced the differentiation of regulatory T cells (Ankrum et al., 2014; Dotoli et al., 2017; Maziarz et al., 2015; Muroi et al., 2016; Shi et al., 2018). Like tumoral exosomes, MSC-associated exosomes have been suggested to be an attractive therapeutic agent for the treatment of immune-mediated disorders through immunomodulation of T cell function (Gomzikova et al., 2019); however clinical trials have resulted in variable success and an optimal source of MSC has yet to be defined. Furthermore, there is currently no direct evidence for the intrinsic connection between MSC therapy and their associated exosomes, though MSC exosomes potentially contribute to the treatment of GvHDs (Fujii et al., 2018; Kordelas et al., 2014; Lai et al., 2018). For instance, a recent clinical study has shown that MSC-derived exosomes can effectively improve GvHD symptoms by reducing the pro-inflammatory cytokine response of donor PBMCs (Kordelas et al., 2014). However, their roles in regulating T cell function, specifically the profiling of checkpoint protein components on sEVs which underly the molecular mechanisms of sEV-mediated therapy, have not been extensively explored.

In this study, we determined that PD-L1 was enriched on the surface of WJMISC sEVs. The focus on WJMISC was based on the importance of maternal-fetal interface immune tolerance, extraembryonic fetal tissues, such as the umbilical cord, and our recent clinical study which assessed whether this was a superior tissue source of MSC to mediate immunomodulation in aGvHD (Soder et al., 2020). To support this clinical trial, we investigated the role of WJMISC sEV-PD-L1 on TCR-mediated TCA. We show that sEV-PD-L1 is necessary for the WJMISC-mediated blockage of TCR-mediated TCA. Mechanistically, membrane-bound PD-L1 provided by WJMISC-associated sEVs is required for the regulation of pZAP70-NFAT signalling pathway downstream of TCR. Finally, we show that increased circulation of sEV-PDL1 in aGvHD patients is associated with WJMISC infusion. Our work provides insight into the molecular mechanisms through which MSC-secreted PD-L1<sup>+</sup> sEVs target pathological immune cells related to aGvHD.

## 2 | RESULTS

### 2.1 | Identifying checkpoint PD-L1 on WJMISC-derived sEVs

Clinical grade WJMISCs (MSCTC-0010) were manufactured by the Midwest Stem Cell Therapy Center (MSCTC) at the University of Kansas Medical Center (KUMC). These cells were used in a phase I study (NCT03158896) designed to evaluate the safety of MSCTC-0010 in the treatment of *de novo* high risk acute or steroid refractory aGvHD (Soder et al., 2020). We demonstrated that WJMISCs express characteristic biomarkers such as CD90, CD105, and CD73 (Figure S1A) and maintain their multipotential under *in vitro* culture (Figure S1B). sEVs (30–150 nm size) were isolated from clinical grade WJMISCs using differential

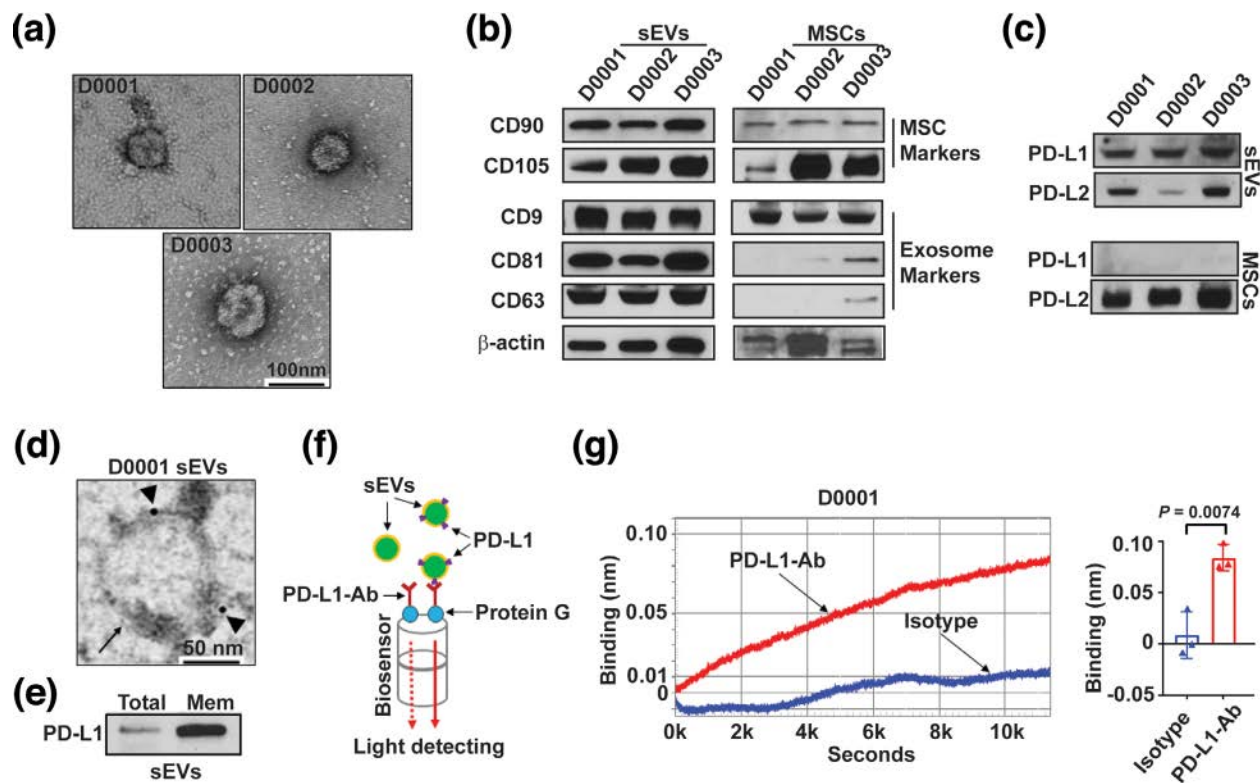


**FIGURE 1** PD-L1 is enriched on WJMSC-derived sEVs. (a) Representative TEM imaging of purified sEVs from three clinical grade human WJMSCs (D0001, D0002 and D0003). Scale bar, 100 nm. (b–c) Immunoblotting for stem cell biomarkers and exosome biomarkers (b), and checkpoint PD-L1 and PD-L2 (c) in purified WJMSC sEVs and the whole cell lysates (MSCs). All lanes were loaded with the same amount of protein. (d) A representative TEM image showing the immunogold-labelled PD-L1 signals (arrowheads) on the surface of a WJMSC sEV (arrow). Scale bar, 50 nm. (e) Immunoblotting for PD-L1 in the whole exosome lysates (Total) and exosomal membrane protein extracts (Mem). All lanes were loaded with the same amount of protein. (f) Schematic of optical biolayer interferometry (BLI) assay for detecting surface PD-L1 on the WJMSC sEVs. PD-L1-Ab, PD-L1 detection antibody. (g) A typical binding (left) between PD-L1-Ab and WJMSC sEVs (red curve) or between Isotype and WJMSC sEVs (blue curve) and quantification analysis based on their wavelength differences (right,  $n = 3$ ). Data are mean  $\pm$  s.e.m. and analysed by unpaired one-tailed Student's *t*-test

centrifugation (Figure S2A). Isolated WJMSC sEVs were characterized through Transmission Electron Microscopy (TEM, Figure 1a & Figure S2B) and Nanoparticle Tracking Analysis (NTA, Figure S2C). As expected, when compared with the cell lysate counterparts, WJMSC sEVs were enriched in conventional exosome-associated biomarkers (e.g., CD9, CD63, and CD81) and the stem cell biomarker CD90 as analysed by immunoblotting (Figure 1b).

PD-L1 was detected on the WJMSCs by flow cytometry (Figure S1C–D) and surface PD-L1 expression was confirmed on the WJMSC sEVs using immunogold TEM (Figure 1d). PD-L1 was consistently enriched in the membrane protein extract isolated from WJMSC-derived sEVs (Figure 1e). To confirm these findings, we used biolayer interferometry (BLI) assay to further detect and quantify surface PD-L1 on sEVs using an anti-human PD-L1 antibody (Figure 1f). A measurable binding was observed between WJMSC sEVs and the PD-L1 antibody (Figure 1g and Figure S3A–C), supporting that checkpoint PD-L1 was predominantly presented on the surface of WJMSC-derived sEVs. To determine whether PD-L1 was enriched on small EVs, we further applied qEVoriginal/70 nm columns (Izon Science, USA) to separate the exosomes from other EVs (Figure S3D–E). We found that PD-L1 was enriched on WJMSC-derived exosomes using our custom PD-L1/BLI assay (Figure S3F–G).

## 2.2 | WJMSC sEVs inhibit TCR-mediated TCA through PD-L1

MSC-derived exosomes have been suggested to regulate the activation and differentiation of T cells (Chen et al., 2016; Zhang et al., 2018; Zhang et al., 2018). We investigated how WJMSC sEVs might modulate the activation of T cells mediated by T cell receptor (TCR). CD3/CD28 Dynabeads were used to stimulate peripheral blood mononuclear cells (PBMCs) *in vitro*, and subsequently, TCR-mediated activation of CD4<sup>+</sup> T cells was indicated by *de novo* CD154 up-regulation (Figure S4A–C). Increased protein expression of PD1 was found on activated CD4<sup>+</sup> T cell surface (Figure S4D, F–G) and directly correlated with CD154 expression (Figure S4E). There was  $40 \pm 2.5$  % CD4<sup>+</sup> T cells co-expressed CD154 and PD1 ( $n = 6$ ) after stimulation with CD3/CD28 Dynabeads (Figure S4F).



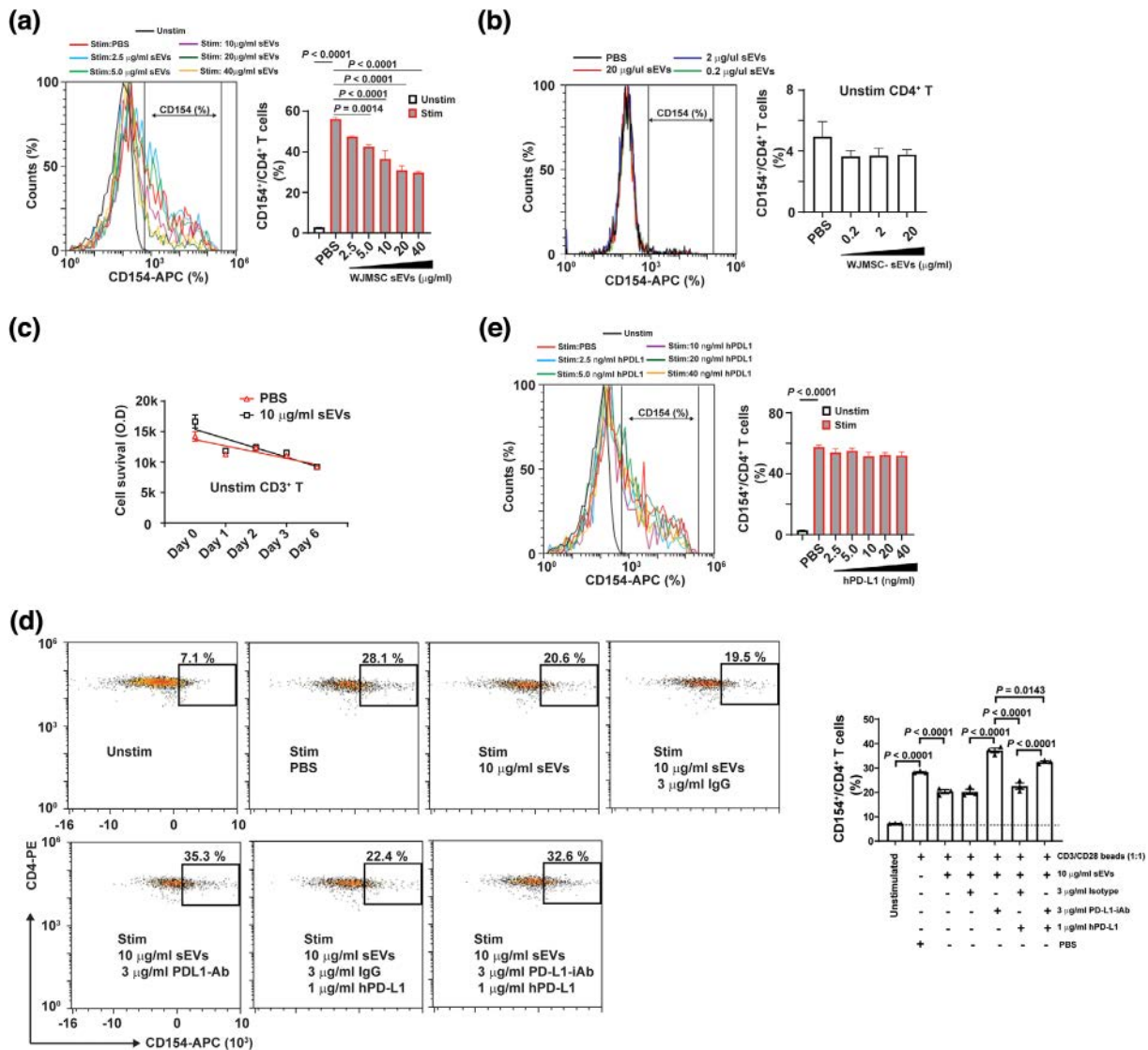


**FIGURE 2** WJMSC sEVs inhibit TCR-mediated CD4<sup>+</sup> TCA through PD-L1. (a) Flow cytometry showing the inhibitory effects of WJMSC-derived sEVs on CD4<sup>+</sup> T cell activation (CD154<sup>+</sup>) in a dose-dependent manner (left) and quantitative analysis (right). (b) Effects of WJMSC sEVs on unstimulated CD4<sup>+</sup> T cells (left) and quantitative analysis (right), measured by flow cytometry. (c) Survival of unstimulated CD3<sup>+</sup> T cells treated with PBS or 10 μg/ml WJMSC sEVs for 6 days. (d) Representative flow charts (left) and quantitative analysis (right) of activated CD4<sup>+</sup> T cells incubated with 10 μg/ml WJMSC sEVs, 3 μg/ml PD-L1-IgG, or 1 μg/ml hPD-L1 for overnight. (e) Flow cytometry showing the effects of soluble hPD-L1 on activated CD4<sup>+</sup> T cells (left) and quantitative analysis (right). Peripheral blood mononuclear cell (PBMC)s were stimulated with (Unstim) or without (Stim) CD3/CD28 Dynabead at a dilution of 1:1 ratio (a,d,e). hPD-L1, recombinant human PD-L1 (d,e). PD-L1-IgG, neutralization antibody for human PD-L1 (d). Data are mean ± s.e.m ( $n = 3$ ) and analysed by one-way ANOVA (a,b,d,e). Experiments independently repeated three times (a,d,e)

Next, we asked whether WJMSC-derived sEVs affected the activation of CD4<sup>+</sup> T cells stimulated by CD3/CD28 Dynabeads. We found that WJMSC sEVs significantly inhibited TCR-mediated CD4<sup>+</sup> T cell activation (TCA) in a dose-dependent manner (Figure 2a). Normalized with the PBS, we found less expression of CD154 on CD4<sup>+</sup> T cells  $15 \pm 1.2 \sim 47 \pm 0.8\%$  ( $n = 3$ ) after treating with 1.25~20 μg/ml WJMSC sEVs for overnight. However, WJMSC sEVs were not able to either activate naïve CD4<sup>+</sup> T cells (Figure 2b) or enhance their survival (Figure 2c). To confirm this observation, we investigated the effects of WJMSC-derived sEVs on TCR-mediated CD8<sup>+</sup> TCA (Figure S5A–B). Consistently, we found that WJMSC sEVs significantly ( $P < 0.05$ ) inhibited the activation of CD8<sup>+</sup> T cells (IFN- $\gamma$ <sup>+</sup>) stimulated by PepTivator cytomegalovirus (CMV) pp65 peptide (Figure S5C).

Exosomal PD-L1 is critical for tumour cells to evade immune attack through coinhibitory regulation mechanisms related to the TCRs (Chen et al., 2018; Ricklefs et al., 2018). Because PD-L1 was also enriched on the WJMSC-derived sEVs, we asked whether WJMSC sEV-PD-L1 molecularly regulates TCR-mediated CD4<sup>+</sup> TCA. After treatment with 10 μg/ml sEVs overnight, TCR-mediated TCA was reduced by  $28 \pm 6\%$  ( $n = 3$ ,  $P < 0.0001$ ), and pre-incubating sEVs with 3 mg/ml neutralization antibody can eliminate their inhibitory effects (Figure 2d). This loss of inhibition can be partially rescued by the addition of soluble human recombinant hPD-L1 protein. However, we did not observe the direct effect of recombinant PD-L1 on the activated CD4<sup>+</sup> T

cells (Figure 2e). Our results support that WJMSC-derived sEVs inhibit TCA by modulating TCR and that PD-L1 is involved in sEV-mediated immunosuppression.

### 2.3 | Genetic disruption of PD-L1 impairs WJMSC sEVs' capability to inhibit TCR-mediated TCA

To confirm the above observation, we generated PD-L1 knockout (KO) WJMSCs by genetically deleting “-CAGC-” in the 3<sup>rd</sup>-Exon through gene editing (Figure S6A). Loss of PD-L1 protein in the *PD-L1*<sup>-/-</sup> WJMSCs was verified by immunoblotting (Figure S6B) and flow cytometry (Figure S6C). These cells demonstrated the same normal phenotype as their wild types (Figure S6C-D) and were not capable of expressing PD-L1 after IFN- $\gamma$  treatment (Figure S6D-E and Figure S7). The immune inhibitory effects of *PD-L1*<sup>-/-</sup> WJMSCs on CD4<sup>+</sup> TCA were further tested. We found *PD-L1*<sup>-/-</sup> WJMSCs failed to block the CD4<sup>+</sup> TCA compared with the WT WJMSCs by means of CD154 expression by flow cytometry (Figure 3a). Consistently, we found that expression of PD1 on activated CD4<sup>+</sup> T cells was decreased by  $58 \pm 3\%$  ( $n = 3$ ,  $P < 0.0001$ ) after treated with WT WJMSCs. Compared with

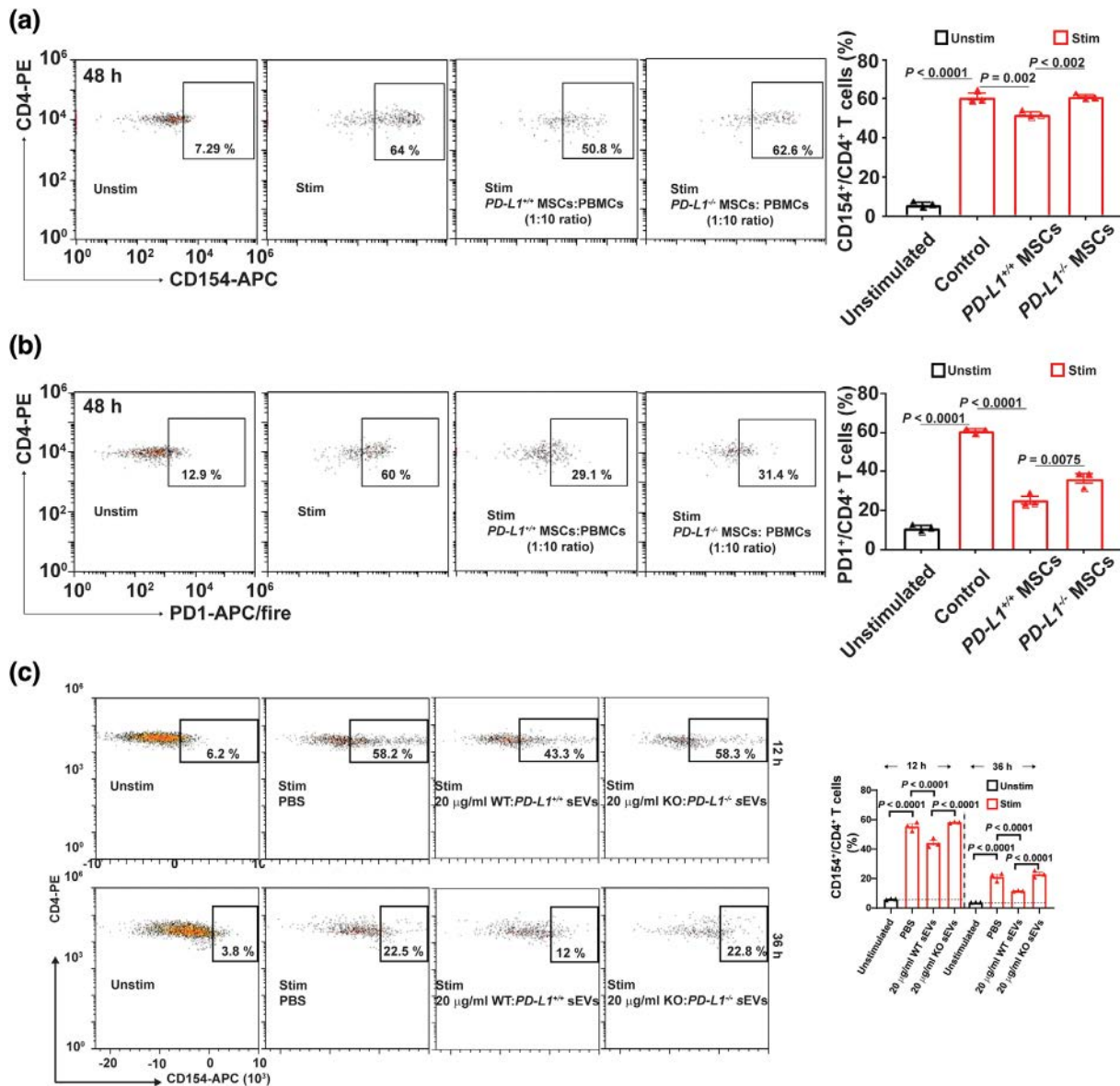


**FIGURE 3** Both WJMSCs and sEVs decrease their capability to block TCR-mediated TCA after PD-L1 knockout. (a) Flow cytometry showing the 48-hour inhibitory effects of both WT and KO WJMSCs on CD4<sup>+</sup> T cell activation (left) and quantitative analysis (right). (b) Expression of PD1 on the CD4<sup>+</sup> T cells mentioned above, measured by flow cytometry (left) and quantitation (right). (c) Representative flow charts (left) and quantitative analysis (right) of activated CD4<sup>+</sup> T cells incubated with 20 µg/ml PD-L1 WT or KO WJMSC sEVs for 12 h or 36 h. PBMCs were stimulated with (Unstim) or without (Stim) CD3/CD28 Dynabead at a dilution of 1:1 ratio (a-c) and the ratio of WJMSCs to PBMCs was 1 to 10 (a,b). Data are mean  $\pm$  s.e.m. ( $n = 3$ ) and analysed by one-way ANOVA (a-c). Data are representative of three independent experiments (a-c)

the WT WJMSCs, expression of PD1 on activated CD4<sup>+</sup> T cells was decreased by  $28.6 \pm 11\%$  ( $n = 3$ ,  $P < 0.0001$ ) after treated with PD-L1<sup>-/-</sup> WJMSCs (Figure 3b).

Next, sEVs were purified from PD-L1<sup>-/-</sup> WJMSCs, and the loss of PD-L1 on their corresponding sEVs was verified by immunoblotting (Figure S8A), TEM (Figure S8B), and BLI (Figure S8C). PD-L1-deficient sEVs demonstrate similar levels of the exo-proteins, for example, CD81, PD-L2, HSP70 (Figure S8A & F), morphology (Figure S8B & E), particle yield (Figure S8D) and average sizes (Figure S8D-E) as their wild type counterparts. These sEVs were not induced by IFN- $\gamma$  to release PD-L1 (Figure S8F-G). Like WJMSCs, we show that PD-L1-deficient WJMSC sEVs significantly lost their capability to inhibit CD3/CD28 Dynabead-stimulated CD4<sup>+</sup> TCA (Figure 3c). Our results suggest that PD-L1 carried by WJMSC sEVs are required for WJMSCs to inhibit TCR-mediated TCA.

## 2.4 | PD-L1 carried by WJMSC sEVs is essential for modulating TCR's functions

To determine whether WJMSC sEVs modulate the TCR signaling pathway through PD-L1, we examined the protein level of phosphorylated zeta-chain-associated protein kinase 70 (pZAP70), a partner protein that is associated with activated TCRs, in T cells (Boussiotis, 2016; Gaud et al., 2018). In the activated CD4<sup>+</sup> T cells (Figure 4a), we found that expression of pZAP70 was increased by  $60 \pm 10\%$  ( $n = 3$ ,  $P = 0.014$ ) compared with the unstimulated CD4<sup>+</sup> T cells (Figure 4b). Treating them with wild type WJMSC sEVs significantly decreased the pZAP70's expression by  $89 \pm 11\%$  ( $n = 3$ ,  $P < 0.0001$ ) in the activated CD4<sup>+</sup> T cells. However, treating them with PD-L1-deficient WJMSC sEVs only decreased the pZAP70's expression by  $16 \pm 5\%$  ( $n = 3$ ,

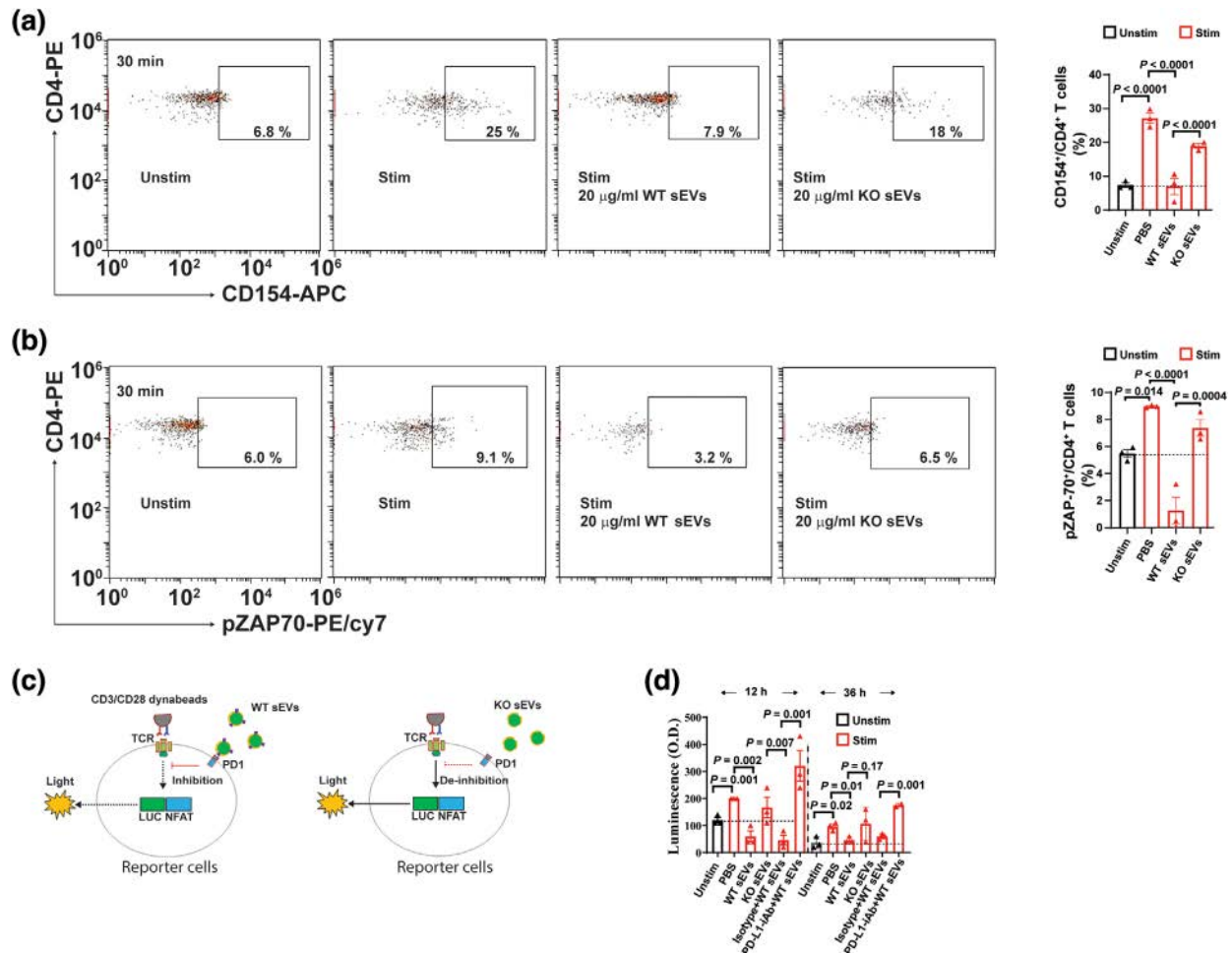


**FIGURE 4** PD-L1 is required for WJMSC sEVs to modulate TCR signalling pathway. (a) Representative flow charts showing the activation of CD4<sup>+</sup> T cells incubated with 20  $\mu$ g/ml PD-L1 WT or KO WJMSC sEVs for 20 min (left) and quantitative analysis (right). (b) Expression of phospho-ZAP70 protein (pZAP70) in activated CD4<sup>+</sup> T cells mentioned above, measured by flow cytometry (left) and quantitation (right). (c) Schematic of PD1-NFAT reporting system in Jurkat T cells stimulated with 1:1 ratio CD3/CD28 Dynabeads and co-incubated with 20  $\mu$ g/ml PD-L1 WT and KO WJMSC sEVs plus 3  $\mu$ g/ml PD-L1-iAb/isotype for 12 h or 36 h. LUCNFAT, luciferase gene under the control of NFAT response elements; PD-L1-iAb, neutralization antibody for human PD-L1. (d) Quantitative analysis from c ( $n = 3$ ). Data are mean  $\pm$  s.e.m and analysed by one-way ANOVA (a,b,d)

$P = 0.054$ ) in the activated CD4<sup>+</sup> T cells. Our results suggest that PD-L1 carried by sEVs is critical for WJMSCs to inhibit CD4<sup>+</sup> TCA through TCR.

Phosphorylation of ZAP70 protein induced its downstream nuclear translocation of nuclear factor of activated T cells (NFAT), signalling pathways through Ca<sup>2+</sup>-calcineurin (Boussiotis, 2016; Gaud et al., 2018). To determine whether WJMSC sEVs modulate this signalling pathway downstream of TCR, we examined their effect on Jurkat T cells that were engineered with a PD1-NFAT-luciferase reporter (Figure 4c). PD1-NFAT reporter-Jurkat cells were stimulated by CD3/CD28 Dynabeads (1:1 ratio) for 12 h and NFAT luciferase reporter activity was significantly increased by  $69 \pm 13\%$  ( $n = 3$ ,  $P = 0.001$ ) compared with unstimulated reporter Jurkat cells (Figure 4d). Our results suggest that reporter-Jurkat cells can be directly activated by CD3/CD28 Dynabeads and activation of NFAT signalling pathways is directly related to the stimulation of TCR. Next, we found that treating them with 20  $\mu\text{g/ml}$  WT WJMSC sEVs significantly decreased the NFAT luciferase reporter activity by  $70 \pm 10\%$  ( $n = 3$ ,  $P = 0.002$ ) in activated reporter-Jurkat cells which could be reversed by neutralizing anti-PD-L1 antibody (Figure 4d). PD-L1<sup>-/-</sup> WJMSCs derived sEVs did not cause inhibition of the activation of reporter-Jurkat cells (Figure 4d). Similar results were obtained through stimulating and treating reporter-Jurkat cells for 36 h. Our results support the concept that WJMSC sEVs modulate TCR function and regulate its downstream signalling pathway mainly through PD-L1.

## 2.5 | Increased plasma sEVs is associated with WJMSC infusion in aGvHD patients

To address whether WJMSCs might provide patients therapeutic benefit via sEV-associated PD-L1, we first applied BLI to examine the levels of sEV-PD-L1 in plasma samples from aGvHD patients infused with WJMSCs in a clinical trial at our center (Figure 5a). Compared to the baseline (pre-dose) plasma level, the level of plasma sEV-PD-L1 was significantly increased (by 50%,  $P < 0.01$ ) 30 min after WJMSC infusion (Figure 5b). A time-dependent decline of plasma sEV-PD-L1 levels was observed at additional longitudinal screening points (from 1 to 8 h post infusion). Nevertheless, the circulating sEV-PD-L1 levels remained elevated when compared to the baseline level. In addition, we observed that multiple infusions (Figure 5c,d) and higher cell dosage (Figure 5e,f) more efficiently increased and maintained plasma levels of sEV-PD-L1 in aGvHD patients.

Next, we used ExoView™ chips (NanoView Bioscience, USA) to enumerate the quantity and population subtypes of sEVs in the plasma from these patients (Figure S9A). We found that total and CD81<sup>+</sup> circulating sEVs captured by the CD81 antibody appeared significantly increased 1 h after WJMSC administration (Figure S9B-C). Similar results were obtained from CD63- or CD9-capture spots (Figure S9B & D-E). All sEV subpopulations, including CD63<sup>+</sup>CD81<sup>+</sup>, CD63<sup>+</sup>CD9<sup>+</sup>, and CD9<sup>+</sup>CD81<sup>+</sup>, were observed to be significantly increased post-infusion (Figure S9C-F). Therefore, our results show that both increased circulation of sEVs and up-regulation of sEV-PD-L1 are associated with WJMSC infusion in aGvHD patients. These findings suggest that WJMSC-mediated immunomodulatory effects are related to increasing sEV-PD-L1 levels. Extending on recent studies indicating an immunomodulatory role of MSC-derived exosomes in preventing GvHD (Kordelas et al., 2014; Lai et al., 2018), our results suggest for the first time that sEV-PD-L1 may represent a mediator of WJMSC immunosuppressive properties.

## 2.6 | WJMSCs infusion demonstrated clinical responses in patients with advanced aGvHD

In the clinical trial (NCT03158896), 70% of patients with advanced aGvHD had an overall response including 40% of patients with a complete response thought to be attributable to MSCTC-0010 infusions. This therapy was associated with median overall > 1 year in this high-risk cohort (Soder et al., 2020). Patients on this trial did not show significant toxicities associated with treatment (Soder et al., 2020). To evaluate the potential therapeutic effects of WJMSCs in patients with aGvHD, we examined the plasma levels of two prognostic aGvHD biomarkers, that is, suppression of tumorigenicity 2 (ST2) and regenerating islet-derived 3 alpha (REG3 alpha or REG3A) in plasma samples from patients with aGvHD (Dunavin et al., 2019; Levine et al., 2012; Lugt et al., 2013; Ponce et al., 2015; Rowan et al., 2020; Te Boome et al., 2015). We observed decreased plasma levels for both ST2 and REG3A (Figure 6a). Prior to WJMSC infusion (Day 1), the mean plasma ST2 level in aGvHD was 80 ng/ml. One week after the 2<sup>nd</sup> WJMSC infusion (Day 14 from first infusion), we found that the mean plasma ST2 level in aGvHD patients decreased to 74 ng/ml,  $P < 0.05$  (Figure A6, left). At post infusion day 21 and day 28, the mean plasma ST2 level decreased to 72 ng/ml ( $P < 0.05$ ) and 64 ng/ml ( $P < 0.005$ ), respectively. Consistently, we found that mean plasma REG3A levels decreased at days 7 (44.5 ng/ml,  $P < 0.05$ ), 14 (42.7 ng/ml,  $P < 0.05$ ) and 21 (44.6 ng/ml,  $P < 0.01$ ) post WJMSCs infusion in aGvHD patients compared to pre-infusion (57.8 ng/ml) (Figure 6b).

## 2.7 | IFN- $\gamma$ induced the release of sEV-PD-L1 from WJMSCs

Interferon- $\gamma$  (IFN- $\gamma$ ) can promote MSCs to secrete soluble PD-L1 (Carvalho et al., 2019; Davies et al., 2017; Francisco et al., 2009; Guan et al., 2018; Krampera, 2011) and enhance the release of exosome-associated PD-L1 in other cell types (Chen et al., 2018;



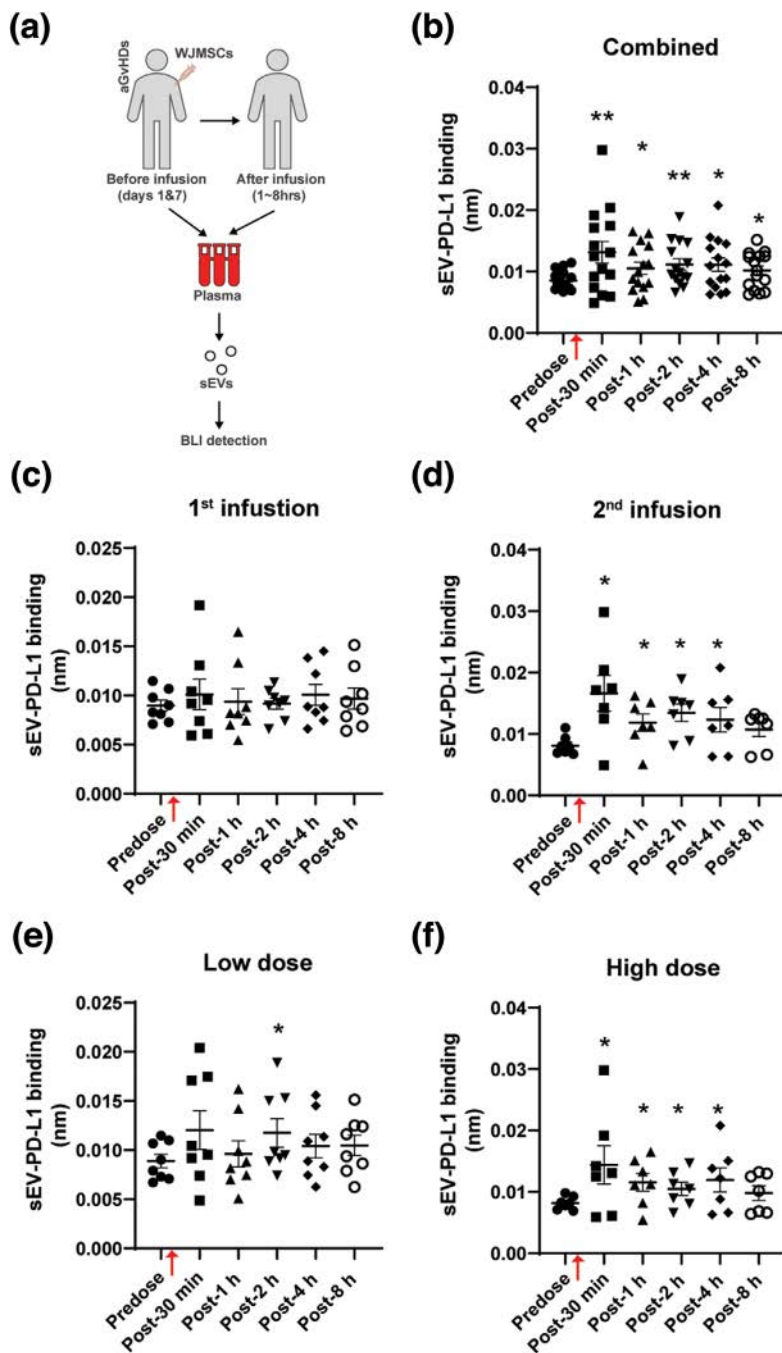


**FIGURE 5** Clinical WJMSC infusion increases plasma sEV-PD-L1 in aGvHD patients. (a) Schematic of measuring plasma sEV-PD-L1 in aGvHD patients clinically received WJMSCs. Patients' plasma samples were collected before (predose) and after (post) WJMSC transplantation within 8 h, sEVs were isolated from these plasma samples, and PD-L1 on sEVs was examined by BLI. (b-f) Quantitative analysis for combined patients (b,  $n = 15$ ) and partial patients received with either 1<sup>st</sup> infusion (c,  $n = 8$ ), 2<sup>nd</sup> infusion (d,  $n = 7$ ), low dose:  $1.2 \times 10^6$  cells/kg (e,  $n = 8$ ), or high dose:  $10 \times 10^6$  cells/kg (f,  $n = 7$ ). WJMSC infusion time points were indicated by red arrows (b-f). Data are mean  $\pm$  s.e.m. and analysed by unpaired one-tailed Student's t-test (b-f). \* $P < 0.05$ , \*\* $P < 0.01$ , \*\*\* $P < 0.005$

Ricklefs et al., 2018). To explore whether increased circulating sEV-PD-L1 was related to patient plasma IFN- $\gamma$  levels, we first examined the levels of plasma IFN- $\gamma$  in aGvHD patients. We observed that the systemic IFN- $\gamma$  concentration in aGvHD patients was significantly higher (increased by 69%,  $P < 0.005$ ) compared with healthy individuals (Figure 7a). In addition, we noticed that WJMSC infusion did not affect patients' plasma IFN- $\gamma$  levels. Second, consistent with previous findings (Carvalho et al., 2019; Davies et al., 2017), we observed that IFN- $\gamma$  significantly up-regulated expression of cell surface protein (Figure 7b) and mRNA (Figure 7c) of PD-L1 in WJMSCs in vitro. Consistent with these observations, we found that PD-L1 concentration increased by 4.5-fold ( $n = 3$ ,  $P < 0.001$ ) in the culture medium from IFN- $\gamma$ -treated WJMSCs (Figure 7d). To determine whether IFN- $\gamma$  can potential induced soluble PD-L1 from WJMSC infusions, we examined the level of PD-L1 protein in complete/unfiltered (Exo<sup>+</sup>) conditioned medium and exosome-depleted (Exo<sup>-</sup>) conditioned medium (Figure 7e). Approximately  $3.8 \pm 1.56$  ng/ml PD-L1 in the untreated culture and  $3.1 \pm 2.0$  ng/ml PD-L1 in the IFN- $\gamma$ -treated culture was detected in exosome-free conditional medium. This finding suggests that IFN- $\gamma$  cannot directly enhance WJMSCs to secrete soluble PD-L1.

Third, we sought to determine the fraction of membrane-bound PDL1 carried by the sEVs to total PDL1 protein in aGvHD patients' plasma post WJMSCs infusion. To address this question, we compared the levels of PD-L1 in the total versus

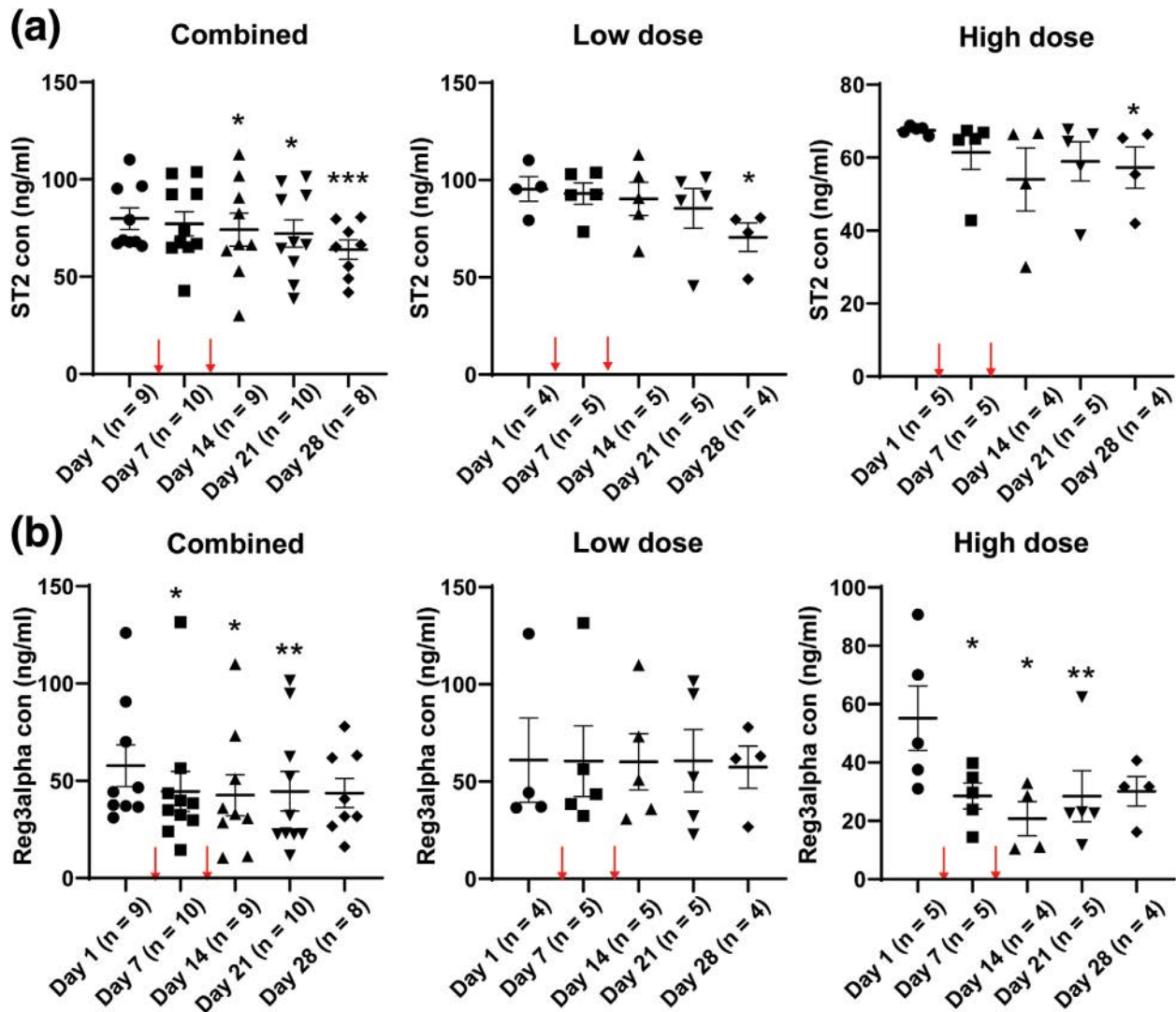


**FIGURE 6** Decreased plasma ST2 and REG3A levels in aGvHD patients with WJMSC infusion. (a,b) ELISA of ST2 (a) and REG3A (b) in the plasma samples from aGvHD patients with the WJMSC infusion. Left, combined analysis; Middle, low-dose ( $1.2 \times 10^6$ /kg WJMSCs); Right, high-dose ( $10 \times 10^6$ /kg WJMSCs). Two cell infusion time points were indicated by red arrows (a,b). Data are mean  $\pm$  s.e.m. and analysed by unpaired one-tailed Student's t-test (a,b). \* $P < 0.05$ , \*\* $P < 0.01$ , \*\*\* $P < 0.005$

EV-depleted plasma samples. About  $19 \pm 6$  pg/ml PD-L1 ( $P = 0.0045$ ) was detected in the unfiltered plasma, but only  $0.02 \pm 0.009$  pg/ml in the exosome-free plasma generated by Ultracentrifugation (Figure 7f). Consistently, significantly lower levels of PD-L1 were detected in exosome-depleted plasma compared to complete/unfiltered plasma (Figure 7g). These findings suggest that a majority of circulating PD-L1 in the plasma was sEV membrane-bound and was not soluble. Indeed, WJMSC sEV-PD-L1 were able to be directly detected by ELISA (Figure 7h). Our results indicated that exposing WJMSCs to the pro-inflammatory cytokine IFN- $\gamma$  may be an initial step to induce the release of immunosuppressive sEV-PD-L1 after WJMSC infusion in vivo.

## 2.8 | Binding of WJMSC sEVs to the peripheral blood cells in vivo

A decline in circulating sEV-PD-L1 at later timepoints was observed in patients (Figure 5a). IFN- $\gamma$  remained constant in aGvHD patients after WJMSC infusion (Figure 7a), and one possibility might be the direct uptake of sEVs by peripheral blood cells. To address this possibility, we intravenously administrated WJMSC sEVs to immunodeficient NOD SCID gamma (NSG) mice (Figure 8a,i) and measured the presence of human PD-L1 (hPD-L1) on the surface of mouse peripheral blood cells by flow cytometry (Figure 8b). Twelve hours after WJMSC sEV injection, about  $8.2 \pm 2.0\%$  of the mouse PBMCs and  $10.8 \pm 1.6\%$  of the mouse CD3<sup>+</sup> T cells appeared positive for hPD-L1 (Figure 8c). Even though an unavoidable low (background) level of  $2.0 \pm 0.31\%$  PBMCs and  $3.0 \pm 0.06\%$  CD3<sup>+</sup> T cells was detected, our results suggested that binding and subsequent uptake of human

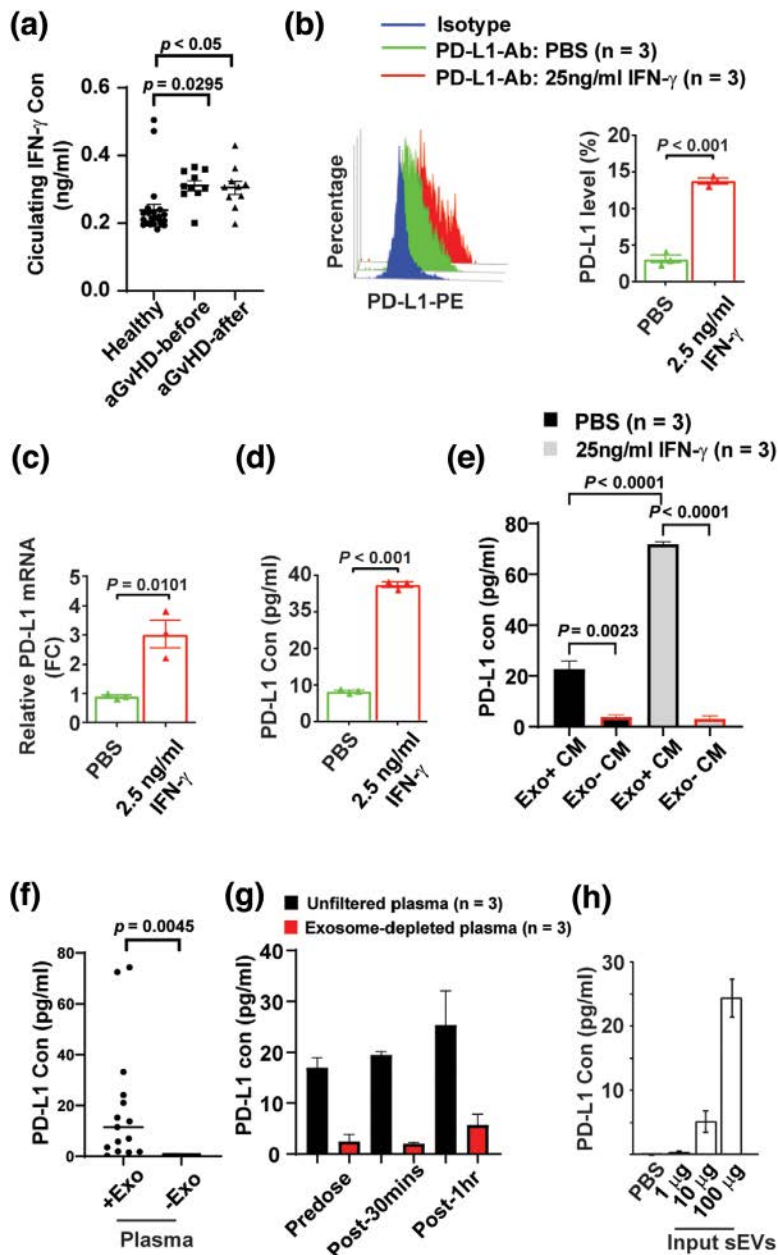


**FIGURE 7** IFN- $\gamma$  induces the sEV-PD-L1 release from WJMSCs. (a) Quantitation of IFN- $\gamma$  in the plasma samples of healthy donors ( $n = 23$ ) and aGvHD patients ( $n = 10$ ) before or after WJMSC infusion, measured by ELISA. (b) Flow cytometry of PD-L1 protein on the WJMSCs induced by 2.5 ng/ml IFN- $\gamma$  (left) and quantitative analysis (right,  $n = 3$ ). (c) Quantitation of PD-L1 mRNA in the WJMSCs from b ( $n = 3$ ). (d), ELISA of PD-L1 secreted from the WJMSC from b ( $n = 3$ ). (e) PD-L1 in both complete conditioned medium (Exo+ CM) and exosome-depleted conditional medium (Exo- CM) from WJMSCs licensed by IFN- $\gamma$  ( $n = 3$ ). (f,g) Quantitation of PD-L1 in unfiltered or exosome-depleted human plasma samples. Exosome-free human plasma was generated by either ultracentrifugation (F,  $n = 3$ ) or Amicon Ultra-4 centrifugal filters ( $n = 3$ ). (h) ELISA of PD-L1 on WJMSC-derived sEVs ( $n = 15$ ). Data are mean  $\pm$  s.e.m. and analysed by unpaired one-tailed Student's *t*-test (a-h)

sEVs by mouse blood cells might be a major reason why hPD-L1 was detectable on mouse cells. We further measured the levels of human PD-L1 on the isolated sEVs from mouse plasma samples by BLI. For WJMSC sEV-injected mice, we found a two-fold increase ( $P = 0.011$ ) of human PD-L1 on isolated mouse sEVs compared with PBS-injected mice (Figure 8d). Within 1–4 h after sEV injection, a higher percentage of hPD-L1-positive mouse PBMCs ( $42 \pm 2.7\% \sim 48 \pm 2.2\%$ ) and CD3<sup>+</sup> T cells ( $38 \pm 2.6\% \sim 42 \pm 2.01\%$ ) were detected (Figure 8e). To confirm this uptake, biotin-labelled WJMSC sEVs were injected into NSG mice (Figure 8a,ii) and similar elevated levels of biotin positive PBMCs ( $13 \pm 6.3\% \sim 43 \pm 6.3\%$ ) and CD3<sup>+</sup> T cells ( $22.6 \pm 3.2\% \sim 30 \pm 1.4\%$ ) were observed (Figure 8f). In addition to inflammatory environment exposure, our results suggest that direct uptake of sEVs by peripheral blood cells may likely influence circulating sEV-PD-L1 levels.

### 3 | DISCUSSION

Steroid refractory aGvHD is a major cause of mortality in patients receiving HCT. While the immunomodulatory characteristics of MSCs represent a potential effective therapy with minimal toxicity, the exact mechanisms for their therapeutic function in vivo have been elusive. Gaining insight into the specific contribution of sEVs to WJMSCs clinical effects provides opportunities for enhanced cellular-based therapeutics in patients with aGvHD. We demonstrate for the first time that WJMSCs secrete

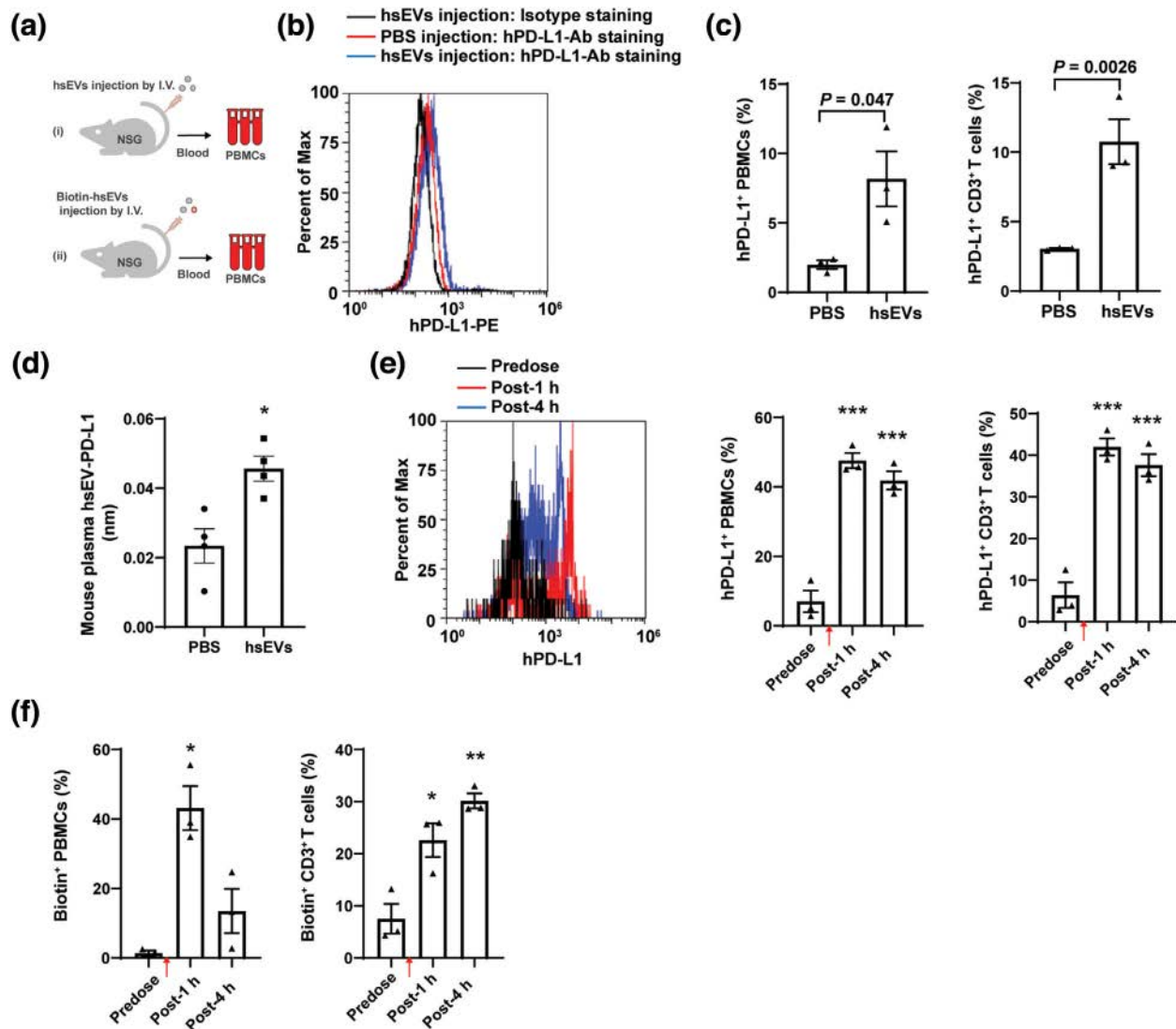


**FIGURE 8** In vivo binding of human WJMSC sEVs on mouse PBMCs. (a) Schematic of intravenously administrating 4 mg/kg sEVs (i) or Biotin-labelled sEVs (ii) to immunodeficient NOD scid gamma (NSG) mice. (b) Flow cytometry of human PD-L1 on the cell surface of PBMCs from NSG mice administrated by PBS or sEVs for 12 h. (c) Quantitation of human PD-L1 on mouse PBMCs (left,  $n = 3$ ) and CD3+ T cells (right,  $n = 3$ ) from b. (d) Quantitative analysis of human sEV-PD-L1 in mouse plasma samples from b ( $n = 4$ ). (e) Flow cytometry showing human PD-L1 on mouse PBMCs from NSG mice before and after WJMSC sEV injection (left) and quantitation (right,  $n = 3$ ). (f) Quantitative analysis of biotin labelled WJMSC sEVs (Biotin<sup>+</sup>) on mouse PBMCs (left,  $n = 3$ ) and CD3+ T cells (right,  $n = 3$ ), measured by flow cytometry. Human WJMSC sEVs infusion time points were indicated by red arrows (d,e). Data are mean  $\pm$  s.e.m. and analysed by unpaired one-tailed Student's t-test (c-f). \* $P < 0.05$ , \*\* $P < 0.01$ , \*\*\* $P < 0.005$

immunosuppressive sEVs after being infused into aGvHD patients and subsequently target the immune cells via enhancing T cell suppression. We identified PD-L1, an inhibitory checkpoint protein expressed on MSCs (Carvalho et al., 2019; Krampera, 2011) and involved in their immunomodulation (Davies et al., 2017; Francisco et al., 2009; Guan et al., 2018), as specifically enriched in WJMSC-derived sEVs. Our study reveals a role of sEV-carried PD-L1 for WJMSC-based therapy in aGvHD patients.

A role for MSC-derived sEVs in T cell regulation has been suggested in various settings (Fujii et al., 2018; Ha et al., 2020; Lai et al., 2018; Zhang et al., 2018; Zhang et al., 2018), mainly in the production and differentiation of T helper cells (Fujii et al., 2018; Lai et al., 2018) and regulatory T cells (Lai et al., 2018; Zhang et al., 2018; Zhang et al., 2018). We report that the inhibitory PDL1 checkpoint is enriched on WJMSC-derived sEVs, thus suggesting these sEVs might regulate the functions of T cell receptors (TCR) responsible for recognizing antigen peptides. Indeed, we show that WJMSC sEVs effectively inhibit both CD4<sup>+</sup> and CD8<sup>+</sup> T cell activation that is mediated by TCR signalling pathway. sEVs only demonstrate their immunosuppressive capability without stimulating the activation or enhancing the proliferation of naïve T cells. Consistent to previous studies (Chen et al., 2016; Fujii et al., 2018), our studies support that sEVs' functions, exerted on the TCRs, primarily rely on indirectly modulatory regulation rather than the direct antigen presentation.



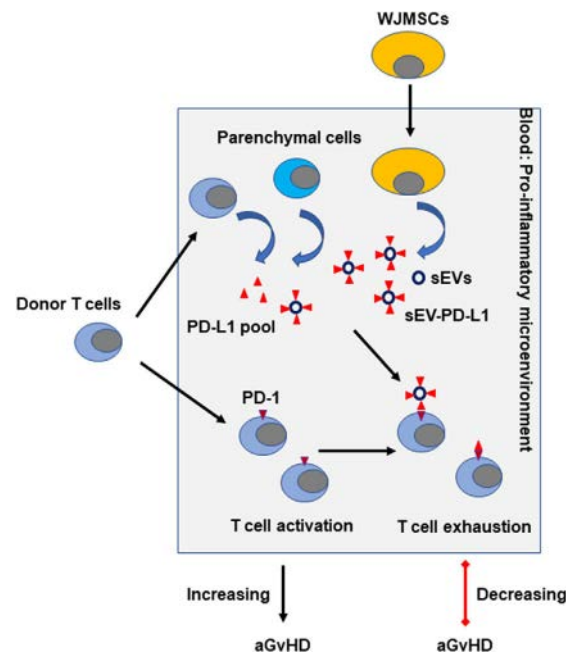


**FIGURE 9** Summary of WJMSCs' contribution to circulation PD-L1 pool through secreting sEVs in aGvHD patients. Transplanted WJMSCs are induced by IFN- $\gamma$  and enhance the release of sEV-carried PD-L1 in the blood. Membrane-bound sEV-PD-L1 interacts the PD1 on the T cells and modulate the TCR-mediated TCA associated with aGvHD

We show that PD1, the receptor for PD-L1, is up-regulated on the activated CD4<sup>+</sup> T cells, underscoring the roles of PD-L1-PD1 axis in sEV-related immunomodulation. Blockage of PD-L1 on the WJMSC sEVs through neutralizing antibodies impairs their inhibitory ability for TCA. Consistently, PD-L1-deficient sEVs from PD-L1 null WJMSCs failed to block the TCA, supporting that sEVs inhibit T cell activation via sEV-carried checkpoint PD-L1. Furthermore, sEV-PD-L1 is essential for the phosphorylation of pZAP70, an important partner protein associated with the activated TCR and its subsequent induction of downstream signalling pathways. Our study suggests that WJMSC-derived sEVs inhibit T cell activation or enhance T cell suppression through membrane-carried inhibitory checkpoints.

While MSC therapy faces challenges from either resources or the standard definition of MSCs (Brown et al., 2019; Galipeau & Sensébé, 2018), sEVs have significant potential as a novel alternative to whole cell therapies because of the low toxicity and ease of storage (Galipeau & Sensébé, 2018). In aGvHD patient with WJMSC infusion, we demonstrate that a rapidly increasing plasma sEV-PD-L1 following infusion. Exposing WJMSCs to IFN- $\gamma$  seems critical to release sEV-PD-L1 from their parental cells. Secreted sEV-PD-L1 can quickly target the peripheral blood cells through direct uptake of sEVs. Remarkably, we show that increased sEV-PD-L1 in patients' plasma samples is associated with improved GvHD after clinical WJMSC infusion, suggesting that sEV-PD-L1 is an important mechanism explaining the efficacy of WJMSC in aGvHD patients.

Taken together, our findings suggest that infused WJMSCs can significantly contribute to the circulation "PD-L1 pool" by quickly secreting sEVs (Figure 9) and may represent the fundamental mechanism underlying WJMSC-based therapies. We also showed that sEV-associated PD-L1, rather than its soluble form, mainly contributes to the inducible "PD-L1 pool" though endogenous soluble PD-L1 is detected in patients. A more detailed characterization of the effects of sEV-PD-L1 on T cells should shed light on the contribution of therapeutic exosomes to T cell regulation.

Tumour cell-derived exosomes carrying PD-L1 have been suggested to contribute to malignant immunosuppression, but are often associated with the clinical benefits of compensatory immune checkpoint targeted therapies (Chen et al., 2018; Poggio et al., 2019; Ricklefs et al., 2018). Although tumoral exosome-PD-L1 has been reported to be deleterious for cancer patients (Chen et al., 2018; Poggio et al., 2019; Ricklefs et al., 2018), our findings indicate that WJMSC sEV-PD-L1 might indeed be beneficial for treating aGvHD patients through targeting CD4<sup>+</sup> T cells. However, increased sEV-PD-L1 may enhance both inhibitory PD-L1/PD1 (Wolfgang Koestner et al., 2011) and stimulatory PD-L1/CD80 (Cassady et al., 2018; Ni et al., 2017) on the donor CD8<sup>+</sup> T cells related to the GvL. Regarding the former point, the completed clinical trial (NCT03158896) of patients with hemopoietic malignancies have evaluated malignancy recurrence and did not show increased malignancy relapse post-WJMSC therapy even with longer follow up (Soder et al., 2020). It has been suggested that MSC-associated exosomes may reduce tumour growth by impairing angiogenesis and increasing apoptosis (Brossa et al., 2020). The identification of sEV-carried PD-L1 further expands the potential application of WJMSC-derived sEVs for their anti-tumour therapy through PD-L1/CD80 checkpoint regulation. More importantly, regarding their immunomodulation roles (Gomzikova et al., 2019), our study offers, for the first time, a rationale to further develop a new generation of cell free therapeutics for aGvHD based on WJMSC-derived sEVs.

## 4 | METHODS

### 4.1 | Production and maintenance of therapeutic WJMSCs

Umbilical cord specimens were obtained from individuals enrolled under the Institutional Review Board-approved protocol (HSC#1546) following good manufacturing practices (GMP). Umbilical cords were collected from healthy women (18~35-year old) who underwent elective cesarean section after full-term pregnancy. The cord was thoroughly washed twice with sterile phosphate buffered saline (PBS), blood vessels were removed, and pieces of cord tissue (approximately 2–3 mm in diameter) were seeded onto tissue culture dishes containing Stem MACS MSC Expansion Media (Miltenyi Biotec, Germany), penicillin 100 U/ml, and streptomycin 100 µg/ml (Mediatech). Explant cultures were incubated at 37°C in a humidified atmosphere containing 5% CO<sub>2</sub>. Medium was changed every 3–4 days and tissue explants were removed after 21 days of culture to allow the migration of cells from the explants. Once between 80–90% confluency, adherent cells were trypsinized using TrypLE Select (Life Technologies) and reseeded in tissue culture flasks (Corning) for further culture expansion. Low-passage WJMSCs (< 4 frozen/thawed cycles) were cultured in Stem MACS MSC Expansion Media. High-passage WJMSCs (> 4 < 10 frozen/thawed cycles) were cultured in conditional DMEM media supplied with 15% (v/v) fetal bovine serum (FBS).

### 4.2 | In vitro WJMSC differentiation

WJMSCs were differentiated into fat cells, cartilage cells and bone cells using human MSC differentiation kits following the standard protocol provided by the manufacturer (ThermoFisher Scientific, USA). Differentiated cells were fixed with 4% formaldehyde (PFA) solution and washed twice with PBS for histochemical analysis. In brief, bone cells were stained with 2% Alizarin Red S (Sigma, USA) prepared in H<sub>2</sub>O for at least 45 min, cartilage cells were stained with 1% Alcian blue (Millipore, USA) solution prepared in 0.1 N HCL for 30 min and fat cells were stained with 0.5% Oil red O (Sigma, USA) solution prepared in propylene glycol for 50–60 min. Images were recorded by using Nikon Digital Imaging Head (Nikon, Japan) and analysed by MetaMorph 7.7.0 imaging software (Molecular Devices, USA).

### 4.3 | Flow cytometry

WJMSCs were characterized by flow cytometry using the BD Stemflow Human MSC analysis kit (BD Biosciences, USA). WJMSCs were washed with PBS and detached using TrypLE Select and resuspended in staining buffer (1% FBS in PBS). WJMSCs were stained with multiple fluorochrome-conjugated antibody cocktails for positive and negative selection markers. Positive marker cocktail included APC-conjugated anti-CD73, FITC-conjugated anti-CD90, and PerCP-Cy5.5-conjugated anti-CD105. The negative marker cocktail included PE-conjugated antibodies against CD45, CD34, CD11b, CD19, and HLA-DR. WJMSCs were stained with PE-conjugated anti-human PD-L1 (Biolegend, USA). Human PBMCs were stained by anti-human antibodies listed as below: Anti- CD3 PE-Cy5/CD4 PE/CD8 FITC Cocktail, APC anti- CD154 and PE-dazzle anti- ZAP70 Phospho (Tyr319)/Syk(Tyr352), and APC/fire anti-PD1 antibodies were purchased from Biolegend (USA). Antibodies anti- CD3, CD4 APC, CD8 FITC, CD14PerCP, and IFN-γ PE proteins were purchased from Miltenyi Biotec (Germany). To stain anti-IFN-γ and pZAP7 antibodies, cells were fixed with 4% formaldehyde and permeabilized with 10 × permeabilization buffer (Invitrogen, USA). Human sEVs on mouse PBMCs were stained by anti-human PD-L1 PE (Biolegend, USA) and rat anti-mouse CD3 FITC (Biolegend, USA). Biotin-labelled human sEVs on mouse PBMCs were stained by streptavidin conjugated with PE/Cyanine 7 (Biolegend, USA) and rat anti-mouse CD3 FITC (Biolegend, USA). All antibodies were used at a dilution of 1:100. Flow cytometric analysis was performed using BD LSR II analyser (Becton Dickinson, USA) or Attune NxT multiparameter flow cytometer (Invitrogen, USA).

### 4.4 | sEV enrichment and characterization

Either 500 ml supernatant from WJMSC culture or 1 ml blood plasma sample from aGvHD patients was spun down at 400 × g for 10 min to remove cell debris. Then, the supernatant was spun down at 2000 × g for 30 min to remove apoptotic bodies. This was followed by ultracentrifugation spins at 10,000 × g for 1.5 h and 100,000 × g centrifugation for 1.5 h, both at 4°C. The pellet was washed with PBS and spun 100,000 × g centrifugation for 1.5 h at 4°C. Finally, the pellet was resuspended in PBS. To enrich for small EVs, extracellular vesicle pellets were further passed through qEVoriginal/70 nm columns (Izon Science, USA) according to the protocol provided by the manufacturer. The size of the sEVs was measured by NanoSight LM10 system and data was analysed using the NTA software v2.3 (NanoSight Ltd; United Kingdom).

## 4.5 | Immunoblotting

WJMCSs and sEVs were lysed with RIPA buffer containing a Halt protease Inhibitor single-use cocktail (Thermo Scientific). Membrane-bound PD-L1 were extracted using Mem-PER™ plus membrane protein extraction kit following the manufacturer's instruction (Thermoscientific, USA). Protein lysates were separated by a Mini-protean TGX precast gel (BIO-RAD, USA) and transferred onto a PVDF membrane (BIO-RAD, USA). Western blots were performed according to the standard techniques. The following antibodies were used at a dilution of 1:1000 in 5% nonfat milk unless otherwise stated: goat anti-human PD-L1 and PDL2 (R&D), Rabbit anti-human CD90, CD105 (Thermo Scientific), Rabbit anti-human CD9, CD81, HSP70, and CD63 (System Biosciences) and mouse anti-human  $\beta$ -actin (1:10,000, Sigma). Secondary antibodies include donkey anti-goat-HRP (R&D), goat-anti-rabbit-HRP (Cell Signalling) and goat anti-mouse antibody conjugated with HRP (Sigma). Signals were developed by using Pierce ECL Western Blotting Substrate (Thermo Scientific).

## 4.6 | Transmission Electron Microscopy (TEM)

TEM was carried out as previously reported (Chen et al., 2018). In brief, 10  $\mu$ l WJMCS sEVs were dropped on the spot plate and glow discharge carbon filmed nickel grids (Electron Microscopy Sciences, USA) were floated on the drops for 20 min. Grids were washed three times with H<sub>2</sub>O and fixed with 2.5 glutaraldehyde in 100 mM sodium cacodylate buffer (PH 7.0) for 1 h. Negative staining was performed by using 3% solution of neutral sodium phosphotungstate for 20 s. For immune-gold staining, grids were incubated with mouse monoclonal Leaf™ purified anti-human PD-L1 antibody (1:250, Biolegend, USA) for 60 min. Grids were washed three times with H<sub>2</sub>O followed by incubation with goat anti-mouse IgG conjugated with gold (1:500, Abcam, USA) for 1 h. Again, grids were then washed three times with H<sub>2</sub>O. Finally, grids were fixed with 1% glutaraldehyde and stained with 1% uranyl acetate for 5 s, dried and viewed under a JEOL JEM-1400 transmission electron microscope (JEOL, USA) equipped with a Lab6 gun at 100 KV.

## 4.7 | Enzyme-linked immunosorbent assay (ELISA)

Samples from blood plasma, cell culture supernatant and purified WJMCS sEVs were added to 96-wll plate to detect the human PD-L1 using a Human/Cynomolgus Monkey B7-H1 Elisa kit according to the manufacturer's instructions (R&D systems, USA). For detection of IFN- $\gamma$ , ST2 and REG3 alpha (REG3A), plates were prepared using DuoSet human IFN- $\gamma$ , ST2 and REG3A ELISA kit according to the manufacturers' instructions (R&D systems, USA). Coated plates were added by the diluted plasma samples from aGvHD patients and detected by ELISA detection antibodies (R&D systems, USA). O.D. Value was read at an absorbance of 450 nm using Infinite 200 PRO plate reader (Tecan US). To determine soluble PD-L1 in conditional medium and human plasma samples, exosome-free conditional medium or plasma samples were generated by either ultracentrifugation (shown as above) or Amicon Ultra-4 centrifugal filters according to the manufacturer's instructions (Millipore, USA).

## 4.8 | Quantitative PCR (qPCR)

The mRNA expression of human PD-L1 was examined by qPCRs. Forward primer: 5'-GCAAGGCGATTAAGTTGGGT-3' and Reverse primer: 5'-GTGCTCTTCATCTTGTTGGT-3' were designed. Total RNA was extracted from cells by using TRIzol reagent (ambio, USA). The first-strand cDNA was synthesized using High Capacity cDNA Reverse Transcription Kit (Applied biosystems, USA) according to the manufacture's protocols. Quantitative PCRs were conducted following the standard protocols using Maxima SYBR Green/Rox qPCR Master Mix (2X) (Thermo scientific, USA). Reactions were conducted on CFX96 Real-Time System (Bio-Rad, USA) following the standard procedures. qPCR experiments were independently repeated three times.

## 4.9 | Immunofluorescence staining

Human PBMCs were isolated with Ficoll-Hypaque solution (STEMCELL, USA) by centrifugation at 400 x g for 30 min followed by washing with PBS. CD3<sup>+</sup> T cells were further sorted using CD3 micro beads (Miltenyi Biotec, Germany). Sorted CD3<sup>+</sup> T cells were activated by CD3/CD28 Dynabeads (1:1 ratio) and seeded on WJMCSs. PBMCs and WJMCSs were cocultured in conditional DMEM medium supplied with 10% FBS for overnight. Immunofluorescence staining was carried out by following the standard procedures. Cells were fixed with 4% PFA and stained by rabbit anti-human CD3 (1:250, Cell Marque, USA) and mouse anti-human PD1 (1:250, eBioscience, USA) for 1 h. These were then washed thrice with PBS. Then, the cells were incubated

with goat secondary antibodies anti-mouse IgG- Alex594 (1:500, Invitrogen, USA) and anti-rabbit IgG-FITC (1:500, Invitrogen, USA). For PD-L1 staining, WJMSCs were cultured in conditioned DMEM medium supplied with 10% FBS and induced with 2.5 ng/ml human recombinant IFN- $\gamma$  protein (R&D, USA). Cells were stained with rabbit anti-human PD-L1 antibody (1:250, Thermal scientific, USA) and washed thrice with PBS. These cells were stained with anti-rabbit IgG conjugated with Alex 594. Finally, cells were mounted with VECTASHIELD mounting medium with DAPI (Vector, USA). Images were recorded by using Nikon Digital Imaging Head (Nikon, Japan) and analysed by MetaMorph 7.7.0 imaging software (Molecular Devices, USA).

#### 4.10 | Clinical blood sample preparation

The Midwest Stem Cell Therapy Center at the University of Kansas Medical Center has developed and manufactured clinical grade WJMSCs (MSCTC-0010) for use in humans. Therapeutic WJMSCs have been tested in a Phase I clinical trial in subjects with high-risk aGvHD and this study showed preliminary safety of two doses of therapeutic WJMSCs by IV administration (ClinicalTrials.gov Identifier: NCT03158896 – “Evaluation of Umbilical Cord-Derived Wharton’s Jelly Stem Cells for the Treatment of Acute Graft Versus Host Disease”). A total of 10 subjects were treated in two dose cohorts of five subjects; five patients had high risk acute myelogenous leukaemia, two myelodysplastic syndrome, two myelofibrosis, and one had T cell non-Hodgkin’s lymphoma. The study was approved by the institutional review board and was conducted in accordance with the principles of the Declaration of Helsinki and International Conference on Harmonization Good Clinical Practice Guidelines. All the patients provided written informed consent (additional details regarding clinical trial design and outcomes are in Soder et al., 2020 (Soder et al., 2020)). Cells were administered via IV infusion at a dose of  $1.2 \times 10^6$  WJMSCs/kg for two doses in the first cohort and  $10 \times 10^6$  WJMSCs/kg in the second cohort and the subjects were followed over a six-month period. Patient blood samples were collected prior to the first dose of and then weekly for 4 weeks and patients’ aGvHD grades were further evaluated according to the clinic diagnostic standards. For dynamic analysis, patient blood samples were collected at individual timepoints before WJMSCs administration (pre-dose) and after WJMSCs administration (post-30 min, post-1 h, post-2 h, post-4 h, and post-8 h).

#### 4.11 | ExoView

sEV numbers in blood plasma were measured using ExoView™ Tetraspanin kits (NanoView Bioscience, USA) according to manufacturer’s instructions. In brief, human and mouse plasma samples were diluted with incubation solution (1:1 dilution). 35  $\mu$ l of diluted plasma samples was loaded on the Nanoview chips and incubated overnight. Each chip included three mouse capture antibodies targeted against sEV tetraspanin markers (CD9, CD63, CD81). After washing thrice with incubation solution, Nanoview chips were stained with detection antibodies cocktail for 1 h. Detection antibody cocktail contained three mouse antibodies anti-human CD81 conjugated with Alex 488, CD63 conjugated with Alex 647 and CD9 conjugated with Alex 555. Again, these were washed thrice with incubation solution, immunofluorescent staining on the chips was recorded with ExoView™ R100 automated imager and analysed using ExoScan 2.5.5 acquisition software (NanoView Bioscience, USA).

#### 4.12 | In vivo WJMSC sEV injection and blood collection

All animal experiments were performed according to protocols (2017-2387 & 2020-2549) approved by the Institutional Animal Care and Use Committee (IACUC) of the University of Kansas Medical Center. 4 mg/kg human WJMSC sEVs were injected into 8-week immunodeficient NSG mice (NOD.Cg-Prkdcscid Il2rgtm1Wjl/SzJ) through intravenous (IV) injection according to a previous protocol (Ehx et al., 2018). WJMSC sEVs were labelled with biotin using EZLabel™ antibody biotin labelling kit according to the standard protocol provided by the manufacturer (Biovision, USA). 4 mg/kg biotin labelled WJMSC sEVs were injected into mice through intravenous (IV) injection. 1 h, 4 h, or 12 h after injection, mouse facial blood withdrawal was performed using 5 mm animal lancet (Goldenrod, USA) and about 2–3 drops of blood samples were collected into an EDTA micro-collection tube (Microtainer, USA). To obtain PBMCs, whole mouse blood was diluted with RBC lysing solution (Biolegend, USA) and kept at RT for 10 min. Cells were spun for 10 min at 250 x g and washed with PBS for one time.

#### 4.13 | In vitro TCR-mediated T cell activation

All patients who provided blood samples for this study did so under written informed consent and University of Kansas Medical Center Institutional Review Board approved the collection protocol (HSC #5929) and following U.S. Common Rule. De-identified clinical samples were provided by the KU Cancer Center’s Biospecimen Repository Core Facility (BRCF) along with detailed clinical outcomes and phenotypes. Once the patient provides written, informed consent in accordance with the BRCF IRB protocol, a blood sample is collected, the sample is de-identified to the user, and transported directly to the laboratory for



processing. Five ml whole blood was used to prepare PBMCs using lymphocyte separation medium (Corning, USA) and spun for 30 min at 400 x g through density gradient centrifugation. After washing with PBS,  $1 \times 10^5$  PBMCs per well were seeded in 96-well plates with 1 ml of Hyclone™ RPMI-1640 medium (GE healthcare life sciences, USA) supplemented with 10% FBS, 10  $\mu$ M HEPES buffer, 100 U/ml penicillin-streptomycin. PBMCs were activated with CD3/CD28 Dynabeads (Gibco, USA) at a dilution of 1:1 ratio as previously described (Chattopadhyay et al., 2005; Chattopadhyay et al., 2006). T cell activation was measured by dual CD154<sup>+</sup>/CD4<sup>+</sup> or PD1<sup>+</sup>/CD4<sup>+</sup> T cells with flow cytometry. Unstimulated or stimulated PBMCs were treated with 0.2-40  $\mu$ g/ml WJMISC sEVs. Stimulated PBMCs were treated with 2.5-40 ng/ml human recombinant PD-L1 protein (R&D systems, USA) for 12 h. Stimulated PBMCs were treated with 10  $\mu$ g/ml WJMISC sEVs, 3  $\mu$ g/ml anti-human PD-L1 internalization antibody/IgG (Novus biologicals, USA), or 1  $\mu$ g/ml recombinant human PD-L1 protein (R&D systems, USA) for overnight. Stimulated PBMCs were treated with WT (*PD-L1*<sup>+/+</sup>) or KO (*PD-L1*<sup>-/-</sup>) WJMISCs for 48 h and the ratio of WJMISCs to PBMCs were 1 to 10. Stimulated PBMCs were treated with WT (*PD-L1*<sup>+/+</sup>) or KO (*PD-L1*<sup>-/-</sup>) WJMISC-derived sEVs for both 12 h and 36 h. For CD8<sup>+</sup> T cell activation, PBMCs were isolated from donors and stimulated with 1 ng/ml PepTivator CMV-pp65 peptide (Miltenyi Biotec, Germany). Intracellular IFN- $\gamma$  in CD8<sup>+</sup> T cells was examined by using Rapid Cytokine Inspector kit (Miltenyi Biotec, Germany) following the manufacturer's instruction.

#### 4.14 | Biolayer interferometry (BLI)

All solutions were made in octet kinetics buffer (1x PBS with 0.1% BSA and 0.02% Tween-20). Goat anti-human PD-L1 antibody or IgG control (R&D systems, USA) was diluted in 200  $\mu$ l kinetics buffer with the final 5 ng/ml concentration. 20  $\mu$ g WJMISC-derived sEVs and 0-1 mg/ml human recombinant PD-L1 protein (R&D systems, USA) were suspended in 200  $\mu$ l in kinetics buffer. Each kinetic experiment consisted of four steps: (1) protein G biosensors were equilibrated in kinetics buffer for 20 min, (2) goat anti-human PD-L1 antibody/IgG control were loaded onto the protein G biosensors for 400 s (3) a baseline was established in kinetics buffer for 1 min, (4) binding WJMISC-derived sEVs 1-2k s. BLI experiments were recorded in sterile PBS at 25°C on Octet Red instrument (ForteBio LLC, USA). Kinetic assay was performed at 25°C with 1000 rpm plate rotation. Software provided with the Octet system (version 7.1) was used to fit the data to a one-to-one model and obtain  $k_{on}$ ,  $k_{off}$ , and  $K_D$  values.

#### 4.15 | PD-L1 Knockout (KO) in WJMISCs and characterization

*PD-L1* gene in WJMISCs was genetically disrupted by CRIPR-cas9 gene editing as described in the previous studies (Cong et al., 2013; Shalem et al., 2014). *Pd1*sgRNA (targeting uCUG): 5'-GGGCCAGTCTCCTCGCCTGC-3' and *Pd1*sgRNA (targeting uAUG): 5'-TGGTCCCAAGCCTCATGCC-3' were designed and by Shalem et al (Shalem et al., 2014) and cloned into pSpCas9(BB)-2A-GFP (PX458) vector (Addgene no. 48138). Non-targeting control sgRNA was used side-by-side with *PD-L1* sgRNA to rule out phenotypes result from nonspecific editing. HEK293T cells (Addgene) were co-transfected with packaging vectors psPAX2 and pCI-VSVG (Addgene) with above lentiviral vectors using lipofectamine 2000 (Invitrogen). Media of the HEK293T cells was changed 18 h after transfection and viral supernatants were collected 24 and 48 h later and filtered to transfect WJMISCs. After infection, WJMISCs were cultured in DMEM medium supplied 10% FBS and positive clones were screened by adding 0.5-2  $\mu$ g/ml puromycin. To confirm *PD-L1* gene knockout, genomic DNAs were isolated from WJMISCs using QIAamp DNA (Qiagen, USA). A 300 nt DNA fragment covered the editing target region was amplified by PCR and cloned into pCRII vector using TA cloning kit (Thermal fisher, USA). The T7 and Sp6 promoters provide on the pCR II vector were used to sequence cloned DNA fragments. Sequence alignment was performed using bioinformatics software DNASTAR (Dnastar, USA).

#### 4.16 | PDI/NFAT assay

PDI/NFAT reporter Jurkat T cells were purchased from BPS Bioscience (USA) and cultured with growth medium 2A conditional medium supplied with 10% FBS. Cells were activated by human T-activator CD3/CD28 Dyna beads (1:1 ratio, Gibco, USA). Activated cells were treated with 20  $\mu$ g/ml PD-L1 WT or KO WJMISC EVs, 3  $\mu$ g/ml PD-L1 antibody or isotype control and 1  $\mu$ g/ml recombinant human PD-L1 protein. Luciferase assay was conducted using One-Step Luciferase assay system (BPS Bioscience, USA) according to the procedures provided by the manufacturer. O.D. Value was read using Infinite 200 PRO plate reader (Tecan, US).

#### 4.17 | MTT assay

CD3<sup>+</sup> T cells were sorted from healthy human PBMCs using CD3 micro beads (Miltenyi Biotec, Germany). CD3<sup>+</sup> T cells were seeded into 96-well plates in RPMI-1640 medium supplied with 10% FBS and treated with 10  $\mu$ g/ml WJMISC sEVs for 6 days.

Cell toxicity was examined by using MTT assay kit (BioVision, USA) according to the manufacturer's instructions. Plates were read by a micro-plate reader at 490 nm wavelength as above.

#### 4.18 | Statistics

Data were analysed and statistics performed in GraphPad Prism 8. Data were expressed as means  $\pm$  s.e.m (standard error of mean). A one-tailed, unpaired Student's *t* test was used for pair-wise comparison or one-way analysis of variance (ANOVA) with Dunnett's test. For correlation analysis, a two-sided Pearson's correlation test was used. \**P* < 0.05, \*\**P* < 0.01, \*\*\**P* < 0.005. and the exact *P* values are indicated in the figures.

#### ACKNOWLEDGEMENTS

We thank Jim Mitchell and the Midwest Stem Cell Therapy Center, which was funded by State legislature and private donors for providing WJMSCs. We acknowledge the support from Larysa Stroganova and Pat St. John (Electron Microscopy Research Laboratory, KUMC), Richard Hastings (Flow Cytometry Core Laboratory, KUMC), Drs. Safinur Atay (Department of Pathology and Laboratory Medicine, KUMC), and Andrew Keightley (School of Biological and Chemical Sciences, the University of Missouri-Kansas City) for their technical assistances. We thank Dr. Kathy Roby (Department of Anatomy & Cell Biology, KUMC) for breeding and providing NSG mice and Dr. Mihaela E. Sardu (Stowers Institute for Medical Research) for bioinformatic support. We acknowledge the University of Kansas Cancer Center's Biospecimen Repository Core Facility and staff, in particular Ms. Sophia McCormick and Ms. Anh Pham, who are sponsored, in part, by the NIH/NCI Cancer Center Support Grant P30 CA168524. The Electron Microscope Research Laboratory and Flow Cytometry Core Laboratory are supported, in part, by NIH/NIGMS COBRE grant P20 GM104936. The JEOL JEM-1400 transmission electron microscope was purchased with funds from NIH grant 1S10RR027564. We acknowledge the Biobanking and Biomarker Validation Core support, which is sponsored, in part, by the Kansas Institute for Precision Medicine NIH/NIGMS COBRE grant P20 GM130423. This work was supported in part by a grant from the NIGMS (P20 GM130423 to A.K.G.) and The University of Kansas Cancer Center Support Grant (P30 CA168524 to N.D. & A.K.G.). Funding for the MSCTC was through the Kansas State Legislature (Senate Bill 199, 2012). A.K.G. is the Chancellors Distinguished Chair in Biomedical Sciences Endowed Professor.

#### CONFLICTS OF INTEREST

The authors declare no competing interests.

#### AUTHOR CONTRIBUTIONS

Meizhang Li designed and performed the experiments and analysed the data. Buddhadeb Dawn directed the Midwest Stem Cell Therapy Center and Rupal Soder generated, characterized, and maintained clinical grade WJMSCs. Neil Dunavin, Sunil Abhyankar, and Siddhartha Ganguly took charge of clinical trial and collected clinical samples. Haitham Abdelhakim, Camille V. Trinidad, and Mitch Braun discussed the hypothesis and contributed to data analysis related to in vitro T cell activation. Harsh B. Pathak and Ziyang Pessetto discussed the hypothesis and contributed to data analysis related to clinical trial. Clayton Deighan performed the ExoView to count exosome number in human plasma samples. Joseph McGuirk, Neil Dunavin, and Andrew K. Godwin coordinated the project, and Meizhang Li, Neil Dunavin, and Andrew K. Godwin interpreted data and wrote the manuscript. All authors reviewed and approved the manuscript. Correspondence and requests for materials should be addressed to Andrew K. Godwin (agodwin@kumc.edu).

#### REFERENCES

- Ankrum, J. A., Ong, J. F., & Karp, J. M. (2014). Mesenchymal stem cells: immune evasive, not immune privileged. *Nature Biotechnology*, 32(3), 252.
- Barbash, I. M., Chouraqui, P., Baron, J., Feinberg, M. S., Etzion, S., Tessone, A., Miller, L., Guetta, E., Zipori, D., Kedes, L. H., Kloner, R. A., & Leor, J. (2003). Systemic delivery of bone marrow-derived mesenchymal stem cells to the infarcted myocardium: Feasibility, cell migration, and body distribution. *Circulation*, 108(7), 863–868.
- Barile, L., & Vassalli, G. (2017). Exosomes: therapy delivery tools and biomarkers of diseases. *Pharmacology & Therapeutics*, 174, 63–78.
- Blazar, B. R., Murphy, W. J., & Abedi, M. (2012). Advances in graft-versus-host disease biology and therapy. *Nature Reviews Immunology*, 12(6), 443–458.
- Boussiotis, V. A. (2016). Molecular and biochemical aspects of the PD-1 checkpoint pathway. *New England Journal of Medicine*, 375(18), 1767–1778.
- Brossa, A., Fonsato, V., Grange, C., Tritta, S., Tapparo, M., Calvetti, R., Cedrino, M., Fallo, S., Gontero, P., Camussi, G., & Bussolati, B. (2020). Extracellular vesicles from human liver stem cells inhibit renal cancer stem cell-derived tumor growth in vitro and in vivo. *International Journal of Cancer*, 147(6), 1694–1706.
- Brown, C., Mckee, C., Bakshi, S., Walker, K., Hakman, E., Halassy, S., Svinarich, D., Dodds, R., Govind, C. K., & Chaudhry, G. R. (2019). Mesenchymal stem cells: cell therapy and regeneration potential. *Journal of Tissue Engineering and Regenerative Medicine*, 13(9), 1738–1755.
- Butte, M. J., Keir, M. E., Phamduy, T. B., Sharpe, A. H., & Freeman, G. J. (2007). Programmed death-1 ligand 1 interacts specifically with the B7-1 costimulatory molecule to inhibit T cell responses. *Immunity*, 27(1), 111–122.
- Butte, M. J., Peña-Cruz, V., Kim, Mi-J., Freeman, G. J., & Sharpe, A. H. (2008). Interaction of human PD-L1 and B7-1. *Molecular Immunology*, 45(13), 3567–3572.
- Carvalho, A. É. S.-., Sousa, M. R. R., Alencar-Silva, T., Carvalho, J. L., & Saldanha-Araujo, F. (2019). Mesenchymal stem cells immunomodulation: the road to IFN-gamma licensing and the path ahead. *Cytokine & Growth Factor Reviews*, 47:32–42.

- Cassady, K., Martin, P. J., & Zeng, D. (2018). Regulation of GVHD and GVL activity via PD-L1 interaction with PD-1 and CD80. *Frontiers in immunology*, 9, 3061.
- Chakraverty, R., & Sykes, M. (2007). The role of antigen-presenting cells in triggering graft-versus-host disease and graft-versus-leukemia. *Blood*, 110(1), 9–17.
- Chattopadhyay, P. K., Yu, J., & Roederer, M. (2005). A live-cell assay to detect antigen-specific CD4<sup>+</sup> T cells with diverse cytokine profiles. *Nature Medicine*, 11(10), 1113–1117.
- Chattopadhyay, P. K., Yu, J., & Roederer, M. (2006). Live-cell assay to detect antigen-specific CD4<sup>+</sup> T-cell responses by CD154 expression. *Nature Protocols*, 1(1), 1–6.
- Chen, G., Huang, A. C., Zhang, W., Zhang, G., Wu, M., Xu, W., Yu, Z., Yang, J., Wang, B., Sun, H., Xia, H., Man, Q., Zhong, W., Antelo, L. F., Wu, B., Xiong, X., Liu, X., Guan, L., Li, T., ... Guo, W. (2018). Exosomal PD-L1 contributes to immunosuppression and is associated with anti-PD-1 response. *Nature*, 560(7718), 382.
- Chen, W., Huang, Y., Han, J., Yu, L., Li, Y., Lu, Z., Li, H., Liu, Z., Shi, C., Duan, F., & Xiao, Y. (2016). Immunomodulatory effects of mesenchymal stromal cells-derived exosome. *Immunologic Research*, 64(4), 831–840.
- Cong, L., Ran, F. A., Cox, D., Lin, S., Barretto, R., Habib, N., Hsu, P. D., Wu, X., Jiang, W., Marraffini, L. A., & Zhang, F. (2013). Multiplex genome engineering using CRISPR/Cas systems. *Science*, 339(6121), 819.
- Daassi, D., Mahoney, K. M., & Freeman, G. J. (2020). The importance of exosomal PDL1 in tumour immune evasion. *Nature Reviews Immunology*, 20(4), 209–215.
- Davies, L. C., Heldring, N., Kadri, N., & Le Blanc, K. (2017). Mesenchymal stromal cell secretion of programmed death-1 ligands regulates T cell mediated immunosuppression. *Stem Cells*, 35(3), 766–776.
- Dotoli, G. M., De Santis, G. C., Orellana, M. D., De Lima Prata, K., Caruso, S. R., Fernandes, T. R., Rensi Colturato, V. A., Kondo, A. T., Hamerschlak, N., Simões, B. P., & Covas, D. T. (2017). Mesenchymal stromal cell infusion to treat steroid-refractory acute GvHD III/IV after hematopoietic stem cell transplantation. *Bone Marrow Transplantation*, 52(6), 859–862.
- Dunavin, N., Braun, M. W., Li, M., Godwin, A. K., Abhyankar, S., & Yankee, T. M. (2019). Biomarker profiling of steroid-resistant chronic GvHD patients undergoing extracorporeal photopheresis demonstrates high ST2 levels at treatment onset and decline during therapy. *Advances in Cell and Gene Therapy*, 2(1), e32.
- Eggenhofer, E., Benseler, V., Kroemer, A., Popp, F. C., Geissler, E. K., Schlitt, H. J., Baan, C. C., Dahlke, M. H., & Hoogduijn, M. J. (2012). Mesenchymal stem cells are short-lived and do not migrate beyond the lungs after intravenous infusion. *Frontiers in immunology*, 3:297.
- Ehx, G., Somja, J., Warnatz, H.-J., Ritacco, C., Hannon, M., Delens, L., Fransolet, G., Delvenne, P., Muller, J., Beguin, Y., Lehrach, H., Belle, L., Humblet-Baron, S., & Baron, F. (2018). Xenogeneic graft-versus-host disease in humanized NSG and NSG-HLA-A2/HHD mice. *Frontiers in immunology*, 9:1943.
- Francisco, L. M., Salinas, V. H., Brown, K. E., Vanguri, V. K., Freeman, G. J., Kuchroo, V. K., & Sharpe, A. H. (2009). PD-L1 regulates the development, maintenance, and function of induced regulatory T cells. *Journal of Experimental Medicine*, 206(13), 3015–3029.
- Freeman, G. J., Long, A. J., Iwai, Y., Bourque, K., Chernova, T., Nishimura, H., Fitz, L. J., Malenkovich, N., Okazaki, T., Byrne, M. C., Horton, H. F., Fouser, L., Carter, L., Ling, V., Bowman, M. R., Carreno, B. M., Collins, M., Wood, C. R., & Honjo, T. (2000). Engagement of the PD-1 immunoinhibitory receptor by a novel B7 family member leads to negative regulation of lymphocyte activation. *Journal of Experimental Medicine*, 192(7), 1027–1034.
- Fujii, S., Miura, Y., Fujishiro, A., Shindo, T., Shimazu, Y., Hirai, H., Tahara, H., Takaori-Kondo, A., Ichinohe, T., & Maekawa, T. (2018). Graft-versus-host disease amelioration by human bone marrow mesenchymal stromal/stem cell-derived extracellular vesicles is associated with peripheral preservation of naive T cell populations. *Stem Cells*, 36(3), 434.
- Fujiwara, H., Maeda, Y., Kobayashi, K., Nishimori, H., Matsuoka, K.-I., Fujii, N., Kondo, E., Tanaka, T., Chen, L., Azuma, M., Yagita, H., & Tanimoto, M. (2014). Programmed death-1 pathway in host tissues ameliorates Th17/Th1-mediated experimental chronic graft-versus-host disease. *Journal of Immunology*, 193(5), 2565–2573.
- Fumihiko Tsushima, S. Y., Shin, T., Flies, A., Flies, S., Xu, H., Tamada, K., Pardoll, D. M., & Chen, L. (2007). Interaction between B7-H1 and PD-1 determines initiation and reversal of T-cell anergy. *Blood*, 110(1), 6.
- Galipeau, J., & Sensébé, L. (2018). Mesenchymal stromal cells: clinical challenges and therapeutic opportunities. *Cell Stem Cell*, 22(6), 824–833.
- Gaud, G., Lesourne, R., & Love, P. E. (2018). Regulatory mechanisms in T cell receptor signalling. *Nature Reviews Immunology*, 18(8), 485–497.
- Gomzikova, M. O., James, V., & Rizvanov, A. A. (2019). Therapeutic application of mesenchymal stem cells derived extracellular vesicles for immunomodulation. *Frontiers in immunology*, 10:2663.
- Greaves, P., & Gribben, J. G. (2013). The role of B7 family molecules in hematologic malignancy. *Blood*, 121(5), 734–744.
- Guan, Q., Li, Y., Shpiruk, T., Bhagwat, S., & Wall, D. A. (2018). Inducible indoleamine 2,3-dioxygenase 1 and programmed death ligand 1 expression as the potency marker for mesenchymal stromal cells. *Cytotherapy*, 20(5), 639.
- Ha, D. H., Kim, H.-K., Lee, J., Kwon, H. H., Park, G.-H., Yang, S. H., Jung, J. Y., Choi, H., Lee, J. H., Sung, S., Yi, Y. W., & Cho, B. S. (2020). Mesenchymal stem/stromal cell-derived exosomes for immunomodulatory therapeutics and skin regeneration. *Cells*, 9(5), 1157.
- Ito, M., & Shizuru, J. A. (1999). Graft-vs.-lymphoma effect in an allogeneic hematopoietic stem cell transplantation model. *Biology of Blood and Marrow Transplantation*, 5(6), 357–368.
- Kebricci, P., Hayes, J., Daly, A., Uberti, J., Marks, D. I., Soiffer, R., Waller, E. K., Burke, E., Skerrett, D., Shpall, E., & Martin, P. J. (2020). A phase 3 randomized study of remestemcel-L versus placebo added to second-line therapy in patients with steroid-refractory acute graft-versus-host disease. *Biology of Blood and Marrow Transplantation*, 26(5), 835–844.
- Keir, M. E., Freeman, G. J., & Sharpe, A. H. (2007). PD-1 regulates self-reactive CD8<sup>+</sup> T cell responses to antigen in lymph nodes and tissues. *Journal of Immunology*, 179(8), 5064–5070.
- Kitazawa, Y., Fujino, M., Wang, Q., Kimura, H., Azuma, M., Kubo, M., Abe, R., & Li, X.-K. (2007). Involvement of the programmed death-1/programmed death-1 ligand pathway in CD4<sup>+</sup>CD25<sup>+</sup> regulatory T-cell activity to suppress alloimmune responses. *Transplantation*, 83(6), 774–782.
- Kordelas, L., Rebmann, V., Ludwig, A.-K., Radtke, S., Ruesing, J., Doeppner, T. R., Epple, M., Horn, P. A., Beelen, D. W., & Giebel, B. (2014). MSC-derived exosomes: a novel tool to treat therapy-refractory graft-versus-host disease. *Leukemia*, 28(4), 970–973.
- Krampera, M. (2011). Mesenchymal stromal cell 'licensing': a multistep process. *Leukemia*, 25(9), 1408.
- Kurtzberg, J., Abdel-Azim, H., Carpenter, P., Chaudhury, S., Horn, B., Mahadeo, K., Nemecek, E., Neudorf, S., Prasad, V., Prockop, S., Quigg, T., Satwani, P., Cheng, A., Burke, E., Hayes, J., & Skerrett, D. (2020). A phase 3, single-arm, prospective study of remestemcel-L, ex vivo culture-expanded adult human mesenchymal stromal cells for the treatment of pediatric patients who failed to respond to steroid treatment for acute graft-versus-host disease. *Biology of Blood and Marrow Transplantation*, 26(5), 845–854.
- Lai, P., Chen, X., Guo, L., Wang, Y., Liu, X., Liu, Y., Zhou, T., Huang, T., Geng, S., Luo, C., Huang, X., Wu, S., Ling, W., Du, X., He, C., & Weng, J. (2018). A potent immunomodulatory role of exosomes derived from mesenchymal stromal cells in preventing cGVHD. *Journal of hematology & oncology*, 11(1), 135.

- Levine, J. E., Logan, B. R., Wu, J., Alousi, A. M., Bolaños-Meade, J., Ferrara, J. L. M., Ho, V. T., Weisdorf, D. J., & Paczesny, S. (2012). Acute graft-versus-host disease biomarkers measured during therapy can predict treatment outcomes: a blood and marrow transplant clinical trials network study. *Blood*, *119*(16), 3854.
- Lugt, V., BT, M. T., Hanash, S., Ritz, J., Ho, V. T., Antin, J. H., Zhang, Q., Wong, C. H., Wang, H., Chin, A., Gomez, A., Harris, A. C., Levine, J. E., Choi, S. W., Couriel, D., Reddy, P., Ferrara, J. L., & Paczesny, S. (2013). ST2 as a marker for risk of therapy-resistant graft-versus-host disease and death. *New England Journal of Medicine*, *368*(6), 11.
- Maziarz, R. T., Devos, T., Bachier, C. R., Goldstein, S. C., Leis, J. F., Devine, S. M., Meyers, G., Gajewski, J. L., Maertens, J., Deans, R. J., Van't Hof, W., & Lazarus, H. M. (2015). Single and multiple dose MultiStem (multipotent adult progenitor cell) therapy prophylaxis of acute graft-versus-host disease in myeloablative allogeneic hematopoietic cell transplantation: a phase I trial. *Biology of Blood and Marrow Transplantation*, *21*(4), 720–728.
- Muroi, K., Miyamura, K., Okada, M., Yamashita, T., Murata, M., Ishikawa, T., Uike, N., Hidaka, M., Kobayashi, R., Imamura, M., Tanaka, J., Ohashi, K., Taniguchi, S., Ikeda, T., Eto, T., Mori, M., Yamaoka, M., & Ozawa, K. (2016). Bone marrow-derived mesenchymal stem cells (JR-031) for steroid-refractory grade III or IV acute graft-versus-host disease: a phase II/III study. *International Journal of Hematology*, *103*(2), 243–250.
- Ni, X., Song, Q., Cassidy, K., Deng, R., Jin, H., Zhang, M., Dong, H., Forman, S., Martin, P. J., Chen, Y.-Z., Wang, J., & Zeng, D. (2017). PD-L1 interacts with CD80 to regulate graft-versus-leukemia activity of donor CD8+ T cells. *Journal of Clinical Investigation*, *127*(5), 1960–1977.
- Pittenger, M. F., Discher, D. E., Péault, B. M., Phinney, D. G., Hare, J. M., & Caplan, A. I. (2019). Mesenchymal stem cell perspective: cell biology to clinical progress. *NPJ Regenerative Medicine*, *4*:22.
- Poggio, M., Hu, T., Pai, C.-C., Chu, B., Belair, C. D., Chang, A., Montabana, E., Lang, U. E., Fu, Qi, Fong, L., & Blleloch, R. (2019). Suppression of exosomal PD-L1 induces systemic anti-tumor immunity and memory. *Cell*, *177*(2), 414–427.e13.
- Ponce, D. M., Hilden, P., Mumaw, C., Devlin, S. M., Lubin, M., Giralt, S., Goldberg, J. D., Hanash, A., Hsu, K., Jenq, R., Perales, M.-A., Sauter, C., Van Den Brink, M. R. M., Young, J. W., Brentjens, R., Kernan, N. A., Prockop, S. E., O'reilly, R. J., Scaradavou, A., ... Barker, J. N. (2015). High day 28 ST2 levels predict for acute graft-versus-host disease and transplant-related mortality after cord blood transplantation. *Blood*, *125*(1), 199–205.
- Ratanatharathorn, V., Ayash, L., Lazarus, Hm, Fu, J., & Uberti, Jp. (2001). Chronic graft-versus-host disease: Clinical manifestation and therapy. *Bone Marrow Transplantation*, *28*(2), 121–129.
- Ricklefs, F. L., Alayo, Q., Krenzlin, H., Mahmoud, A. B., Speranza, M. C., Nakashima, H., Hayes, J. L., Lee, K., Balaj, L., Passaro, C., Rooj, A. K., Krasemann, S., Carter, B. S., Chen, C. C., Steed, T., Treiber, J., Rodig, S., Yang, K., Nakano, I., ... Chiocca, E. A. (2018). Immune evasion mediated by PD-L1 on glioblastoma-derived extracellular vesicles. *Science Advances*, *4*(3), eaar2766.
- Rowan, C. M., Pike, F., Cooke, K. R., Krance, R., Carpenter, P. A., Duncan, C., Jacobsohn, D. A., Bollard, C. M., Cruz, C. R. Y., Malatpure, A., Farag, S. S., Renbarger, J., Liu, H., Bakoyannis, G., Hanash, S., & Paczesny, S. (2020). Assessment of ST2 for risk of death following graft-versus-host disease in the pediatric and adult age groups. *Blood*, *135*(17), 1428–1437.
- Saha, A., O'Connor, R. S., Thangavelu, G., Lovitch, S. B., Dandamudi, D. B., Wilson, C. B., Vincent, B. G., Tkachev, V., Pawlicki, J. M., Furlan, S. N., Kean, L. S., Aoyama, K., Taylor, P. A., Panoskaltis-Mortari, A., Foncea, R., Ranganathan, P., Devine, S. M., Burrill, J. S., Guo, L., ... Blazar, B. R. (2016). Programmed death ligand-1 expression on donor T cells drives graft-versus-host disease lethality. *Journal of Clinical Investigation*, *126*(7), 2642–2660.
- Shalem, O., Sanjana, N. E., Hartenian, E., Shi, Xi, Scott, D. A., Mikkelsen, T. S., Heckl, D., Ebert, B. L., Root, D. E., Doench, J. G., & Zhang, F. (2014). Genome-scale CRISPR-Cas9 knockout screening in human cells. *Science*, *343*(6166), 84–87.
- Shi, Y., Wang, Yu, Li, Q., Liu, K., Hou, J., Shao, C., & Wang, Y. (2018). Immunoregulatory mechanisms of mesenchymal stem and stromal cells in inflammatory diseases. *Nature Reviews Nephrology*, *14*(8), 493–507.
- Soder, R. P., Dawn, B., Weiss, M. L., Dunavin, N., Weir, S., Mitchell, J., Li, M., Shune, L., Singh, A. K., Ganguly, S., Morrison, M., Abdelhakim, H., Godwin, A. K., Abhyankar, S., & Mcguirk, J. (2020). A phase I study to evaluate two doses of Wharton's jelly-derived mesenchymal stromal cells for the treatment of de novo high-risk or steroid-refractory acute graft versus host disease. *Stem Cell Reviews Reports*, *16*(5), 979–991.
- Te Boome, L. C. J., Mansilla, C., Van Der Wagen, L. E., Lindemans, C. A., Petersen, E. J., Spierings, E., Thus, K. A., Westinga, K., Plantinga, M., Bierings, M., Broers, A. E. C., Cuijpers, M. L. H., Van Imhoff, G. W., Janssen, J. J., Huisman, C., Zeerleder, S., Huls, G., Boelens, J. J., Wulffraat, N. M., ... Kuball, J. (2015). Biomarker profiling of steroid-resistant acute GVHD in patients after infusion of mesenchymal stromal cells. *Leukemia*, *29*(9), 1839–1846.
- Van Niel, G., D'angelo, G., & Raposo, G. (2018). Shedding light on the cell biology of extracellular vesicles. *Nature Reviews Molecular Cell Biology*, *19*(4), 213–228.
- Wolfgang Koestner, M. H., Herbst, J., Klein, C., Welte, K., Fruehauf, J., Flatley, A., Vignali, D. A., Hardtke-Wolenski, M., Jaeckel, E., Blazar, B. R., & Sauer, M. G. (2011). PD-L1 blockade effectively restores strong graft-versus-leukemia effects without graft-versus-host disease after delayed adoptive transfer of T-cell receptor gene-engineered allogeneic CD8+ T cells. *Blood*, *117*(3), 12.
- Zeiser, R., & Blazar, B. R. (2017). Acute graft-versus-host disease - biologic process, prevention, and therapy. *New England Journal of Medicine*, *377*(22), 2167–2179.
- Zhang, A., Xiong, Y., Xu, F., Wang, Z., Ma, J., Zhao, N., Hu, T., Yi, J., Zhou, Y., & Luan, X. (2020). IL-1beta enhances human placenta-derived mesenchymal stromal cells ability to mediate Th1/Th2 and Th1/CD4(+)/IL-10(+) T cell balance and regulates its adhesion, proliferation and migration via PD-L1. *Cellular Immunology*, *352*:104113.
- Zhang, B., Yeo, R. W. Y., Lai, R. C., Sim, E. W. K., Chin, K. C., & Lim, S. K. (2018). Mesenchymal stromal cell exosome-enhanced regulatory T-cell production through an antigen-presenting cell-mediated pathway. *Cytotherapy*, *20*(5), 687.
- Zhang, Q., Fu, L., Liang, Y., Guo, Z., Wang, L., Ma, C., & Wang, H. (2018). Exosomes originating from MSCs stimulated with TGF-beta and IFN-gamma promote Treg differentiation. *Journal of Cellular Physiology*, *233*(9), 6832–6840.

## SUPPORTING INFORMATION

Additional supporting information may be found online in the Supporting Information section at the end of the article.